UNIVERSITY OF SOUTHAMPTON

Faculty of Physics Sciences and Engineering
Optoelectronics Research Centre

Silicon fibres for nonlinear wavelength conversion

by

Meng Huang

Supervisor: Prof. Anna C. Peacock

Co-Supervisor: Prof. Radan Slavík

A thesis for the degree of
Doctor of Philosophy

February 2024

University of Southampton

Abstract

Faculty of Physics Sciences and Engineering
Optoelectronics Research Centre

Doctor of Philosophy

Silicon fibres for nonlinear wavelength conversion

by Meng Huang

Supervisor: Prof. Anna C. Peacock
Co-Supervisor: Prof. Radan Slavík

Nonlinear optics has been one of the most important research areas in optics since the invention of lasers. Within this field, nonlinear fibre optics has gained notable attention as the guided light can be confined tightly within small core cross sections over extended lengths, thus enhancing the nonlinear interactions. In recent years, silicon core optical fibres have emerged as a versatile platform for nonlinear applications due to the high nonlinearity of the silicon material and their ability to be integrated with other fibre-based components. The motivation of this project is to build novel nonlinear photonic devices using silicon core fibres. In this thesis, the polysilicon core fibres were fabricated via a conventional molten core drawing method and subsequently tapered down to small core diameters in a range of 0.7 μm to 2 μm to enhance the nonlinearity. The linear and nonlinear properties of tapered silicon core fibres were characterised to ensure excellent nonlinear performance after the tapering process. Then the tapered fibres were used for nonlinear applications. Firstly, Raman amplification was demonstrated using a silicon core fibre for the first time. A Raman gain of 1.1 dB was obtained by using a continuous wave pump source in the telecom band. Following the initial Raman amplification demonstration, an enhanced peak Raman gain of 30.4 dB was achieved by using a pulsed pump laser in the 2 μm regime, taking advantage of the lower nonlinear losses in this region. Secondly, wavelength conversion based on four-wave mixing was investigated. Following a discussion on the roles of the dispersion profile and fibre length in the wavelength conversion processes, measurements were conducted to confirm the expected efficiencies of four-wave mixing in the tapered silicon core fibres. A maximum conversion efficiency of -30 dB was measured and a wavelength conversion range of 280 nm was achieved. Moreover, the possibility to enhance the four-wave mixing processing using the high Raman gain was also studied in silicon core fibres. A maximum Raman enhancement of $\sim$15 dB was achieved experimentally by using tapered silicon core fibres with a suitable dispersion

profile and length. Finally, undetected-photon imaging was demonstrated using photon beams generated via four-wave mixing processes in the silicon core fibres, which was the first such imaging example to make use of a third-order nonlinear process. Due to the strong correlation of photon beams, both high-quality phase and amplitude images were measured with a resolution of 1.4 mm. These demonstrations show the wide-ranging potential of silicon core fibres for use in nonlinear processes that extend the wavelength coverage beyond traditional glass fibre systems.

Contents

List of Figures

List of Tables

Declaration of Authorship

I declare that this thesis and the work presented in it is my own and has been generated by me as the result of my own original research.

I confirm that:

1. This work was done wholly or mainly while in candidature for a research degree at this University;
2. Where any part of this thesis has previously been submitted for a degree or any other qualification at this University or any other institution, this has been clearly stated;
3. Where I have consulted the published work of others, this is always clearly attributed;
4. Where I have quoted from the work of others, the source is always given. With the exception of such quotations, this thesis is entirely my own work;
5. I have acknowledged all main sources of help;
6. Where the thesis is based on work done by myself jointly with others, I have made clear exactly what was done by others and what I have contributed myself;
7. Parts of this work have been published as: See List of Publications

Signed:..... Date:.....

Acknowledgements

It was an impressive journey to study PhD progress at the Optoelectronic Research Centre, University of Southampton. Here I would like to acknowledge a few people who have given me important support to make my journey more smooth.

I would like to thank my supervisor Prof. Anna C. Peacock for her kind guidance and supervision during my PhD. I have learned a lot of important academic skills from her and I like the excellent working environment and academic atmosphere she created in the research group. I would also like to thank my co-supervisor Prof. Radan Slavík for offering sensible experiment suggestions and always happy to help me when I face challenges.

Then I would like to thank my colleagues, Dr. Shiyu Sun, Dr. Amar N. Ghosh, Dr. Than S. Saini, Dr. Dong Wu, Dr. Haonan Ren and Dr. Li Shen. They delivered a lot of important ideas and skills to me.

Then I would like to thank my collaborators, Prof. Ursula J. Gibson, Prof. John Ballato, Dr. Thomas W. Hawkins, Prof. Marco Liscidini and Prof. John E. Sipe. With their support, I had the opportunity to generate impressive works during my PhD.

Then I would like to thank my parents, Mr. Qinghua Huang and Mrs. Xiaoqing Lin. I would also like to thank my wife, Mrs. Liying Fang. They gave me important mental support when I face challenges.

In the end, I am proud of my hard work and acquisition of many new skills in the past four years.

Definitions and Abbreviations

3PA	Three-Photon Absorption
a-Si	Amorphous Silicon
a-Si:H	Hydrogenated Amorphous Silicon
BC	Beam Combiner
BS	Beam Splitter
CaO	Calcium Oxide
CE	Conversion Efficiency
c-Si	Crystalline Silicon
CW	Continuous Wave
DP	Detected Photon
FCA	Free Carrier Absorption
FCD	Free Carrier Dispersion
FOD	Fourth-order Dispersion
FSR	Free Spectral Range
FWHM	Full Width at Half Maximum
FWM	Four-wave Mixing
GaAs	Gallium Arsenide
GVD	Group Velocity Dispersion
HPCVD	High-pressure Chemical Vapor Deposition
IRS	Inverse Raman Scattering
LIA	Lock-in Amplifier
LP	Linear polarised
MCD	Molten Core Drawing
MFD	Mode Field Diameter
MOF	Microstructured Optical Fibre
NA	Numerical Aperture
NLSE	Nonlinear Schrödinger Equation
OSA	Optical Spectrum Analyser
PC	Polarisation Controller
PDC	Parametric Down-conversion
poly-Si	Polycrystalline Silicon
SCF	Silicon Core Fibre

SiGe	Silicon-germanium
SMF	Single Mode Fibre
SOI	Silicon-on-insulator
SPM	Self-phase Modulation
SRS	Stimulated Raman Scattering
SSPD	Silicon Schottky Photodetector
TLF	Tapered Lensed Fibre
TPA	Two-photon Absorption
UP	Undetected-photon/ Undetected Photon
WDM	Wavelength Division Multiplexer
ZDW	Zero-dispersion Wavelength
ZnSe	Zinc Selenide

Chapter 1

Introduction

1.1 Nonlinear fibre optics

In 1960, the invention of the laser gave birth to the new research field of nonlinear optics [1]. The response of optical media to the light field could no longer be taken to be linear as the light intensity produced by lasers was high enough to manipulate the optical properties of a material [2]. By investigating the interaction between different lasers and optical materials, a variety of nonlinear processes were discovered in the decade of 1960s, including the intensity-dependent refractive index [3], second harmonic generation [4], Raman scattering [5], Brillouin scattering [6], and four-wave mixing (FWM) [7]. In the initial investigations, transparent crystal and liquid materials were used as nonlinear optical mediums, such as quartz, sapphire and organic dyes [4]. As a common optical material, silica glass was also on the research list of nonlinear optics [8]. However, due to the relatively weak nonlinear properties, it seemed not a good idea to use silica for nonlinear applications. For example, the second-order nonlinearity of silica vanishes due to the inversion symmetry of molecular arrangement. Moreover, the third-order nonlinearities, including the Kerr effect, Raman scattering, and Brillouin scattering, are several orders of magnitude smaller than other popular nonlinear materials, such as carbon disulfide, organic dyes and semiconductors like gallium arsenide (GaAs).

Although the appearance of silica glass fibres can be traced back even earlier than the invention of lasers, the high impurities of the early silica optical fibres resulted in high transmission losses, thus they were not considered to be useful for nonlinear experiments. However, with the invention of low-loss silica optical fibres in 1970 [9], nonlinear fibre optics became an active research area. High-intensity light can be confined tightly within a small spot size (mode diameter <10 μm for single-mode fibres) and propagate over long fibre lengths with extremely low losses (<1 dB km^{-1} in the wavelength range of 1–1.6 μm) so that nonlinear effects could be observed at low power

levels even with the low nonlinearity of silica glass. Most of the third-order nonlinear effects were successfully observed in low-loss silica fibres during the 1980s [10]. A remarkable achievement of this period was the discovery of solitons in silica glass optical fibres, which gave birth to a new branch of nonlinear optics [11, 12, 13].

In the 1990s, with the invention of microstructured optical fibres (MOFs), nonlinear fibre optics continued to grow considerably. As the nonlinearity of these special silica fibres can be enhanced through structural engineering, the fibre length needed for nonlinear applications can be reduced drastically [14, 15]. Moreover, some special MOFs, such as hollow core fibres, can be filled with highly nonlinear gases or fluids, offering flexible choices of nonlinear materials [16]. Interestingly, the development of MOFs also provides the possibility to produce semiconductor core fibres by depositing semiconductors from chemical precursors into the holes of MOFs [17]. Most of the semiconductor materials, including silicon, germanium, tellurium, zinc selenide (ZnSe), silicon–germanium (SiGe) alloys and GaAs, have strong nonlinearities [18]. Among these materials, silicon has attracted most of the attention due to its fantastic electronic and optical properties, which makes it not only very popular in the electronics industry but also important in the research field of silicon photonics.

1.2 Silicon photonics

Silicon is the second most abundant element within the Earth's crust (about 28%). As a semiconductor material, the electrical conductivity properties of silicon can be manipulated by introducing dopants so that they can act as insulators or conductors. Compared with other semiconductor materials, silicon has a high optical damage threshold and thermal stability ($\sim$10 times higher than GaAs), which helps to make it the dominant material in the semiconductor industry. With the development of the semiconductor industry, high-quality silicon-on-insulator (SOI) wafers can be produced at low-cost from the mid-1980s, and SOI has been also treated as an ideal optical platform. Thanks to the wide low-loss transmission window (1.1-8 μm), silicon is suitable for optical applications extending from the near-infrared spectral region up to the mid-infrared region. Importantly, due to the strong optical confinement offered by the high refractive index contrast between silicon ($n_{Si} = 3.45$) and silica ($n_{SiO_2} = 1.45$), SOI can be used for creating integrated planar waveguide circuits. Numerous passive and active photonic devices have been successfully demonstrated in the SOI platform, such as low-loss waveguides [19], multiplexers [20], resonators [21] and modulators [22, 23].

Moreover, silicon has attractive nonlinear optical properties. The Kerr index for silicon is $\sim$100 times larger than silica, whereas the Raman coefficient is $\sim$1000 times stronger [24]. As a result, nonlinear silicon photonics has attracted intense interest in the past

decades, and a variety of nonlinear devices have been demonstrated in the SOI platform, such as all-optical switches [25], Raman lasers [26], parametric amplifiers [25], supercontinuum generation [27], and frequency comb generators [28].

However, the huge mode mismatch between the silicon waveguide (mode area $\sim$0.1 μm^2) and a single mode silica fibre (mode area $\sim$50 μm^2) makes it difficult to couple light efficiently from a fibre network to a planar waveguide system. To overcome the mode mismatch between these two systems, two main light coupling approaches were developed. Figure 1.1(a) shows the inverted taper method, where the light from the single mode fibre (SMF) is launched into the nanotaper tip with most of the light in the cladding. The light then is absorbed into the core as the width increases. Due to the wavelength insensitivity of the inverted taper waveguide, this method can achieve high coupling efficiency over a broad wavelength range. However, it is difficult to fabricate a tiny tip because the tip end is very fragile during the etching process. Figure 1.1(b) shows the grating coupler method, where an etched grating is used to collect the light from SMF. Due to the relatively large size, the grating is robust during the etching process. However, the grating couplers usually have narrower operating bandwidth and lower coupling efficiency than inverted taper couplers. In recent years, the achieved lowest coupling losses in the telecom band for the inverted taper method and grating coupler method were $\sim$0.7 dB [29] and $\sim$1.6 dB [30], respectively. Although the coupling loss can be optimised to be very low for SOI waveguides, precise alignment is still needed for the planar waveguide systems, which reduces the robustness. Moreover, due to the absorption loss from silica cladding, the working wavelength of SOI waveguides is limited to $\sim$3.3 μm [31, 32]. Thus, more complicated structures of silicon planar waveguides are necessary for longer working wavelengths, such as suspended waveguides [33], silicon-on-sapphire [34] and SiGe-on-silicon [35].

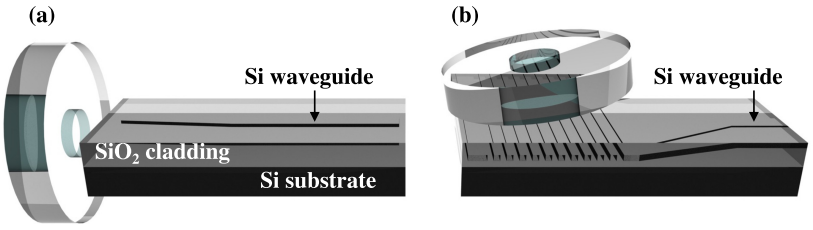

FIGURE 1.1: Coupling strategies between an optical fibre and a silicon planar waveguide. (a) Inverted taper method. (b) Grating coupler method.

1.3 Silicon core fibre

Inspired by the successes achieved in nonlinear fibre optics and silicon photonics, a silicon core fibre (SCF) platform has emerged in the past decades. This novel fibre platform consists of a silicon core surrounded by silica cladding. The motivation of

this new platform is to combine the unique optoelectronic properties of silicon with the excellent light-guiding properties of fibre waveguides [18]. Compared with planar waveguides, the SCFs are more flexible due to the fibre geometry and can be produced with long lengths using conventional fibre-drawing methods. They are also compatible with post-processing methods for silica optical fibres, such as cleaving, polishing, splicing and tapering. Due to the similar silica cladding and fibre geometry, it is convenient to splice a SCF with a SMF to fabricate robust all-fibre devices, and the splicing loss between SMF and SCF can be reduced to as low as 1 dB by introducing anti-reflection structures [36, 37]. A remarkable work in recent years is the all-fibre, fully-integrated frequency comb generator in Ref. [38], where both sides of the SCF were spliced to a SMF with low losses. Another benefit of the SCF platform is that it is convenient to tailor the fibre dimensions by using a tapering procedure to engineer the dispersion of SCFs for better nonlinear performances. For example, supercontinuum generation in a dispersion engineered SCF can achieve high brightness and coherence within a spectrum spanning from 1.6-5.3 μm [39], which is much broader than what has been achieved in the SOI platform (1.5-3.3 μm) [31]. In conclusion, SCFs present a useful combination of optical fibres and silicon photonics, which have shown excellent nonlinear properties and are more compatible with conventional fibre networks. Although planar silicon waveguides are still the best choice for applications that need very large-scale integration, SCF can be an alternative solution for near- and mid-infrared applications that need robust and portable highly nonlinear optical systems, for example in sensing, signal processing, or free-space communications.

1.4 Literature review

1.4.1 Fabrication procedures

In 2006, Sazio *et al.* fabricated the first SCF by using a high-pressure chemical vapour deposition (HPCVD) technique. As shown in the schematic of Figure 1.2(a), a silane precursor was flowed through the holes under high pressures (MPa to tens of MPa) and temperatures ($\sim$700 ^{o}C) to deposit silicon into the pores of a capillary tube [17]. The fabricated SCFs had a polycrystalline silicon (poly-Si) core and an estimated linear loss of 7 dB cm^{-1} at 1.55 μm. Following the initial work, in 2007, Finlayson *et al.* found that semiconductor materials could be deposited into the silica capillaries in an amorphous state by reducing the deposition temperatures to $\sim$500 ^{o}C [40]. However, due to the dangling bonds of amorphous silicon (a-Si), these fibres were highly lossy over the infrared wavelength regime. To saturate the dangling bonds, hydrogen was retained in the a-Si fibre by further reducing the deposition temperature to $\sim$400 ^{o}C [41]. In 2010, Lagonigro *et al.* reported the first hydrogen amorphous silicon (a-Si:H) fibre with a measured loss of $\sim$5 dB cm^{-1} at 1550 nm [42]. By tuning the hydrogen content with

more precisely control of the deposition temperature, the losses of the a-Si:H fibres could be further reduced to 1 dB cm^{-1} [18]. The key benefit of the HPCVD method is the ability to fabricate high-quality SCF with either a-Si:H or poly-Si core in a flexible core diameter range of 1-10 μm. In 2011, Healy *et al.* measured the surface roughness of the core–cladding interface by using a 1.3 μm core size HPCVD SCF [43]. The small roughness value ($\sim$0.1 nm) and low surface scattering loss ($<$0.1 dB cm^{-1}) highlighted the quality of the core/cladding interface of the HPCVD fibres and their suitability for obtaining low transmission losses in small core structures. However, the deposition process of the HPCVD method was time-consuming and the fibre lengths are limited to a few centimetres.

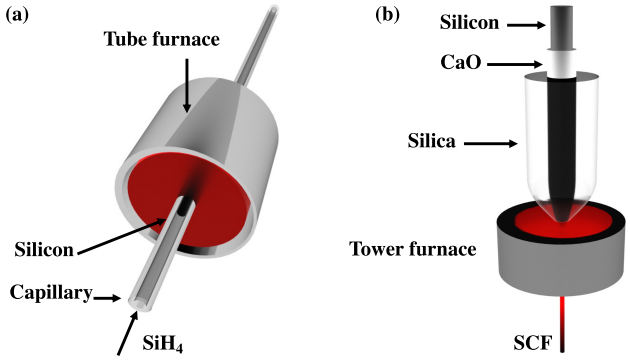

FIGURE 1.2: Schematic of the SCF fabrication methods. (a) High-pressure chemical vapour deposition technique. (b) Molten core drawing method.

Inspired by the success of traditional fibre fabrication methods, Ballato *et al.* developed a tower drawing approach to fabricate long-length SCFs in 2008 [44]. As shown in Figure 1.2(b), a fibre preform was created by sleeving a silicon rod inside a silica glass tube and then drawn down to fibre dimensions with a heating temperature of $\sim$1900 ^{o}C. Due to the lower melting temperature of silicon ($\sim$1400 ^{o}C), the core was molten during the drawing process. Hence this method was called the molten core drawing (MCD) method. The initial fabricated SCF had a length of $\sim$30 m, with an estimated large core diameter in the range of 60-120 μm. Despite the success in fabricating long lengths of SCF, the as-drawn fibre contained lots of bubbles in the poly-Si core and the bubble-free lengths were less than 5 cm. To investigate the generation mechanism of the bubbles, Minami *et al.* compared the influence of different atmospheres (argon vs vacuum) for the drawing process in 2011 [45]. This work confirmed that the bubbles were formed with argon and can be avoided with a vacuum drawing atmosphere. In 2012, Schnurre *et al.* studied the role of the cross-sectional geometry on the resultant core crystallography [46]. This work suggested that the square-core exhibited higher local single-crystallinity than the round-core silicon fibre (90% vs 70%). However, the longest single crystalline length for both cases was similar (4–5 mm). Moreover, due to the thermal mismatch and oxygen diffusion between the silicon core and silica cladding, the

team was still struggling to draw SCFs with small core diameters by using the initial MCD method.

In 2013, to prevent the oxygen diffusing and balance the thermal mismatch, Nordstrand *et al.* used calcium oxide (CaO) as an interface modifier between the silicon core and silica cladding [47]. After introducing the CaO interface, the core diameter could be drawn down to 10 μm with low oxygen incorporation and strong mechanical strength (<1 cm bending radii). The measured losses were 5-11 dB cm^{-1} due to the small defects and discontinuities that exist in the poly-Si core. To further reduce the fibre core diameter and transmission loss, some researchers invested their efforts to further optimise the MCD method. In 2021, Kudinova *et al.* reported a stack-and-draw method that can draw SCFs with core dimensions in a range of 0.8-3.5 μm [48]. A 3.3 μm diameter core fibre was characterised to have a background loss of less than 0.2 dB cm^{-1} in telecom band, but the nonlinear properties were not thoroughly studied due to unknown conditions. Other researchers focused on using post-processing techniques to optimise the core materials.

It is worth noting that there were some other interesting MCD methods that target SCF production for applications outside the nonlinear field. In 2009, Scott *et al.* reported a power-in-tube technique to fabricate n-type silicon core optical fibres, where phosphorus-doped silicon wafers were fractured and then inserted into a silica tube to form a n-type preform [49]. In the same year, Hou *et al.* reported an interesting MCD that used an aluminium rod to form the fibre preform. The SCF was produced via the redox reaction between aluminium and silica during the fibre drawing process [50]. Owing to the different solubility properties, the silicon, aluminium and aluminium oxide were totally separated and finally form a pure silicon core.

1.4.2 Post-processing techniques

Post-processing techniques were first used to optimise the performance of HPCVD SCFs. In 2010, Healy *et al.* used a fibre tapering method to tailor the core diameter of HPCVD SCFs to submicron dimensions [51]. A fusion splicer was used to taper the core diameter of the SCF from 1.3 μm to ~500 nm. The total device loss was ~12 dB with an estimated taper loss of only ~0.5 dB. In 2016, Chaudhuri *et al.* used a two-step thermal annealing method to recrystallise a HPCVD SCF with a core diameter of 5.6 μm. The core material was recrystallised from a-Si to poly-Si with an annealing temperature of 530 ^{o}C for the first step and 1300 ^{o}C for the second step [52]. The optimised optical loss was 5.2 dB cm^{-1} in the telecom band and 0.99 dB cm^{-1} at 2.2 μm. When the as-drawn SCFs can be produced with a small core diameter of ~10 μm via the modified MCD method, post-processing methods were also applied to optimise the quality of these fibres. In 2016, Healy *et al.* used a carbon dioxide (CO_2) laser to recrystallise the core material of as-drawn SCFs [53]. The fibre loss was reduced from 14–20 dB cm^{-1} to

2 dB cm^{-1} at 1.55 μm for a SCF with a core diameter of 12 μm. Additional material characterisation indicated that a single crystal silicon grain with a length of 1.8 cm could be generated along the fibre after laser recrystallising. In the same year, Suhailin *et al.* tapered the as-drawn SCF from a 10 μm core diameter to ~1 μm with a measured loss of ~3.5 dB cm^{-1} at 1.55 μm [54]. Then the loss of tapered as-drawn SCFs were further reduced to 2 dB cm^{-1} by Franz *et al.* in 2017 [55]. In summary, due to the motivation for nonlinear applications, the development of post-processing techniques for SCFs have mainly focused to reducing the core diameter and transmission loss. Figure 1.3 plots a map of the transmission loss in the telecom C-band, as a function of core diameter for SCFs produced via the different methods [18]. With the development of post processing techniques, the as-drawn SCFs fabricated by MCD method have become more and more popular, and the linear loss of MCD SCFs can be reduced to less than 1 dB cm^{-1}. Moreover, the core diameters of these fibres can be reduced to submicron to enhance the nonlinear interactions. It is for this reason why I focus on the MCD SCFs for the work in this thesis.

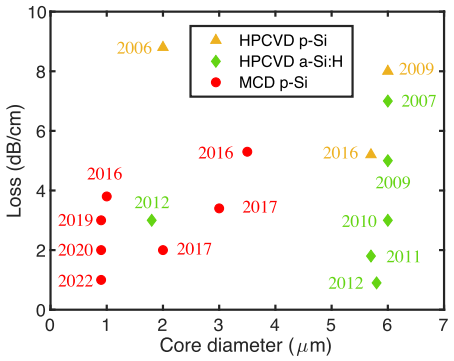

FIGURE 1.3: Recent progress to reduce the losses and core diameters for SCFs fabricated by the HPCVD and MCD methods.

1.4.3 Photonic applications

Early nonlinear applications in SCFs were demonstrated by using HPCVD SCFs due to the lower transmission losses and smaller core sizes compared to MCD SCFs. In 2010, Mehta *et al.* presented the first full characterisation of the nonlinear properties of an a-Si:H SCF [56]. The nonlinear absorption coefficients ($\beta_{TPA} \sim 0.8$ cm GW^{-1} and $\sigma \sim 1 \times 10^{-16}$ cm^2) and Kerr index ($n_2 \sim 1.8 \times 10^{-13}$ cm^2 W^{-1}) were measured by comparing the nonlinear transmission measurements with numerical models. In 2011, Mehta *et al.* subsequently demonstrated ultrafast nonlinear signal processing in an a-Si:H SCF [57]. A subpicosecond modulation with an extinction ratio of 4.5 dB was achieved by using the two-photon absorption (TPA) process. Inspired by the success of using TPA for ultrafast processing, in the same year, Mehta *et al.* demonstrated an ultrafast wavelength conversion by using the cross-phase modulation process in

an a-Si:H fibre [57]. A subpicosecond response time with 12 dB extinction ratios was obtained for the telecom band wavelength conversion process, indicating the potential of SCFs for high-speed nonlinear optical switching. Inspired by the achievements in telecom band signal processing, the research interest then shifted to the mid-infrared regime. In 2013, Shen *et al.* characterised the nonlinear transmission properties of a-Si:H fibres extending to mid-infrared regime [58]. The measured linear losses decreased from 2.1 dB cm^{-1} to 0.62 dB cm^{-1} as the wavelength increased from 1.55 μm to 2.3 μm, and the TPA was negligible when the wavelength was beyond $\sim$1.7 μm. These results showed the advantages of a-Si:H fibres for mid-infrared applications. In 2014, Shen *et al.* observed a supercontinuum generation from 1.64–3.37 μm in a 1.7 μm core size a-Si:H fibre [59]. Two sidebands of FWM were also observed in Ref. [59] when the pump wavelength was close to the zero-dispersion wavelength.

The first nonlinear demonstrations of MCD SCFs were reported when Suhailin *et al.* successfully reduced the core diameters to $\sim$1 μm by using the tapering approach. Following the successes achieved in HPCVD SCFs, the roadmap for the nonlinear applications of MCD SCFs was clear. The nonlinear properties of tapered SCFs were first characterised in the telecom band [54]. A TPA coefficient (β_{TPA}) of $\sim$0.7 cm GW^{-1} and a Kerr index (n_2) of $\sim 5 \times 10^{-14}$ cm^2 W^{-1} were measured. Both these values matched well with single-crystal silicon, which also confirms the high-quality of the silicon core after tapering. In 2017, Franz *et al.* characterised the material of tapered SCFs by using Raman spectroscopy and X-ray diffraction [55]. By comparing with the as-drawn SCFs, the results indicated that the original millimetre-long silicon crystal grains could be recrystallised to a centimetre-long grain, thus the transmission loss could be reduced from 10 dB cm^{-1} to 2 dB cm^{-1}. In the same year, important progress was made toward all-fibre integration between SCFs and SMFs. Ren *et al.* demonstrated a proof-of-concept for low-loss SCF-SMF integration using a nano-spike structure on the end of a SCF [37]. In this work, the nano-spike coupler was formed using a modified tapering method in which the silicon core was collapsed using a modified tapering method in which the silicon core was collapsed to form the spike. The small core of the spike region acts to force more of the core-guided light out into the silica cladding, increasing the mode size and reducing the reflection loss between SCF and SMF. The measured coupling and transmission loss were below 4 dB and 2 dB cm^{-1}. At around the same time, Wu *et al.* demonstrated broadband optical parametric amplification in the telecom band of 1420-1680 nm. An on-off optical parametric gain of up to 9 dB was achieved by using a precisely dispersion-engineered tapered submicron SCF ($\sim$915 nm). Following this, I was able to show that by combining the precise core tailoring with the nano-spike couplers, the SCFs could be incorporated within all-fibre systems as an efficient nonlinear silicon photonic wavelength converter for telecom band [60]. A conversion of 20 Gb s^{-1} bitrate quadrature phase-shift keying signals was successfully demonstrated with a low bit-error rate, thus confirming the potential to use this robust SCF platform for telecom band communication applications.

Then the research interest for the tapered MCD SCFs turned to the mid-infrared regime. In 2019, Ren *et al.* characterised the optical transmission properties of tapered MCD SCFs from the wavelength of 1.5 μm to 2.5 μm [61]. The tapered SCF showed a linear loss of $\sim$2 dB cm^{-1} in the whole wavelength range and a negligible TPA when $\lambda > 2.25$ μm. Inspired by the excellent nonlinear properties in the mid-infrared, Ren *et al.* also demonstrated the mid-infrared supercontinuum generation from 1.6–5.3 μm using a tapered SCF with a length of only $\sim$1 cm [39]. With careful design of the tapered profile to reduce the interaction with the silica cladding, the longer wavelength edge of the measured spectrum was far beyond that of planar waveguides (3.3 μm). Moreover, due to the larger core of the SCF, the spectral density was much higher than that in the planar waveguides (2 μW nm^{-1} vs 0.2 μW nm^{-1}), confirming the advantages of power handling for longer wavelengths by using fibre geometry.

It is worth noting that thanks to the combination of good electrical and optical properties, SCFs have also been used to build optoelectric devices. In 2014, Martinsen *et al.* demonstrated a solar cell with a n-type MCD SCF [62]. A vapour deposition technique was used to create the p-i-n junction with an overall conversion efficiency of 3.62%. Following this initial work, in 2014 Homa *et al.* demonstrated a SCF-based p-n junction by removing the silica cladding, and then using boric acid solution to react with silicon core to generate a p-type boron layer outside the n-type SCF [63]. In the same year, Healy *et al.* reported a laser-crystallised method to shift the bandgap of the silicon core material in a HPCVD SCF [64]. A continuous wave (CW) argon ion laser ($\lambda = 488$ nm) was used to introduce a strain gradient through the laser crystallising process and reduce the silicon bandgap from 1.11 eV down to 0.59 eV. In 2015, Huang *et al.* demonstrated an in-line silicon Schottky photodetector (SSPD) in telecom band by using a MCD SCFs [65]. A responsivity of 0.226 mA W^{-1} was achieved when reverse-biased at 0.45 V, which was comparable with conventional SSPDs. The large refractive index difference between the silicon core and silica cladding also made it possible to build high-quality cavities and resonators for sensing. In 2015, Zhang *et al.* reported an all-fibre silicon cavity Fabry–Perot interferometer by splicing the SCF with conventional SMF [66]. A high temperature sensitivity of 82 pm ^{o}C^{-1} was demonstrated within the range of 10-100 ^{o}C. The extinction ratio was approximately 14 dB and the free spectral range (FSR) was 9.34 nm. In the same year, Suhailin *et al.* demonstrated the first hybrid silicon-core, silica-clad microspherical resonator with a MCD SCF [67]. The resonator was formed by softening the tip of SCF with a CO_2 laser. A FSR of $\sim$4.7 nm and a high quality factor (Q) of $\sim 1.11 \times 10^5$ was achieved, which was 100 times larger than that of pure silicon microcylindrical resonators.

In conclusion, due to the development of high-quality SCFs with small core diameter ($<$1 μm) and low transmission loss ($<$2 dB cm^{-1}), a variety of nonlinear applications such as ultrafast signal processing and wavelength generation were demonstrated in the telecom bands and mid-infrared regimes. Moreover, thanks to its unique electrical

properties and special fibre geometry, the SCF platform has also shown versatility to build devices beyond nonlinear applications, such as solar cell systems, photodetectors and sensing systems. However, despite these successes, Raman amplification was one of the nonlinear processes that had yet to be observed prior to this project. This difficulty in observing Raman was attributed to the relatively short lengths of the low-loss SCFs produced up to this date ($\sim$1 cm).

1.5 Key achievements

1. Developed the method to taper long-length SCFs with low losses. The tapering parameters, including tapering ratio, speed, and heating power were further optimised. Using this method, the core diameter of as-drawn SCFs could be tapered down to a range of 0.7 μm-3 μm with a transmission loss of $<$1 dB cm^{-1} and a length of up to 6.5 cm. The maximum achievable length was only limited by the range of the tapering rig.

2. Provided the first demonstration of the Raman amplification in SCFs. The Raman gain coefficient of the tapered SCFs was fully characterised using a 1431 nm wavelength CW laser and a 2 μm wavelength thulium fibre-based pulsed laser. A 1.1 dB on-off gain was achieved in the telecom band (1.55 μm) and an 30.4 dB peak on-off gain was achieved in the mid-infrared regime (2.22 μm).

3. Measured the Raman-enhanced FWM experimentally. The FWM efficiency with the enhancement caused by Raman scattering was first measured in the telecom band. A maximum enhancement of $\sim$15 dB was achieved by using a low-power CW pump ($\sim$20 mW) by setting the new generated wave of FWM within the Raman emission bandwidth.

4. Demonstrated classical undetected-photon imaging with tapered SCFs. Amplitude and phase images was measured by using the undetected-photon beams generated by stimulated FWM. The fiberised imaging system was specially designed to produce stable and robust images. An imaging resolution of 1.4 mm and an interference visibility of more than 53% was observed experimentally. It is worth noting that this was the first time a third-order nonlinear process had been used as a source for undetected-photon imaging.

1.6 Thesis outline

Chapter 2 reviews the background knowledge of optical fibres and their primary nonlinear effects. The important fibre parameters are introduced first, including refractive index and group velocity dispersion. The concept of fibre modes is also discussed to

better understand light propagation in a fibre. In the nonlinear section, the third-order nonlinear effects that dominate in the SCFs are introduced first. Then the nonlinear Schrödinger equation is presented to describe ultrashort pulse propagation in a SCF, and the influence of linear loss, dispersion and nonlinear effects are discussed. In the end, the important nonlinear processes for this thesis are introduced, including self-phase modulation, FWM and Raman scattering.

Chapter 3 introduces the fabrication and characterisation for the tapered SCFs. The MCD method, including the incorporation of a core/cladding interface layer, is introduced first, followed by the two-step tapering method. The role of the tapering process in the crystallinity improvement of silicon core is discussed by comparing that with the as-drawn SCFs. Then the profile of tapered SCFs is introduced, followed by a short section about the fibre facet polishing method. In the fibre characterisation section, the linear losses of the tapered SCFs, as measured by the cut-back method, are presented. Then nonlinear properties, which includes the TPA coefficient and Kerr index, are characterised by comparing the nonlinear saturation and spectral broadening with the numerical modelling of the nonlinear Schrödinger equation.

Chapter 4 investigates the Raman process in both the telecom band and mid-infrared regimes. The previous Raman demonstrations in planar silicon waveguides are reviewed first. Then the spontaneous Raman emission and the stimulated Raman amplification of tapered SCFs are characterised in the telecom band. For the mid-infrared regime, the fibre profile of the tapered SCF is redesigned to reduce the absorption from silica cladding. Then the mid-infrared spontaneous emission and stimulated amplification are measured with a pulsed mid-infrared laser and compared with those obtained in the telecom band. Finally, the wavelength extension to the regime of 2-5 μm via cascaded Raman scattering is discussed.

Chapter 5 studies FWM and Raman-enhanced FWM in the telecom band. The dispersion engineering method, which is used to achieve phase-matching for highly efficient FWM, is introduced first. The role of phase matching and fibre length in the FWM process is discussed. Then the FWM in tapered SCFs with different core sizes and lengths are characterised and analysed. The influence of fibre core diameter and length is studied by comparing the measured FWM efficiency curves with the simulation modelling. In the Raman-enhanced section, the FWM efficiency is measured by tuning the FWM wavelength within the Raman emission bandwidth. The Raman enhancement is measured by using tapered SCFs with different core sizes and lengths to investigate the role of phase-matching and fibre length in the Raman enhancement.

Chapter 6 demonstrates undetected-photon imaging using the beams generated by FWM in the SCFs. The concept of undetected-photon imaging and photon beams generation methods are discussed first. Then the design of the SCF-based imaging system is presented and compared with previous systems, including quantum and classical

systems. The fibre design for highly efficient photon beams generation is also discussed. After that, both amplitude imaging and phase imaging are demonstrated in the telecom band by using SCF-based undetected-photon imaging system. The imaging quality and system robustness is analysed. In the end, the possibility of extending the conversion wavelength of undetected-photon beams to mid-infrared regime is also discussed.

Chapter 7 concludes the achievements and new findings of this thesis, as well as discussing possible research opportunities for future work.

Chapter 2

Theory

2.1 Introduction

In this chapter, the background knowledge of light propagation in optical fibres is reviewed. The fibre structure, light propagation and mode theory are introduced first. Then, the optical properties of SCFs, such as light transmission loss, dispersion and nonlinearity are discussed. Moreover, the properties of ultrafast laser pulses that are used for nonlinear processes in SCFs are introduced. The influence of dispersion and nonlinearity during the propagation of ultrashort pulses is discussed by using the nonlinear Schrödinger equation. Finally, three nonlinear processes that are critical to the work in this thesis are described, including self-phase modulation (SPM), FWM and Raman scattering.

2.2 Optical Fibres

2.2.1 Light propagation

As shown in Figure 2.1(a), optical fibres have a high refractive index circular core (n_{core}) and a lower refractive index cladding (n_{clad}). Due to the refractive index contrast between the core and cladding, the light can be transmitted through total internal reflection in the interface of core and cladding. According to the refractive index profile, fibres can be usually divided into step-index fibre and graded-index fibre. Step-index fibre has a constant refractive index in the core and cladding. In contrast, the refractive index of graded-index fibre varies in the radial direction within the core, which is usually used to optimise the light propagating properties for multimode fibres. The most common material for optical fibres is silica glass because it has high mechanical strength and two low-loss transmission windows around 1.31 μm and 1.55 μm, which

makes it suitable for optical fibre communications. The core and cladding materials of traditional SMF are both silica glass, and the different refractive index for silica core and cladding are achieved by using different dopants. The parameter of refractive index difference (Δ) for the core and cladding of a fibre is defined as:

$$\Delta = \frac{n_{core} - n_{clad}}{n_{core}}, \tag{2.1}$$

where n_{core} is the refractive index of the core material and n_{clad} is the refractive index of the cladding material. The refractive index difference of SMFs is usually very small ($\Delta \approx 0.003$), therefore, SMFs are treated as weakly guided step-index fibres. In contrast, the core material ($n_{Si} = 3.45$) of SCFs studied in this work is much larger than the cladding material ($n_{SiO_2} = 1.45$), so that it has a much larger refractive index difference ($\Delta \approx 0.58$), which allows the propagating light be confined more tightly within the core. Thus, the core diameter of SCFs can be reduced to much smaller (<1 μm) than that of SMFs (~9 μm).

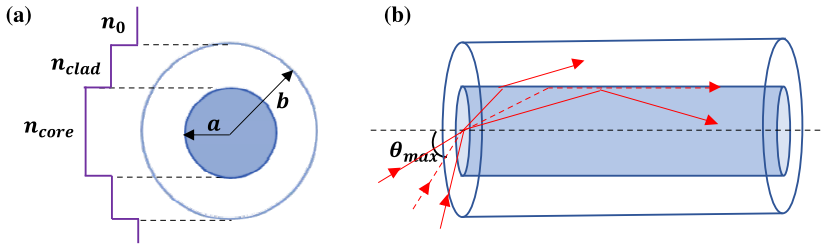

FIGURE 2.1: (a) Cross-sectional and refractive index profile of a fibre. (b) Schematic of light propagation in a step-index fibre.

Figure 2.1(b) shows the light propagation in a step-index fibre. The incoming light is allowed to propagate in the fibre when the injected angle is smaller than the maximum acceptance angle (θ_{max}), which can be calculated by using the numerical aperture (NA) of the fibre:

$$NA = n_0 \sin\theta_{max} = n_0 \sqrt{n_{core}^2 - n_{clad}^2}, \tag{2.2}$$

where n_0 is the refractive index of the optical medium for incoming light, which is usually air ($n_0 \approx 1$). The light coupling between fibres and other optical systems is usually achieved by optical lenses. To ensure high coupling efficiency, the NA of optical lens should match with the fibre. Moreover, the smallest achievable beam radius of the coupling lens should be smaller than the mode field diameter (MFD) of the fibre, which depends on the size of the optical field in the fibre core. The achievable smallest focus spot size (s) of a lens can be calculated by [68]:

$$s = \frac{1.27 M^2 \lambda f}{d}, \tag{2.3}$$

where M^2 is the laser beam parameter, λ is the wavelength, f is the focus length and d is the input beam diameter for the lens. The size matching between MFD and the focused beam spot can minimise the mode mismatch loss for light coupling. Moreover, the coupling efficiency is also influenced by the light alignment and the fibre facet condition. Figure 2.2(a) and Figure 2.2(b) show the coupling conditions with high efficiency and low efficiency, respectively. To achieve high coupling efficiency experimentally, the fibre facet should be flat (perpendicular to the z-axis) and smooth enough.

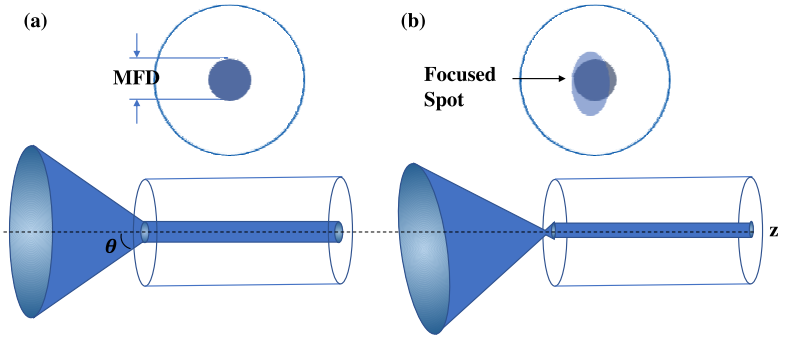

FIGURE 2.2: Schematic of light coupling from an optical lens to a fibre system with (a) high efficiency and (b) low efficiency.

Due to the large refractive index difference between silicon ($n_{Si} = 3.45$) and air ($n_0 = 1$), Fresnel reflection loss also contributes to the light coupling losses of SCFs. The Fresnel reflection loss can be calculated by:

$$R = (\frac{n_{core} - n_0}{n_{core} + n_0})^2 \approx 0.3. \tag{2.4}$$

The light propagation behaviour within a SCF can be described accurately by using wave optics, where the light is treated as electromagnetic waves. The propagation of optical fields in a fibre is governed by Maxwell's equations, which can be used to describe all electromagnetic wave propagation, either in free space or an optical medium. The wave equation, which is derived from Maxwell's equations, can be expressed as [2]:

$$\nabla^2 \widetilde{E} + n^2(\omega)\frac{\omega^2}{c^2}\widetilde{E} = 0, \tag{2.5}$$

where $\widetilde{E}$ is the Fourier transform of the electric field E, n is the refractive index profile of optical medium and ω is the light frequency. The solutions of Equation (2.5) are the spatial distribution $\widetilde{E}(r, \omega)$ of guided modes. Due to the cylindrical symmetry of fibres, the wave equation for a point can be rewritten to [2]:

$$\frac{\partial^2 \widetilde{E}}{\partial \rho^2} + \frac{\partial \widetilde{E}}{\rho \partial \rho} + \frac{\partial^2 \widetilde{E}}{\rho^2 \partial \phi^2} + \frac{\partial^2 \widetilde{E}}{\partial^2 z} + n^2 k_0^2 \widetilde{E} = 0, \tag{2.6}$$

where ρ is the Euclidean distance for the z-aixs to the point, ϕ is the angle between the reference direction on the chosen plane and the line from the origin to the projection of

the point on the plane, and $k_0 = \omega/c$ is the wavenumber in vacuum. In a cylindrical coordinate, the electric and magnetic field have six components $\widetilde{E}_\rho, \widetilde{E}_\phi, \widetilde{E}_z, \widetilde{H}_\rho, \widetilde{H}_\phi, \widetilde{H}_z$, but only two components out of six are independent. It is customary to choose $\widetilde{E}_z$ and $\widetilde{H}_z$ as the independent components to express the other four components. Here, $\widetilde{E}_z$ is considered as an example to be derived from Equation (2.6) and $\widetilde{H}_z$ can be derived by following the same method. The general solution of $\widetilde{E}_z$ for Equation (2.6) can be expressed as:

$$\widetilde{E}_z(\rho, \omega) = A(\omega)F(\rho)\exp(im\phi)\exp(j\beta z), \tag{2.7}$$

where $A(\omega)$ is the frequency dependent amplitude, m is an integer, β is the propagation constant, and $F(\rho)$ is the fibre modes. The propagation constant β can be calculated by using the refractive index (n) and the vacuum wavenumber ($\beta = nk_0$). By replacing $\widetilde{E}$ in Equation (2.6) with $\widetilde{E}_z(\rho, \omega)$, the equation for $F(\rho)$ can be obatained:

$$\frac{\partial^2 F}{\partial \rho^2} + \frac{\partial F}{\partial \rho} + (n^2k_0^2 - \beta^2 - \frac{m^2}{\rho^2})F = 0. \tag{2.8}$$

Equation (2.8) is the well-known differential equation for Bessel functions. Thus, the solution can be represented as [2]:

$$F(\rho) = \begin{cases} J_m(p\rho) & \rho < a, \\ K_m(q\rho) & \rho > a, \end{cases} \tag{2.9}$$

where a is the fibre core radius, J_m is the Bessel function of the first kind and K_m is the modified Bessel function of the second kind. p and q are defined as [2]:

$$p = k_0\sqrt{n_{core}^2 - n_{eff}^2}, \tag{2.10}$$

$$q = k_0\sqrt{n_{eff}^2 - n_{clad}^2}, \tag{2.11}$$

where n_{eff} is the effective refractive index of a fibre. When the light propagating in a fibre, the propagation constant β depends on the refractive index of both the core and cladding materials. Therefore, β should be modified by using an effective refractive index ($\beta = n_{eff}k_0$), which has a value between the refractive index of core and cladding ($n_{clad} < n_{eff} < n_{core}$). The value of n_{eff} can be obtained by solving the equation [69]:

$$[\frac{J_m'(pa)}{pJ_m(pa)} + \frac{K_m'(qa)}{qK_m(qa)}][\frac{J_m'(pa)}{pJ_m(pa)} + \frac{n_{clad}^2}{n_{core}^2}\frac{K_m'(qa)}{qK_m(qa)}] = [\frac{m\beta k_0(n_{core}^2 - n_{clad}^2)}{an_{core}p^2q^2}], \tag{2.12}$$

where m is a integer for each propagation constant β. For each integer value of m, Equation (2.12) has several solutions for β. Each eigenvalue β_{ms} (s is also an integer) describes a specific mode, which can be guided by the fibre if it satisfies the condition: $k_o n_{clad} < \beta_{ms} < k_o n_{core}$. The fibre modes are called HE mode if the longitudinal electric field value E_z is larger than H_z. Otherwise they care called EH modes. In particular,

when $m = 0$, the guided modes are transverse electric mode (TE, $E_z = 0$) or transverse magnetic mode (TM, $H_z = 0$), where the electric field E or magnetic field H are completely transverse to the fibre axis. When $m > 0$, all six components (E_ρ, E_ϕ, E_z, H_ρ, H_ϕ, H_z) of the electromagnetic field are non-zero. However, the guided modes can still be approximately treated as the linear polarised modes (LP modes) because E_z and H_z are negligible compared with the transverse components (E_ρ, E_ϕ, H_ρ, H_ϕ).

The number of guided modes for a step-index fibre is usually estimated with V number, which is a normalised frequency parameter and can be expressed as [70]:

$$V = ak_0\sqrt{n_{core}^2 - n_{clad}^2} = \frac{2\pi a}{\lambda}NA. \tag{2.13}$$

The number of guided modes supported by a multimode fibres can be estimated by:

$$M \approx \frac{V^2}{2}. \tag{2.14}$$

When V is smaller than the cut-off frequency ($V_c = 2.405$), only the fundamental mode HE_{11} is supported in the step-index fibre. To support only single mode propagation in a SCF, a core diameter of ~200 nm is needed to satisfy the cut-off frequency ($V_c = 2.405$).

2.2.2 Fibre modes

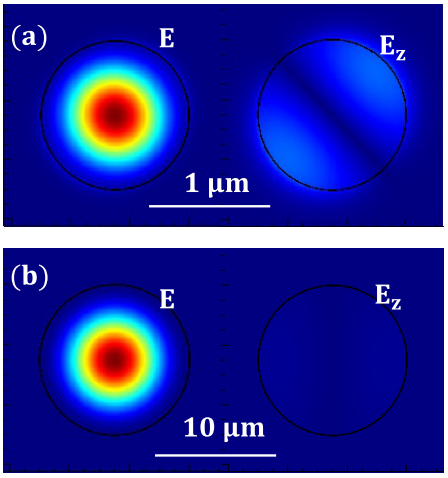

FIGURE 2.3: Fundamental mode profile in a SCF with core diameter of (a) 1 μm and (b) 10 μm.

Figure 2.3(a) and Figure 2.3(b) show the fundamental mode profiles for SCFs with different core diameters (1 μm vs 10 μm). As shown in Figure 2.3(a), the longitudinal electric field E_z is much smaller than the total electric field E for a SCF with a small core diameter of 1 μm, so that the light field is still dominated by the transverse components and be confined very well in the core. The longitudinal electric field E_z decreases as the fibre core diameter increases, indicating that more light can be confined in the silicon

core for SCFs with large core diameters, as shown in Figure 2.3(b). Thus, the interaction between light and cladding decreases as the fibre core diameter increases. Owing to the large V number, higher-order modes will also be excited when light is coupled into an SCF off-axis or with an incorrect mode diameter for SCFs with large core diameter. The coupling efficiencies for higher-order modes depend on the overlap between the incoming beam and the modes of the fibre. The overlap η can be calculated using [71]:

$$\eta = \left(\frac{Re\int \vec{E_1} \times \vec{H_2^*}\, d\vec{s}}{\int \vec{E_1} \times \vec{H_2^*}\, d\vec{s}}\right)\left(\frac{Re\int \vec{E_2} \times \vec{H_1^*}\, d\vec{s}}{\int \vec{E_2} \times \vec{H_2^*}\, d\vec{s}}\right), \tag{2.15}$$

where $\vec{E_1}$, $\vec{H_1}$, $\vec{E_2}$, $\vec{H_2}$ are the electric and magnetic field of the two modes, and * represents the complex conjugate. Due to the circular geometry of SCFs, LP_{0m} modes can be conveniently excited by increasing or decreasing the focus spot size of the coupling lens, as shown in Figure 2.4. The most important parameter for the fibre modes is the effective mode area (A_{eff}), which is defined as [72]:

$$A_{eff} = \frac{(\int\int_{-\infty}^{\infty} |F(x,y)|^2 dxdy)^2}{\int\int_{-\infty}^{\infty} |F(x,y)|^4 dxdy}. \tag{2.16}$$

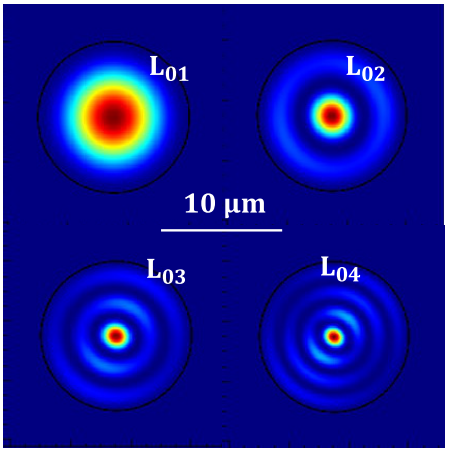

FIGURE 2.4: Profiles of high order modes for a SCF with the core diameter of 10 μm.

The number of modes supported by SCFs can be reduced by reducing the fibre core diameter. As the interest of this thesis focused on fundamental mode, the core diameter of SCFs used in this work were designed in a range of 0.7 μm-2 μm. Figure 2.5 shows the effective mode area (A_{eff}) of the fundamental mode in SCFs as a function of core diameter. Both 1.55 μm and 2 μm wavelengths are analysed because my experimental work mainly focused on these two wavelengths. The small A_{eff} ($\leq$1.6 μm^2) is good for generating high intensity with low pump power for nonlinear interaction processes. Although the A_{eff} for the wavelength of 2 μm is always larger than that of 1.55 μm, it is very close for these two wavelengths due to the tight light confinement of SCFs.

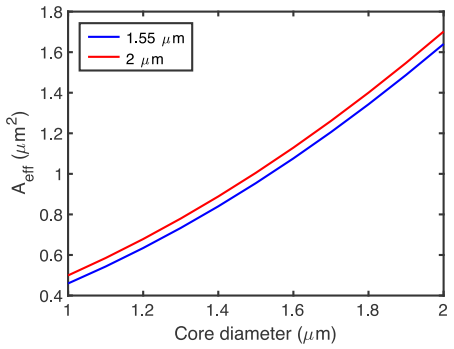

FIGURE 2.5: Effective mode area of fundamental mode in SCFs as a function of core diameter at the wavelengths of 1.55 μm and 2 μm.

2.3 Linear properties in fibres

2.3.1 Propagation losses

The propagation losses are used to describe the light power attenuation when propagating through an optical waveguide, such as a fibre. It can be characterised by using the launched power P_0, fibre length L, and the fibre transmitted power P:

$$P = P_0 \exp(-\alpha L), \tag{2.17}$$

where α is the attenuation constant that describes the losses from all sources. Assuming the fibres have uniform cross-sections, Equation (2.17) can be rewritten by using the light intensity as:

$$I = I_0 e^{-\alpha L}, \tag{2.18}$$

where I_0 is the initial power intensity. In practice, the attenuation constant α is usually expressed in units of dB cm^{-1}, and the unit conversion can be achieved by using the relation of:

$$\alpha_{dB} = -\frac{10}{L}\log(\frac{I}{I_0}) = 4.343\alpha. \tag{2.19}$$

When the light propagates in a transparent medium, such as silicon or silica, the optical attenuation is mainly caused by the material absorption and scattering loss. Figure 2.6(a) shows the silicon absorption loss characterisation results from Ref. [73] by measuring a 10 mm thick silicon plate. The maximum transmission is only ~53 % due to the strong Fresnel reflection loss from the air-silicon interface. By removing the influence of Fresnel reflection, the estimated transmission window of silicon is 1.1-8 μm. When the wavelength is shorter than 1.1 μm, the photon energy is sufficient to span the bandgap energy of silicon atoms (1.1 eV). When the wavelength is longer than 8 μm, the strong light absorption is caused by the molecular vibrations and rotations. Figure 2.6(b) shows the silica absorption loss characterisation results from Ref. [74] by measuring a 10 mm thick silica plate. The low loss transmission window of silica is

below 2.3 μm. When the light wavelength is beyond 2.3 μm, the absorption of silica is strong due to the vibrational resonances. Although the silica cladding of SCFs shows strong material absorption in the mid-infrared, SCFs can still be used in this regime because the tight light confinement in the core can reduce the interaction between the propagating light and silica cladding.

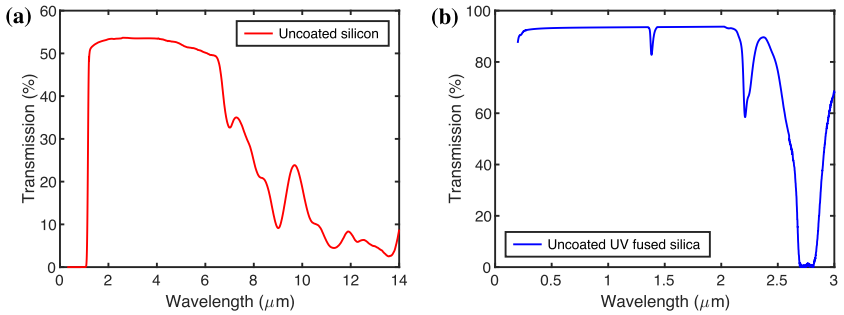

FIGURE 2.6: Material absorption loss characterisation results of (a) silicon [73] and (b) silica [74].

The scattering loss mainly depends on the impurities and imperfections in the optical material. Moreover, the surface roughness at the core/cladding boundary can also introduces the scattering loss. Thanks to the very smooth core/cladding interface of the SCFs, the surface scattering is usually considered to be negligible. Therefore, the scattering loss in a SCF mainly depends on the imperfections in the silicon core, such as cracks and polycrystalline grain boundaries. The scattering loss can be express as a function of wavelength [2]:

$$\alpha_R = \frac{C_R}{\lambda^4}, \tag{2.20}$$

where C_R is a constant related to the properties of material. As the scattering loss decreases as the wavelength increases, SCFs can have lower scattering in the longer wavelength regime. Therefore, it is also treated as a promising platform for mid-infrared regime [44].

2.3.2 Dispersion

The dispersion describes the phase velocity difference in waveguides. It arises primarily due to the interaction between light and electrons of the medium. Generally, there are three kinds of dispersion for a fibre: intermodal dispersion, polarization dispersion and chromatic dispersion. Intermodal dispersion describes phase velocity differences between different fibre modes. As the interest of this work is focused on the behaviour of the fundamental mode, the intermodal dispersion in SCFs is not discussed in this thesis. Polarisation dispersion is caused by the fibre birefringent. Due to the cubic face-centred lattice structure, silicon has vanishing natural birefringence [75], so that it is also not discussed here. Chromatic dispersion is the wavelength dependence of the

phase velocity. From a physical view, the chromatic dispersion is related to the characteristic resonance frequencies at which the medium interacts with the electromagnetic radiation through oscillations of bound electrons. The chromatic dispersion includes material dispersion and waveguide dispersion, which are going to discussed in this section.

Material dispersion

The material dispersion arises from the frequency dependence of refractive index in an optical medium. The refractive index of a material can be approximated as a function of wavelength by the Sellmeier equation [72]:

$$n^2(\lambda, T) = 1 + \sum_{i=1}^{m} \frac{S_i(T)\lambda^2}{\lambda^2 - \lambda_i^2(T)}, \tag{2.21}$$

where S_i is the strength of the resonance feature at λ_i. To calculate the refractive index, the summation is usually approximated by three terms ($m = 3$). By using the parameters from Ref. [76], Figure 2.7(a) shows the calculated refractive index of silicon as a function of wavelength at room temperature ($T = 295$ K). Moreover, Figure 2.7(b) shows the calculated refractive index of silica by using the parameters from Ref. [72].

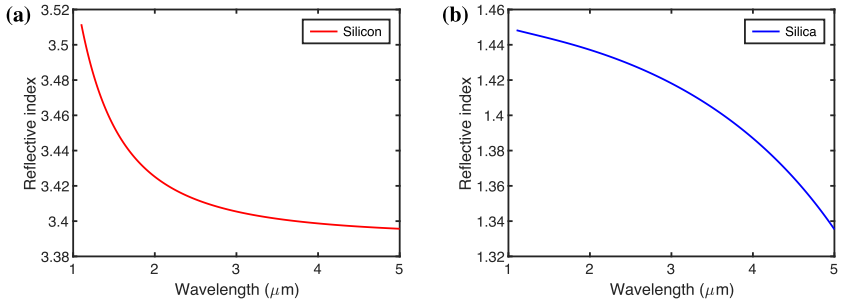

FIGURE 2.7: Reflective index of (a) silicon [76] and (b) silica [77] at room temperature ($T = 295$ K).

To calculate the material dispersion, the light propagation constant β in an optical medium is expanded in a Taylor series around the central frequency ω_0 of the pulse spectrum:

$$\beta(\omega) = n(\omega)\frac{\omega}{c} = nk, \tag{2.22}$$

$$\beta(\omega) = \beta_0 + \beta_1(\omega - \omega_0) + \frac{1}{2}\beta_2(\omega - \omega_0)^2 + \frac{1}{6}\beta_3(\omega - \omega_0)^3 + \cdots, \tag{2.23}$$

where β_i is the i^{th} derivative of β at ω_0, which is also called the i^{th} order dispersion. β_1 and β_2 are related to the refractive index profile as:

$$\beta_1 = \frac{1}{v_g} = \frac{n_g}{c} = \frac{1}{c}(n + \omega\frac{\partial n}{\partial \omega}), \tag{2.24}$$

$$\beta_2 = \frac{1}{c}(2\frac{\partial n}{\partial \omega} + \omega\frac{\partial^2 n}{\partial \omega^2}), \tag{2.25}$$

where n_g is the group index and v_g is the group velocity. As v_g characterises the velocity of the pulse envelope when it propagates in a medium, β_1 governs the speed of the optical pulse envelope. β_2 is called group velocity dispersion (GVD), which is responsible for the pulse envelope spreading. β_3 is the third-order dispersion, which results from the frequency dependency of β_2, and typically acts to induce an oscillatory structure on ultra-short pulses in the time domain [2]. By using the refractive indices of silicon and silica, Figure 2.8(a) and Figure 2.8(b) show the calculated GVD for silicon and silica material, respectively. Due to the wavelength dependence of group velocity, dispersion can also introduces frequency-dependent phase changes for a propagating light pulse. In the normal dispersion region ($\beta_2 > 0$), the group velocity decreases when the optical frequency increases, which results in a positive chirp. In the anomalous dispersion region ($\beta_2 < 0$), the group velocity increases when the optical frequency increases, which causes negative chirps. The introduction of chirp for a light pulse will be discussed in Section 2.5

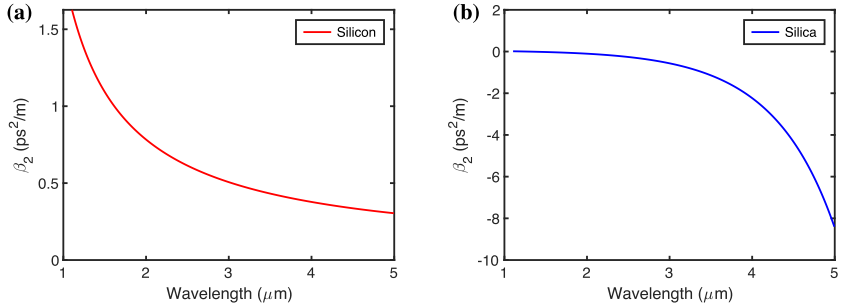

FIGURE 2.8: Calculated GVD for the material of (a) silicon and (b) silica.

Waveguide dispersion

Waveguide dispersion is the chromatic dispersion which arises from the waveguide structure. For example, SCFs have a silicon core, but the fibre dispersion is not equal to the material dispersion of silicon due to the influence of silica cladding. The difference between the material dispersion and the fibre dispersion is caused by the waveguide dispersion effect. As discussed in Section 2.2.2, the effective refractive index (n_{eff}) of the fundamental mode in a fibre can be calculated with Equation (2.12). Then the fibre dispersion can be calculated by using the effective refractive index (n_{eff}) to replace the refractive index (n) in Equation (2.22). By using the same method of material dispersion calculation, Figure 2.9 shows the SCF dispersion (β_2) as a function of wavelength for different core diameters. When the fibre core diameter is large (> 4 μm), the fibre dispersion is close to the silicon material dispersion, which has been shown in Figure 2.8(a). As the core diameter decreases, the role of the cladding dispersion plays

more important role and the fibre dispersion is more close to the silica material dispersion, which has been shown in Figure 2.8(b). An important fibre dispersion parameter is the zero-dispersion wavelength (ZDW), where the GVD is zero. As can be seen in Figure 2.9, the ZDW can be shifted to short wavelengths by tailoring down the core diameter of SCFs. Therefore, the fibre dispersion of SCFs can be engineered conveniently by tailoring the core diameter to satisfy the requirement of nonlinear applications.

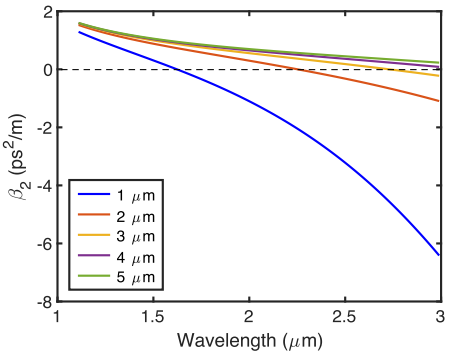

FIGURE 2.9: Dispersion profile of the fundamental mode in SCFs as a function of wavelength for different core diameters, as labelled in the legend.

2.4 Nonlinear properties in fibres

The nonlinear properties of a dielectric medium describes the nonlinear response when interacting with an intense laser beam. Figure 2.10 shows the nonlinear response, which is related to the anharmonic motion of bound electrons under the influence of an applied optical field. The electric field-induced polarisation P depends on the electric field E and the susceptibility χ. For nonlinear optical mediums, the electric polarisation P can be expressed as:

$$P = \epsilon_0(\chi^{(1)}E + \chi^{(2)}E^2(t) + \chi^{(3)}E^3(t)\cdots), \tag{2.26}$$

where $\chi^{(n)}$ is the n^{th} order susceptibility and ϵ_0 is the vacuum electric permittivity. $\chi^{(1)}$ is the linear portion of the polarization, which can be used to express the refractive index and attenuation coefficient as [2]:

$$n = 1 + \frac{1}{2}Re[\chi^{(1)}(\omega)], \tag{2.27}$$

$$\alpha = \frac{\omega}{nc}Im[\chi^{(1)}(\omega)]. \tag{2.28}$$

$\chi^{(2)}$ is the second order susceptibility, which is absent in silicon due to the symmetric crystalline structure of silicon. $\chi^{(3)}$ is responsible for nonlinear effects, including nonlinear absorption and nonlinear refraction, which will be discussed below.

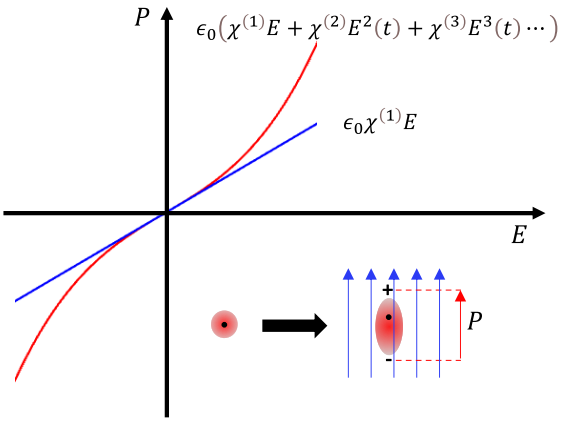

FIGURE 2.10: Schematic of electric field induced nonlinear polarisation of molecules.

2.4.1 Nonlinear absorption

The nonlinear absorption in silicon includes TPA and free carrier absorption (FCA). TPA happens when the total energy of the two injected photons is larger than the bandgap energy of the silicon molecule. Figure 2.11(a) shows a diagram of the TPA process. The two photons can have either the same or different energies, in which case the process is termed degenerate or non-degenerate TPA, respectively. The nonlinear attenuation introduced by TPA process can be described as [78]:

$$\frac{\partial I}{\partial z} = -\beta_{TPA} I^2, \tag{2.29}$$

where β_{TPA} is the TPA coefficient. Equation (2.29) can be solved as:

$$I = \frac{1}{1/I_0 + \beta_{TPA} z}, \tag{2.30}$$

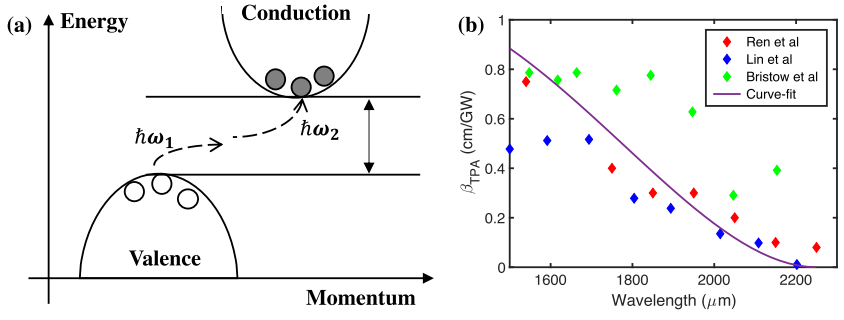

FIGURE 2.11: (a) Diagram of the TPA process in a momentum energy diagram. (b) Measured TPA parameters as a function of wavelength [61].

where z is the propagation length of light. Therefore, the value of β_{TPA} can be characterised by measuring the input and output power. Figure 2.11(b) shows the measured β_{TPA} of silicon material from different research groups. It is worth to note that the TPA

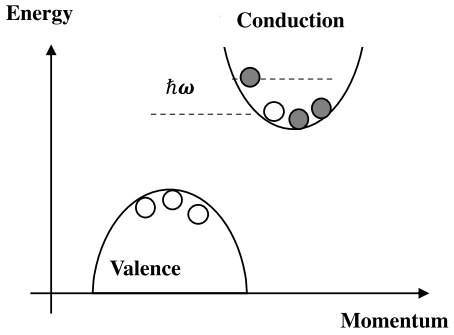

FIGURE 2.12: Diagram of FCA process.

absorption decreases when the wavelength increases, and vanishes beyond 2.2 μm because the total energy of the two photons is not enough to span the bandgap of silicon. Beyond the wavelength of 2.2 μm, three-photon absorption (3PA) starts to dominate the nonlinear absorption, which is a $\chi^{(5)}$ process and follows similar absorption scheme with TPA but is much weaker. The TPA coefficient is related to the imaginary part of $\chi^{(3)}$ and can be expressed as [2]:

$$\beta_{TPA}(\omega) = \frac{3\omega}{2\epsilon_0 n^2 c^2} Im[\chi^{(3)}(\omega)]. \tag{2.31}$$

FCA is another important nonlinear absorption process for silicon. Figure 2.12 shows the diagram of FCA, where an electron absorbs the energy of a photon and rises into a higher energy state within the conduction band. The light attenuation caused by FCA can be described as [2]:

$$I(z) = I_0 e^{-\alpha_{FCA} z}, \tag{2.32}$$

where α_{FCA} is the FCA coefficient, which can be modelled as [79]:

$$\alpha_{FCA} = \frac{q_e^3 \lambda^2}{4\pi^2 \epsilon_0 c^3 n} \left(\frac{N_e}{(0.26 m_0)^2 \mu_e} + \frac{N_h}{(0.39 m_0)^2 \mu_h} \right), \tag{2.33}$$

where N_e, N_h are the density of free electrons and holes, ϵ_0 is the permittivity in vacuum, q_e is the electronic charge, μ_e and μ_h are the mobilities of free carriers, m_0 is the electron rest mass and c is the speed of light. Usually, the density of free electrons and holes are assumed to be equal ($N_e = N_h = N_c$) in the two-band approximation. Therefore, Equation (2.12) can be simplified as:

$$\alpha_{FCA} = \sigma_{FCA} N_c, \tag{2.34}$$

where σ_{FCA} is the FCA coefficient. The refractive index of silicon material can also be modified by free carriers, which is called the free carrier dispersion (FCD) effect. The free carrier coefficient σ which contains both FCA and FCD can be expressed as [80]:

$$\sigma = \sigma_{FCA}(1 + i\mu) N_c, \tag{2.35}$$

where $\mu = 2k_c k_0/\sigma_{FCA}$ governs the FCD and $k_c = 1.35 \times 10^{-27}$ m^3. The free carriers can be modified by the TPA process and can be described via [80]:

$$\frac{\partial N_c}{\partial t} = \frac{\beta_{TPA}}{2\hbar\omega} I^2 - \frac{N_c}{\tau_c}, \tag{2.36}$$

where τ_c is the carrier lifetime.

2.4.2 Nonlinear refraction

Nonlinear refraction describes the intensity dependence of the refractive index when the medium interacts with a high intensity optical field. Due to manipulation from the nonlinear response, the modified refractive index can be written as [2]:

$$n(n, I) = n_{eff}(\omega) + n_2|E|^2, \tag{2.37}$$

where n_2 is the nonlinear index coefficient related to $\chi^{(3)}$ by the relation of [2]:

$$n_2 = \frac{3}{8n} Re(\chi^{(3)}). \tag{2.38}$$

Usually, the nonlinear refractive index modification can be strong when using a high light power. To enhance the nonlinear refraction effects, high power is usually achieved by using ultrashort pulse lasers.

2.5 Ultrashort pulses

Ultrafast pulses are typically used to generate high peak powers. These pulses usually have pulse durations on the order of picoseconds (10^{-12} s) or femtoseconds (10^{-15} s), so that the laser peak powers can achieve kilowatt or even megawatt levels. The electric field of an optical pulse can be described as the product of an envelope $A(t)$ with a phase $\phi(t)$:

$$E(z, t) = A(z, t) \exp i\phi(z, t). \tag{2.39}$$

To study the pulse evolution more conveniently, a frame of reference that moves with the pulse at the group velocity is used. Within this frame, the time index is transformed as:

$$T = t - \frac{z}{v_g} = t - \beta_1 z. \tag{2.40}$$

One common form of the pulse envelope from a laser source is Gaussian profile, which can be described as:

$$A(z, T)|_{z=0} = \sqrt{P_0} \exp -\frac{(1 + iC)T^2}{2T_0^2}, \tag{2.41}$$

where C is the initial chirp parameter of the pulse, T_0 is the input pulse width at 1/e intensity point and P_0 is the peak power of the input pulse. The temporal chirp of a light pulse is defined as the time dependence of its instantaneous frequency. To study the chirp, the pulse is rewritten as:

$$A(z,T) = |A(z,T)| \exp i\phi(z,T), \tag{2.42}$$

where $\phi(z,T)$ implies that the instantaneous frequency differs across the pulse from the central frequency ω_0. The chirp ($\delta\omega$) is defined by the time derivative as [2]:

$$\delta\omega(T) = -\frac{\partial\phi}{\partial T}. \tag{2.43}$$

Another important parameter of optical pulses is the pulse duration, which is usually defined by the full width at half maximum (FWHM) of the optical power in time domain. The FWHM for a Gaussian pulse can be calculated as:

$$T_{FWHM} = 2\sqrt{\ln 2}T_0 \approx 1.665T_0. \tag{2.44}$$

Another common form of pulse envelope from a laser source is hyperbolic secant profile, which can be described as:

$$A(z,T)|_{z=0} = \sqrt{P_0}sech(\frac{T}{T_0}) \exp(-\frac{iCT^2}{2T_0^2}). \tag{2.45}$$

The FWHM of the pulse envelope with a hyperbolic secant profile can be calculated as:

$$T_{FWHM} = 2\ln(1+\sqrt{2})T_0 \approx 1.763T_0. \tag{2.46}$$

2.5.1 Nonlinear Schrödinger equation

When the pulse propagates in a nonlinear medium, dispersion, loss and nonlinear effects all play important roles for the pulse evolution. The pulse propagation in a waveguide can be described by the nonlinear Schrödinger equation (NLSE) [58]:

$$\frac{\partial A}{\partial z} + \frac{i\beta_2\partial^2 A}{2\partial T^2} + \cdots + \frac{\alpha+\sigma}{2}A = i\gamma|A|^2A, \tag{2.47}$$

where γ is the nonlinear coefficient, which relates to the nonlinear refractive index n_2 and the TPA coefficient β_{TPA}:

$$\gamma = \frac{2\pi n_2}{\lambda A_{eff}} + \frac{i\beta_{TPA}}{2A_{eff}}. \tag{2.48}$$

The NLSE can be solved by the split-step Fourier method numerically. Figure 2.13 shows the main idea of it, where the propagation of light happens in two separate

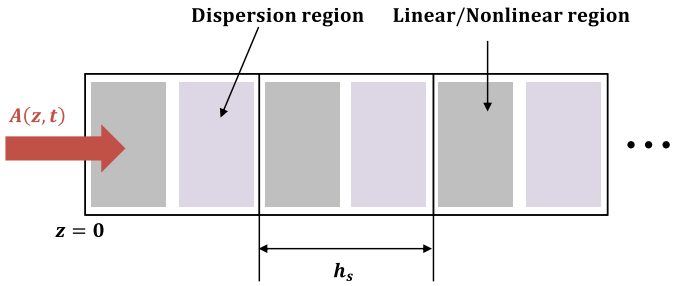

FIGURE 2.13: Schematic of the split-step Fourier method for NLSE solving.

steps, the dispersion only region and the linear/nonlinear region. Hence, the NLSE can be numerically solved in the split steps. In this case, the NLSE is given as:

$$\frac{\partial A}{\partial z} = (\hat{D} + \hat{N} + \hat{L})A, \tag{2.49}$$

where $\hat{D}$ governs the dispersion, $\hat{N}$ represents the nonlinear parts, $\hat{L}$ describe the linear loss terms. These three operators are given as:

$$\hat{D} = \sum_{m\geq 2}^{\infty} \frac{i^{m+1}\beta_m \partial^m}{m!\partial T^m}, \tag{2.50}$$

$$\hat{N} = i \cdot (\frac{2\pi n_2}{\lambda A_{eff}} + \frac{\beta_{TPA}}{2A_{eff}})|A|^2, \tag{2.51}$$

$$\hat{L} = -\frac{\alpha}{2} - \frac{\sigma}{2}(1 + i\mu)N_c. \tag{2.52}$$

In the dispersion step, the influence from dispersion is calculated in the frequency domain. Then in the nonlinearity step, linear and nonlinear influence are calculated in the time domain. The whole fibre is divided with the same step length h_s, which is set small enough to get exact results. In each step, the corresponding operator is applied to solve the NLSE, with the output used as the input for the next step. The split-step method can provide a accurate description for the pulse propagation when the step length is set to be small enough, where the simulation results are consistent when decrease the step length further. As the fibre length changes, either dispersion or nonlinear effects can play the dominate role. To study the fibre length scales L over which dispersion or nonlinear effects become more important for the pulse evolution, the dispersion length L_D and the nonlinear length L_{NL} are introduced here as [2]:

$$L_D = \frac{T_0^2}{|\beta_2|}, \tag{2.53}$$

$$L_{NL} = \frac{1}{\gamma P_0}. \tag{2.54}$$

When $L \ll L_{NL}$ and $L \ll L_D$, neither dispersive or nonlinear effects play a significant role during pulse propagation. When $L \ll L_{NL}$ and $L \sim L_D$, the pulse evolution is

governed by the dispersion in time domain, and the nonlinear effects play a relatively minor role. When the fibre length is such that $L \ll L_D$ and $L \sim L_{NL}$, the pulse evolution is governed by the nonlinear effects in frequency domain.

2.5.2 Dispersion effects

To investigate the effects introduced by dispersion when the pulse propagates in a fibre, the linear and nonlinear part of the NLSE are set to zero by assuming the fibre have a negligible linear loss and a length that satisfies $L \ll L_{NL}$. Then the NLSE is simplified as:

$$i\frac{\partial A}{\partial z} = \frac{\beta_2}{2}\frac{\partial^2 A}{\partial T^2}. \tag{2.55}$$

Although higher order dispersion can also influence the pulse evolution in the time domain, it is not included because β_2 plays more dominated role than higher order dispersion. Equation (2.55) can be solved in the frequency domain and the solution can be expressed as:

$$A(z,\omega) = A(0,\omega)\exp(\frac{i\beta_2\omega^2 z}{2}). \tag{2.56}$$

The spectrum of the short pulse is maintained during the propagation as $|A(z,\omega)| = |A(0,\omega)|$. However, the pulse envelop in time domain varies, which can be obtained using inverse Fourier transform of Equation (2.56):

$$A(z,T) = \frac{1}{2\pi}\int A(z,\omega)e^{i\omega T}d\omega. \tag{2.57}$$

By using a Gaussian shaped input pulse, which can be expressed by Equation (2.41), and assuming there is no chirp ($C = 0$) for the initial pulse, Figure 2.14 shows the pulse evolution when propagating along different lengths ($z = 0$, $z = 2L_D$, $z = 4L_D$). The pulse is broadening as the fibre length increases and the peak power decreases.

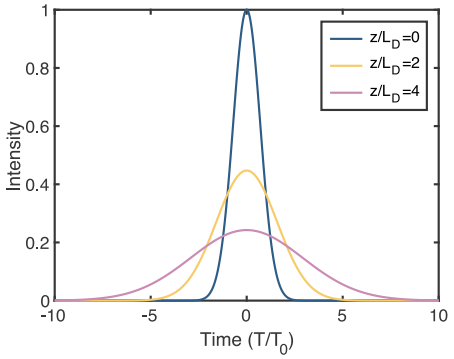

FIGURE 2.14: Normalised intensity $|A|^2$ as a functions of T/T_0 for a Gaussian pulse propagating in a fibre at different lengths.

2.6 Self-phase modulation

SPM is the most fundamental $\chi^{(3)}$nonlinear phenomenon where the phase of an intense ultrashort pulse is modulated by the nonlinear refraction. To study SPM, the linear loss and the dispersion term of the NLSE is neglected:

$$\frac{\partial A}{\partial z} = i\gamma|A|^2 A. \tag{2.58}$$

The solution of Equation (2.58) is:

$$A(z,T) = A(0,T)e^{i\phi_{NL}}, \tag{2.59}$$

where ϕ_{NL} is the nonlinear phase shift, which can be expressed as:

$$\phi_{NL}(z,t) = \frac{z}{L_{NL}}|A(0,T)|^2. \tag{2.60}$$

The spectral changes induced by SPM are caused by the time dependence of ϕ_{NL}. The difference $\delta\omega$ is given by:

$$\delta\omega(z,t) = -\frac{\partial\phi_{NL}}{\partial T} = -\frac{z}{L_{NL}}\frac{\partial|A(0,T)|^2}{\partial T}. \tag{2.61}$$

As the time dependence of $\delta\omega$ is refered to as frequency chirping, the new frequency components are continuously generated when the pulse propagates along the fibre. Figure 2.15 shows the spectral evolution of a 1 ps Gaussian pulse at $\lambda = 1.55$ μm, where the new frequencies are continuously generated along the propagation length. When the pulse propagates through a length of $10L_{NL}$, the new frequencies are generated at two sides of the central waveleneth. A useful function of SPM is that it can be used to estimate the value of nonlinear parameter γ by measuring the resulting spectral broadening, which will be discussed in Section 3.7.2.

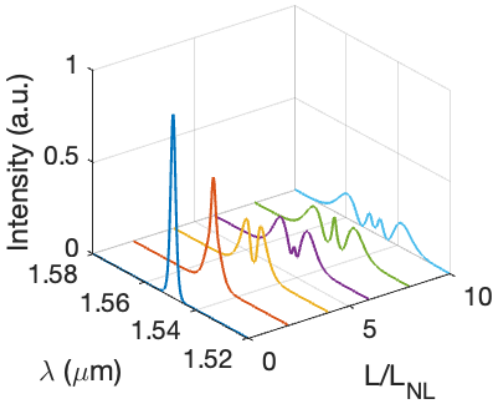

FIGURE 2.15: Spectral evolution of SPM for a 1 ps Gaussion pulse at 1.55 μm.

2.7 Raman scattering

Raman scattering is another $\chi^{(3)}$ nonlinear phenomenon. It belongs to stimulated inelastic scattering because the optical field transfers part of its energy to the nonlinear medium. The stimulated inelastic scattering in SCFs includes Raman scattering and Brillouin scattering. Although both Raman and Brillouin scattering have compelling opportunities for applications, the observation of Brillouin processes in silicon nanophotonics has proven difficult because large optical forces and tight confinement of both phonons and photons are required, which are not met in conventional silicon waveguides. Impressive stimulated Brillouin amplification and lasering and lasering only demonstrated by using complex suspended silicon nanowire structures to achieve tight confinement for light and sound, and therefore maximizing photon-phonon coupling [81, 82]. Moreover, the frequency shift of the Brillouin process in silicon waveguides is very small (1-18 GHz), thus the pump and signal are very close in the spectrum and high-resolution heterodyne detection is needed to measure the stimulated Brillouin gain [83].

Therefore, here I focus on Raman scattering, which comes from photon-phonon interactions in an optical medium and where the incident photons are scattered from the vibrational modes of the material molecules. Figure 2.16 shows the energy level diagrams of Raman scattering, which includes Stokes scattering process and anti-Stokes scattering process. In the Stokes process, the pump photon (ω_p) excites the vibrational quanta in the medium. A red shifted Stokes photon (ω_S) is generated. In the anti-Stokes process, the pump photon absorb an optical phonon generated by the Stokes process and results in a blue-shifted anti-Stokes photon (ω_{AS}). The anti-Stokes process is much weaker than the Stokes process because the generation of an anti-Stokes wave needs phonons generated by Stokes process. To study Raman process, energy transfer from the pump pulse to Stokes and anti-Stokes waves should be included in the nonlinear refractive index of Equation (2.37), therefore:

$$\Delta n(\omega) = n_2 \int_0^\infty R(t')|E(r, t-t')|^2 dt' + \frac{i\alpha}{2k_0}. \tag{2.62}$$

Then the NLSE should be modified by introducing frequency dependence for both α and n_2, which can be included by writing γ and α in the form:

$$\gamma(\omega) = \gamma(\omega_0) + \gamma_1(\omega - \omega_0), \tag{2.63}$$

$$\alpha(\omega) = \alpha(\omega_0) + \alpha_1(\omega - \omega_0), \tag{2.64}$$

where $\gamma_1 = \partial\gamma/\partial\omega$ and $\alpha_1 = \partial\alpha/\partial\omega$. Both of them are evaluated at $\omega = \omega_0$. Therefore, the NLSE can be modified to a more generalised format which includes the Raman

processes as:

$$\frac{\partial A(z,t)}{\partial z} + \frac{1}{2}(\alpha(\omega_0) + i\alpha_1\frac{\partial}{\partial t})A(z,t) - \sum_{n=1}^{\infty}\frac{i^n\beta_n\partial^n A(z,t)}{n!\partial t^n} = i(\gamma(\omega_0) + i\gamma_1\frac{\partial}{\partial t})(A(z,t)\int_0^{\infty} R(t^{'})|A(z,t-t^{'})|^2 dt^{'}), \tag{2.65}$$

where $R(t)$ is the nonlinear response function and can be expressed as [2]:

$$R(t) = (1 - f_R)\delta(t) + f_R h_R(t), \tag{2.66}$$

and f_R is the fractional contribution of the delayed Raman response to the nonlinear polarisation. $h_R(t)$ is the Raman response function, which can be approximated by an exponentially decayed sinusoidal function as:

$$h_R(t) = \frac{\tau_1^2 + \tau_2^2}{\tau_1^2\tau_2^2}\exp(-\frac{t}{\tau_2})\sin(-\frac{t}{\tau_1}), \tag{2.67}$$

where τ_1 is the phonon lifetime and τ_2 is the damping time of the Raman process.

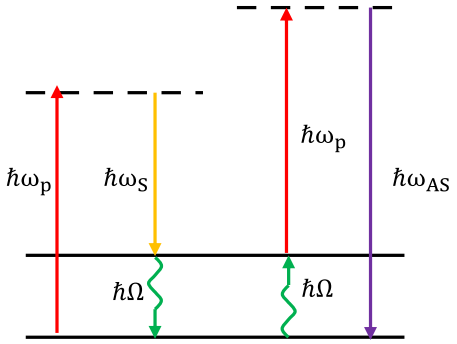

FIGURE 2.16: Energy level diagrams of Stokes and anti-Stokes wave generation via Raman scattering. ω_p, ω_S, ω_{AS} and ω represent frequencies of the pump, Stokes and anti-Stokes photons and frequencies of phonon, respectively, and $\hbar$ is the reduced Planck constant.

2.8 Four-wave mixing

FWM is also an important $\chi^{(3)}$ nonlinear parametric process. As shown in Figure 2.17, two pump photons (ω_p & ω_q) are annihilated to create photons at new frequencies (ω_s & ω_i) in FWM. In order to be efficient, the process must conserve energy and momentum during the interaction. The conservation of energy can be expressed as:

$$\omega_p + \omega_q = \omega_s + \omega_i, \tag{2.68}$$

which is automatically satisfied. The conservation of momentum is also known as phase matching condition. To study the phase matching condition, the phase mismatch

between the involved waves can be expressed as:

$$\Delta k = \beta(\omega_s) + \beta(\omega_i) - \beta(\omega_p) - \beta(\omega_q). \tag{2.69}$$

Significant FWM occurs only when the phase mismatch nearly vanished ($\Delta k \approx 0$). The phase mismatch term Δk includes linear phase mismatch (Δk_L) and nonlinear phase mismatch (Δk_{NL}):

$$\Delta k = \Delta k_L + \Delta k_{NL}. \tag{2.70}$$

The linear phase mismatch Δk_L can be calculated by using the Taylor expansion of β, as has been done in Equation (2.23). By using the expansion and retaining the GVD (β_2) and fourth-order dispersion (β_4) terms, Δk_L can be expressed as [84]:

$$\Delta k_L = \beta_2 \Delta\omega^2 + \beta_4 \Delta\omega^4/12, \tag{2.71}$$

where $\Delta\omega = |\omega_p - \omega_s| = |\omega_q - \omega_i|$ is the frequency difference between the signal/idler and the pump waves. Δk_{NL} arises due to the nonlinear refractive index variation after the light interacts with the nonlinear medium, which can be expressed as:

$$\Delta k_{NL} = \gamma(P_p + P_q). \tag{2.72}$$

It is obvious that the nonlinear term Δk_{NL} is always positive. To realise phase matching for FWM, a suitable negative linear term Δk_L is needed, which can be achieved via dispersion engineering. The frequencies of the two pump photons can be either the same or different, which is known as degenerate and nondegenerate FWM. Due to the value of Δk_{NL} in SCFs is usually small, strong FWM usually happens when the pump wavelength is close to the ZDW ($\beta_2 = 0$).

The FWM can be either a spontaneous or stimulated process. The benefit of spontaneous FWM is that the generated photon beams exhibit high entanglement and can be used as a quantum source. Although stimulated FWM can not be used to generate entangled photon beams, the emission efficiency is much higher, and the generated photon beams have high amplitude and phase correlations. For degenerate FWM, the

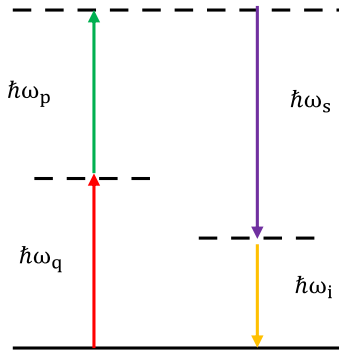

FIGURE 2.17: Energy level diagram of four-wave mixing.

correlation between the two generated beams can be expressed as [2]:

$$|A_i| \propto |A_p|^2 \cdot |A_s|, \tag{2.73}$$

$$\phi_i = -\phi_s. \tag{2.74}$$

Chapter 3

Tapered Silicon Core Fibre

3.1 Introduction

In this chapter, the tapered silicon core fibres are introduced. Firstly, the fabrication method of silicon core fibres is presented. Secondly, the tapering technique used to enhance the nonlinear performance of the as-drawn fibres is introduced, and its benefits for reducing the transmission loss are also discussed. Thirdly, the polishing process used to prepare the coupling facets, necessary to undertake the optical measurements in the multimaterial fibres, is outlined. Finally, the linear and nonlinear characterisation of tapered silicon core fibres is discussed.

3.2 Molten core drawing method

The SCFs used for this thesis were produced by our collaborators from Clemson University and the Norwegian University of Science and Technology. The MCD method was used for the fibre fabrication, whereby a precursor core phase melts at the drawing temperature and the soft cladding glass encapsulates it [85]. The MCD method is similar with traditional fibre tower drawing method, which includes the preform fabrication process and the fibre drawing process. To form a SCF preform, a very thin CaO layer was also introduced to coat the inside of a silica tube. The most important function of CaO is to prevent the diffusion of oxygen from the silica cladding to the silicon core in high drawing temperature. A typical silica tube has an outer diameter of 4 mm and an inner diameter of 2 mm with a length of 200 mm. To ensure uniformity of the interface layer, CaO formed hydroxides was used to prepare the uniform interface layer via an aqueous route [47]. Then the silicon rod was placed into the silica tube, of which the lower end and upper end were sealed to hold the core in place and prevent the oxygen incorporation from air.

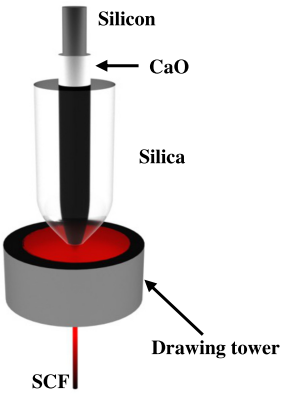

FIGURE 3.1: Schematic of the molten core drawing method.

Figure 3.1 shows the subsequent drawing process. The whole preform is loaded into a furnace, where the temperature is sufficiently high (approximately 1950 °C) to make sure the silicon rod is molten and the cladding is softened. The drawing speed is 60-150 metres per min and the as-drawn fibre can have a length of hundreds of metres. As the CaO material is softer (Mohs hardness of 4.5) than either silicon or silica (Mohs hardness of 7), it can also minimise the internal stress caused by the thermal expansion mismatch between the silicon core and silica cladding during the heating and cooling dynamic. Figure 3.2(a) shows images of an as-drawn SCF with the silica cladding removed. Thanks to the CaO layer, the oxidation can be minimised during the drawing process and the as-drawn SCFs showed a high-quality silicon core with a smooth side surface. Moreover, as the internal expansion was also be minimised by the CaO interface, the as-drawn SCFs showed excellent mechanical strength, which can be seen via the fibre in Figure 3.2(b). Figure 3.2(c) shows the surface quality of the silicon core. The striations in the expanded and contrast-enhanced inset arised from the eutectic of CaO-SiO_2, which has a thickness of $\sim$100 nm. Due to the relatively thin thickness and the graded refractive index, deterioration of the optical properties caused by the interface layer is negligible. However, the core diameter ($\sim$12 μm) of these as-drawn SCFs is still too large for nonlinear applications, and their transmission losses are typically very high (>10 dB cm^{-1}) due to the defects in the poly-Si core. Thus, the as-drawn SCFs were post-processed with a tapering technique to reduce the fibre core diameter and optimise the quality of silicon core.

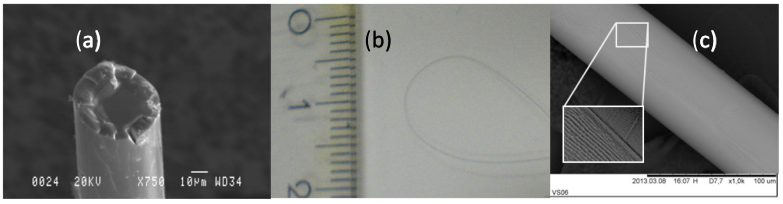

FIGURE 3.2: (a) Image of as drawn SCF with silica cladding removed. (b) Mechanical strength testing of the SCFs. (c) SEM image of the silicon core surface [47].

3.3 Tapering technique

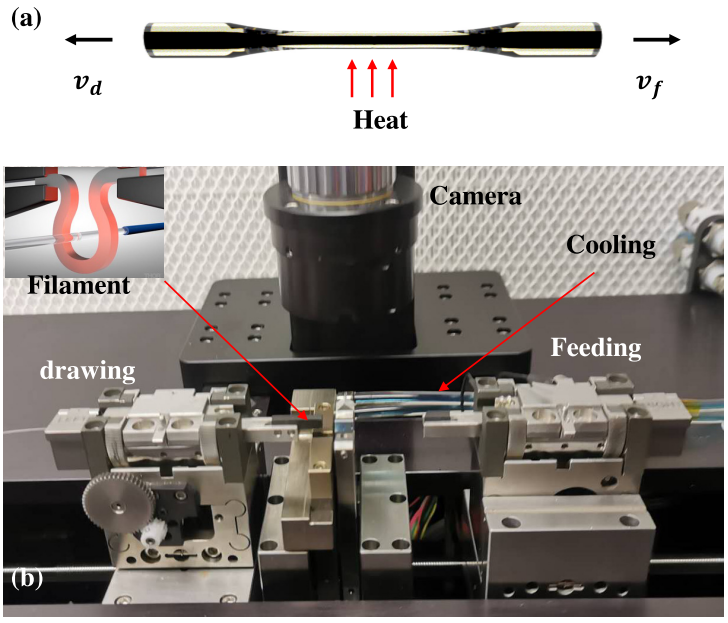

FIGURE 3.3: (a) Schematic of the tapering process. (b) Photo of the Vytran GPX-3300 glass processor.

Tapering was initially applied for semiconductor fibres with Ge materials in the core before subsequently being applied to a SCF in Ref. [54]. The results in Ref. [54] suggests that the tapering technique can not only modify the fibre core dimension, but also reduce the transmission losses by improving the crystallinity of SCFs. Figure 3.3(a) shows the tapering process, where the two ends of an as-drawn SCF is drawn after the fibre is heated. By controlling the drawing (v_d) and feeding speed (v_f), the as-drawn SCFs can be tailored to have different core diameters. The tapering technique is a similar process to the MCD method, but uses lower heating powers and slower drawing speeds because the core diameter of as-drawn fibre is much smaller than that of a fibre preform. In this thesis, the tapering rig is an automated glass processor (Vytran GPX-3000). As shown in Figure 3.3(b), the Ω shaped filament-based heater of Vytran system can produce uniform heating when tapering the as-drawn SCFs. A cooling system connected with the filament holder was used to ensure the stabilisation of tapering temperature. The two ends of the as-drawn SCFs were fixed on two movable stages, which can produce precise drawing and feeding speeds according the the system settings. Moreover, the two stages can also precisely adjust the rotation and pivot of the fibres for alignment. A CCD camera was used to check the fibre profile and quality from the top view of the filament head before processing the SCFs.

3.3.1 Two-step tapering method

Due to the small target core diameters (<2 μm) for my experiment, I have developed a two-step tapering method to taper the initial as-drawn SCFs, which have a large core diameter of ~12 μm. Compared to the single-step tapering, two-step tapering can use a lower heating power for the second step, which is very important for producing a high-quality single-crystal like silicon core over long lengths [55]. Moreover, the tapering ratios of the two-step tapering is smaller than the one-step tapering method, so that the tapering region can better satisfy adiabatic transition and reduce the insertion loss of the tapered SCF. Usually, I targeted a tapering ratio of $D_{initial}/D_{final} = 125/50$ to get tapered SCFs with a core/cladding diameter of 4.8 μm/50 μm in the first step. In the second step, I set the ratio according to the target waist diameter. For example, to get SCFs with a core diameter of 1.5 μm, the $D_{initial}/D_{final}$ of the second step is set to 80/25. Here, the $D_{initial}$ in the second step is not equal to the D_{final} in the first step because of the setting limitation of Vytran system ($D_{initial} \geq 80$ and $D_{final} \geq 10$), but the core/cladding ratio is contained with the designed dimensions. To ensure a good tapering quality in the down and up tapered regions, they are set to a length of 3 mm in the second step tapering step. Due to the high refractive index contrast between the SCF core and cladding, the fibers can support sharp taper transitions whilst still maintaining the adiabatic condition. As discussed in Ref. [86], the requirement of the taper transition is $\theta \leq 0.2$ for silicon waveguides, therefore:

$$tan\theta = \frac{D_{initial} - D_{final}}{L} \leq 0.2, \tag{3.1}$$

where L is the length of tapering region. By using Equation (3.1), the minimum length of tapering region to ensure a adiabatic transition is estimated to be tens of micrometres, thus the length of tapering region (3 mm) for tapered SCFs is long enough to obtain low-loss adiabatic transition.

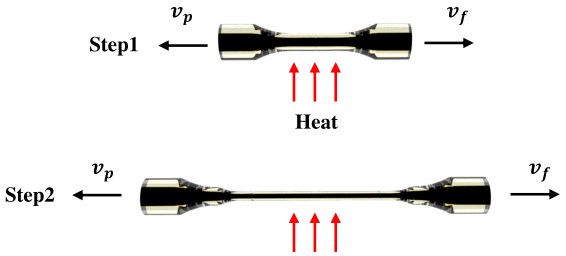

FIGURE 3.4: Schematic of the two-step tapering method.

3.3.2 Tension monitor for tapering

To have a better idea if the heating power is suitable or not, I used a tension monitor view during the tapering process. The tension monitor is a tool of Vytran system that

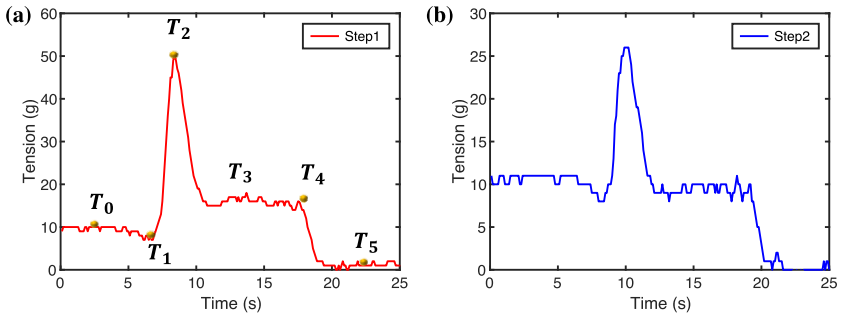

FIGURE 3.5: Fibre tension view of (a) the first step tapering and (b) the second step tapering.

can track fibre tension variation. According to the tension, I can know if the heating power is too high or too low. For example, if the heating power is too high, the fibre tension is very small because the fibre would be too soft to be held straight; and if the heating power is not enough, the fibre tension would be very large and the fibres could be broken. As an example, Figure 3.5 shows the tension view for tapering a 1.5 μm core diameter fibre with a waist region of 1 cm by using the as-drawn SCFs with a core/cladding diameter of 12 μm/125 μm. The tapering process in tension view can be divided into 6 parts: T_0 is the initial tension before the tapering process, which I usually target a tension of 10 g to ensure the fibre is totally straight. T_1 represents the tension when the fibre is fully softened, which is a little lower than T_0. Then the tension would go up to the maximum tension of T_2 when the fibre is starting to be drawn by the left stage and the down-tapering region is being formed at the same time. According to my experience, T_2 should be $\sim$60 g for the first step and $\sim$30 g for the second step for good quality tapering. T_3 shows the tension when forming the waist region, which should be as flat as possible during the tapering. Either too high or too low heating power will make T_3 unstable during the waist growing process. T_4 represents the end of waist tapering and the start of the up-tapering region and T_5 is the tension after the whole tapering process is finished.

Table 3.1 summaries the parameters for the two-step tapering process. The heating power for the second step is 10 W lower than the first step, which is good to produce high-quality silicon cores. It should be noted that the heating power should be adjusted according the drawing tension variation because the filament condition can change

TABLE 3.1: Tapering settings for 1.5 μm core diameter fibre with 1 cm waist length.

Parameter	Symbol	Step1	Step2
Start core size (μm)	$D_{initial}$	12	4.8
End core size (μm)	D_{final}	4.8	1.5
Tapering ratio	$D_{initial}/D_{final}$	125/50	80/25
Waist length (mm)	L	10	10
Heating power (W)	P	65	55
Drawing speed (mm/s)	v_d	1	1

from time to time. Another important tapering parameter is the drawing speed, which is 1 mm s^{-1} for all of my fibre fabrications in this thesis.

3.4 Crystallinity of tapered silicon core fibres

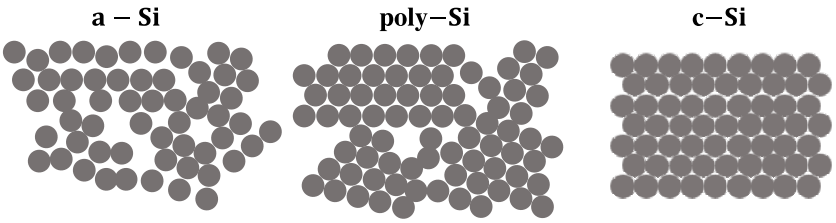

FIGURE 3.6: Common allotropes of silicon material.

There are three common types of silicon: a-Si, where the silicon atoms are arranged in a random order; crystalline silicon (c-Si), where the atoms are arranged orderly; and poly-Si, which is a mixture of small crystal grains. To study the role of tapering in the material quality optimisation, Figure 3.7 shows XRD measurement results for both the as-drawn fibre and the tapered SCFs from Ref. [55]. It is clear that the as-drawn SCF was made up of several millimetre-long crystal grains. Some of them are overlapped, which results in large scattering losses between the crystal grains. After tapering, the tapered region is found to consist of only a single-crystal grain which extends over a length of 9 mm. Due to the optimised crystal quality, the measured propagation loss of the as-drawn SCFs was reduced from 10 dB cm^{-1} to less than 2 dB cm^{-1}. However, this propagation loss is still far from the lowest loss of high-quality on-chip silicon waveguides (4 dB m^{-1} in Ref. [87]) due to the imperfections of the tapered SCFs.

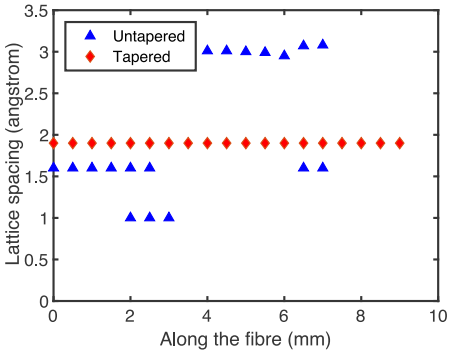

FIGURE 3.7: Lattice spacing of diffraction spots measured via XRD along the as-drawn fibre (blue) and a tapered waist (red) [55].

3.5 Facet preparation

3.5.1 Capillary mounting method

Due to the material properties of poly-Si, it is difficult to get a high-quality fibre facet via the traditional fibre cleaving process. An alternative solution is fibre facet polishing method. However, the tapered SCFs used in this thesis usually have a small cladding diameter (10∼30 μm) over a length of a few centimetres, so that the fibre mechanical strength is not strong enough for a standard polishing process. To enhance the mechanical strength of the tapered SCFs for the fibre polishing process, I use a capillary to mount the fibres. Figure 3.8(a) shows the capillary mounting method for tapered SCFs. The fibre is first inserted into a capillary whose inner diameter is 250 μm and outer diameter is 665 μm. Then one side of the fibre is dragged until the whole tapered SCF is within the capillary. In the end, the excess part of the fibre is cleaved and the capillary is filled with wax (crystal bond 509) to fix the fibre inside the capillary. The wax used in this work has a flow point of 121$^{\circ}C$, which makes it convenient to use a hot plate to melt it into a liquid form to flow through the capillary.

Figure 3.8(b) shows the smooth facet after polishing. The finest polish films used in the experiments have a particle size of 0.5 μm and the polishing system is from ULTRA TEC. Moreover, when the facet is dirty or burnt by the laser, it can be re-polished conveniently. The only disadvantage of this method is that the tapered SCFs cannot accommodate very high pump powers as the melting point of wax is not high. When the wax melts, it can spread over the facet and decrease the coupling efficiency. The degree of heating the wax is related to the average pump power, pumping wavelength and coupling condition. According to my experience, the highest average power that can be used for coupling is estimated to be ∼150 mW at 1.55 μm. To increase the power that can be used for tapered SCFs, our group is testing a new fibre mounting method that uses a silicon chip with a customed V-groove to hold the tapered SCFs, which we hope will increase the usable highest average power to 600 mW.

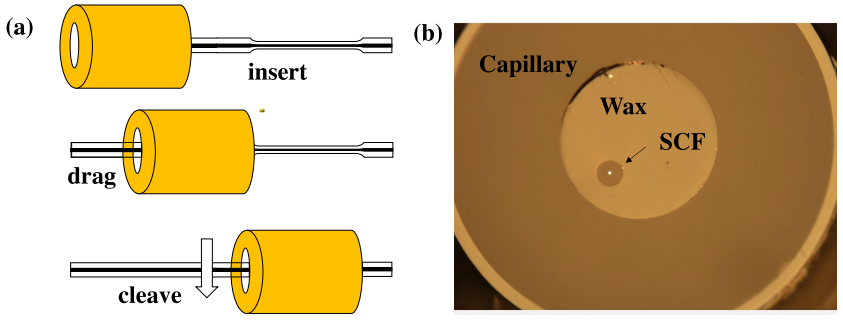

FIGURE 3.8: (a) Schematic of the capillary mounting method for tapered SCF. (b) Image of fibre facet after polishing.

3.5.2 Fibre profiles

Figure 3.9 shows the fibre profile of the tapered SCFs after polishing. To enhance the light intensity for nonlinear applications, the waist diameters of the tapered SCFs used in this thesis were all designed to be less than 2 μm. Due to the small waist diameter, it is difficult to couple light from optical lenses to the fibre waist with high efficiency. Therefore, the taper transitions were retained to target a core diameter for the input and output facet of ~4.6 μm, which can have a better match to the focused spot size of the input beam.

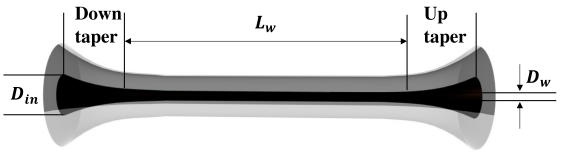

FIGURE 3.9: A schematic of the tapered SCF profile after polishing.

3.6 Linear transmission characterisation

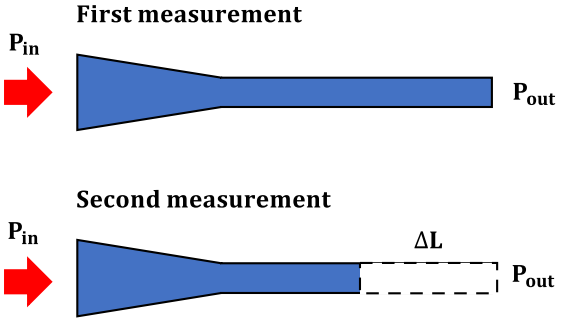

FIGURE 3.10: Schematic of the cutback method for the linear loss measurement of tapered SCFs.

The most popular way to measure the linear losses of the tapered SCFs is using the well-known cutback method. Figure 3.10 shows the measurement process. The output up-tapered transition region was totally removed to ensure the same output coupling. The input down-tapered transition region was retained to ensure high light coupling efficiency to the fibres. The insertion loss difference between each measurement depends on the length of removed section (ΔL). By measuring the fibre insertion loss as a function of fibre length, the propagation loss and coupling loss can be figured out. Figure 3.11 shows the setup for the cut-back measurement. To have a better beam spot size matching with the input core diameter, a 40$\times$ objective lens (OL1, NA: 0.65) was used to coupled light to the tapered SCFs. A beam spliter (BS) was used to guide the light from the reflected input facet of SCF to the camera (CCD_1), which was used to view the coupling condition. To ensure the light was perpendicular to the fibre facet,

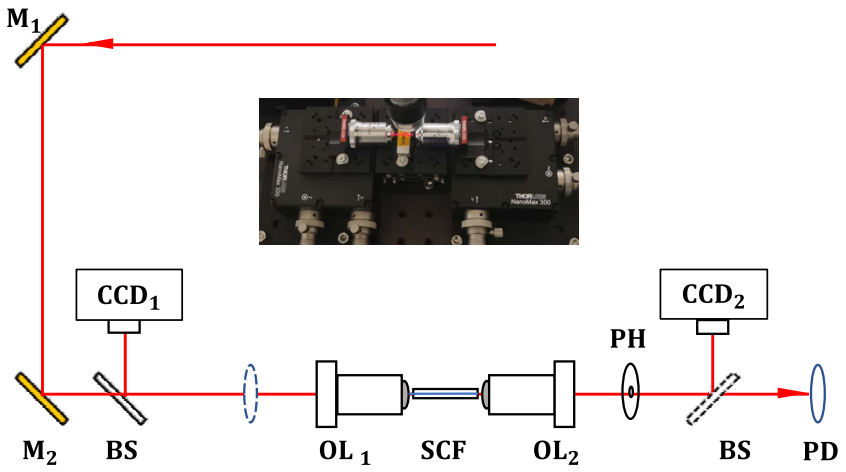

FIGURE 3.11: Schematic of insertion loss measurement setup. M: mirror, BS: beam splitter, CCD: charge-coupled device camera, PD: power detector, OL: optical lens, PH: pinhole.

mirrors (M_1 & M_2) were used to adjust the angle of the incoming light slightly. The output was collected with a 60× optical lens (OL2, NA: 0.85), which has a better light collection efficiency due to the high NA. The camera (CCD_2) at the output side was used to view the output beam profile to ensure the light propagating in the SCF was fundamental mode. The input/output power was measured by the power detectors (InGaAs Photodiode, Thorlabs S132C). A pinhole (PH) was used to filter the light that propagating through the cladding. To ensure the same coupling loss of each measurement, high accuracy XYZ alignment stages (5 nm Theoretical Resolution) were used for the coupling lenses and fibre samples, as shown in the inset.

The fibre used to demonstrate the cutback measurement had a waist diameter of 1.5 μm and a total length of 6.2 cm after the output tapering region was totally removed. By using a CW telecom band laser (TUNICS T100S), Figure 3.12(a) shows the cutback measurement result at the wavelength of 1.55 μm. The linear fitted equation is y=(1.02±0.25)+7.3, so that the propagation loss of this fibre is 1.02 dB cm^{-1} and the coupling loss is 7.3 dB. The estimated linear loss (1.02 dB cm^{-1}) is better than that (2 dB cm^{-1}) in Ref. [61] due to the optimisation of the fabrication process. The coupling

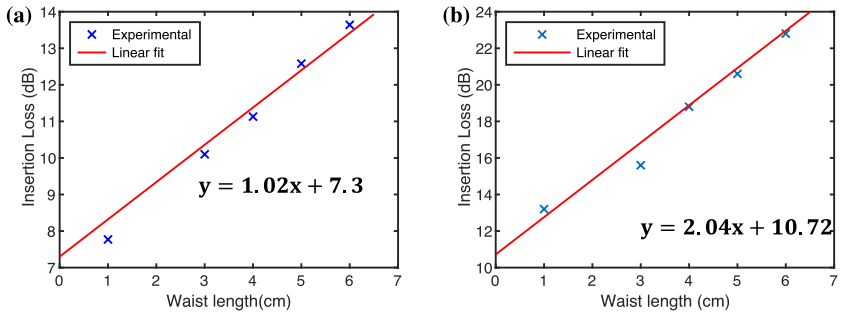

FIGURE 3.12: Cutback measurement results of 1.5 μm core size tapered SCFs at (a) the wavelength of 1.55 μm and (b) the wavelength of 2 μm.

loss mainly includes the losses from the facet reflections, lenses and mode mismatch between the incoming beam and the silicon core. As this project was also interested in the 2 μm regime, a CW mid-infrared laser (Cr^{+2}: ZnS/Se IPG Photonics) was used for a 2 μm cut-back measurement. Figure 3.12(b) shows the cut-back measurement results at 2 μm. The estimated propagation loss of this fibre was 2.04 dB cm^{-1} and the estimated coupling loss was 10.7 dB. The higher propagation loss at 2 μm is caused by the higher absorption loss of silica cladding. The higher coupling loss at 2 μm is most probably caused by the higher lens losses and a greater mode mismatch loss. It worth noting that plenty of tapered SCFs with different waist diameters and lengths were measured by using cut-back method during the early period of this thesis. The similar input/output core diameter and tapering region profiles ensures the coupling losses are similar (7.3 dB at 1.55 μm and 10.7 dB at 2 μm) for tapered SCFs with different waist diameters. Therefore, the fibre propagation loss can be estimated from the measured fibre insertion loss by using the same coupling losses for a given input/output taper design.

3.7 Nonlinear characterisation

For nonlinear effects, the most important two parameters are the TPA coefficient (β_{TPA}) and Kerr nonlinear index (n_2).

3.7.1 Two-photon absorption measurement

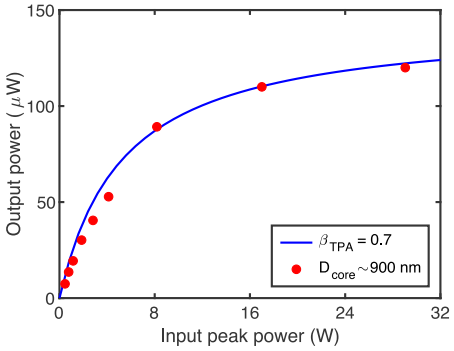

FIGURE 3.13: Two-photon absorption of tapered SCFs with a 900 nm core diameter.

To estimate the value of β_{TPA}, the insertion loss was measured as a function of input power. The fibre lengths are kept short (1 cm) to make sure it is much shorter than the dispersion length ($L_D = T_0^2/|\beta_2|$), so that the influence of dispersion can be ignored. The fibre waist diameter was ~0.9 μm to enhance the nonlinear absorption so that the nonlinear saturation can be measured with a relatively low input power. The nonlinear saturation then can be fitted with a simplified NLSE that only accounts for the decrease in output power [2]:

$$\frac{dI}{dz} = -\alpha I - \beta_{TPA} I^2 - \sigma_{FCA} N_c I, \tag{3.2}$$

where N_c depends on the TPA coefficient β_{TPA} and free carrier lifetime τ_c:

$$\frac{dN_c}{dt} = \frac{\beta_{TPA}}{2\hbar\omega} I^2 - \frac{N_c}{\tau_c}. \tag{3.3}$$

The setup used for the TPA measurement was the same as the linear loss measurement, which has been shown in Figure 3.12. The input source used has a pulse duration of 750 fs and repetition rate of 40 MHz at 1.54 μm so that it could generate a very high peak power to achieve nonlinear saturation. The peak power of the pulsed laser can be calculated from the measured average power:

$$P_p = \frac{P_{av}}{f_r \cdot T_p}, \tag{3.4}$$

where P_{av} is the measured average power, f_r is the repetition rate and T_p is the pulse duration. Figure 3.13 shows the measurement results. To estimate the value of β_{TPA}, the output peak powers were calculated by using Equation (3.2). Table 3.2 summaries the simulation parameters. The linear loss was estimated to 0.8 dB cm^{-1} according to the measurement insertion losses when using a low input power. The simulation curve fits well with the experiment data points and the estimated TPA values was 0.7 cm GW^{-1}, which also agrees with the Z-scan measurement results for bulk crystal silicon material [88].

TABLE 3.2: Simulation parameters for the nonlinear absorption of a tapered SCF.

Parameter	Symbol	Value (unit)
Linear loss	α_l	0.8 dB cm^{-1}
Free carrier lifetime	τ_c	10 ns
TPA coefficient	β_{TPA}	0.7 cm GW^{-1}
Core diameter	D_{core}	900 nm
Effective mode area	A_{eff}	0.41 μm^2
FCA coefficient	σ_{FCA}	1.45 $\times$ 10^{-21} m^2

3.7.2 Kerr index measurement

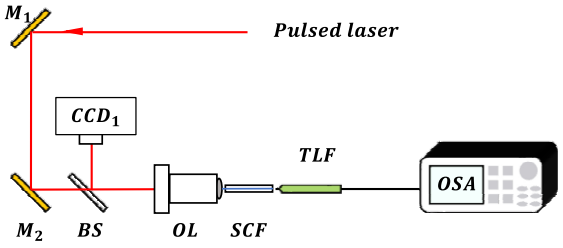

FIGURE 3.14: Schematic of the SPM experimental setup. TLF: tapered lens fibre. OSA: optical spectrum analyser.

For silicon waveguides, the Kerr index (n_2) is usually investigated by measuring the size of nonlinear effects such as SPM [89] or FWM [90] with different power levels.

In this work, the Kerr index was characterised by measuring the spectral broadening induced by SPM. After the linear loss (α) and TPA coefficient (β_{TPA}) have been characterised, n_2 is the only unknown parameter for Equation (2.47). Therefore, the value of n_2 can be estimated by comparing the SPM spectral broadening with the simulation results. Figure 3.14 shows the experimental setup, which is similar to the setup used for the linear loss and nonlinear absorption measurement. However, a tapered lens fibre (TLF) was used to collect light from the output side and to connect with the optical spectrum analyser (OSA) conveniently. The TLF has a focal diameter of 2.5 μm and a working distance of 14 μm to achieve a high coupling efficiency with the tapered SCF, which has a core diameter of ~900 nm with a waist length of 1 cm. This SCF was used for the TPA characterisation experiment previously. Figure 3.15 shows the measurement results. The blue curves represent the experiment results and the red curves are the simulation results by solving Equation (2.47) via the split-step method. The simulation results match well with the measured SPM broadening spectra. The estimated value of n_2 is 5×10^{-14} cm^2 GW^{-1} at 1.54 μm, which also agrees well with the results from other research groups [88]. The excellent characterisation results of nonlinear properties also indicates the high-quality of the silicon core for the tapered SCFs.

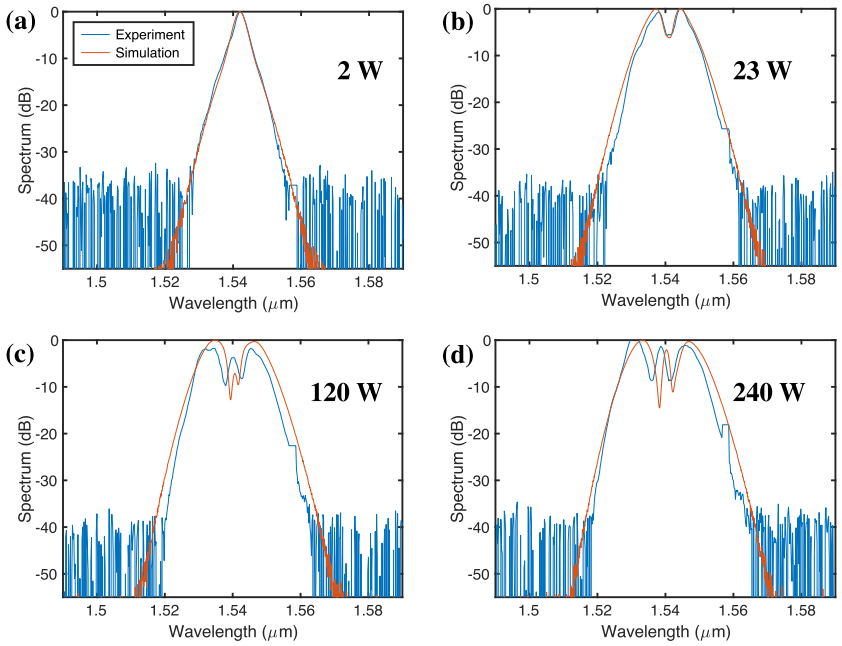

FIGURE 3.15: Experimental SPM spectra for different input peak power (blue lines). The red curves are numerical fits using the NLSE.

3.8 Conclusion

In this chapter, I have introduced the tapered SCFs. Firstly, the MCD method that used to fabricate long lengths of poly-Si core SCF was described. Then the tapering technique that can tailor the fibre core dimension was discussed. Material characterisation shows that this technique can also reduce the fibre transmission loss by recrystallising the poly-Si core to a single-crystal-like material. Thirdly, the fibre facet polishing method for the tapered SCFs was presented. Finally, the optical characterisation methods were described and the results for a typical tapered SCF were presented, including measurements of both the linear and nonlinear parameters. These characterisations indicate that the tapered fibres could have a linear loss around 1 dB cm^{-1} and a nonlinear Kerr index of 5×10^{-14} cm^2 GW^{-1}.

Chapter 4

Raman amplification

4.1 Introduction

In this chapter, Raman amplification in the tapered SCFs is studied. Firstly, spontaneous Raman scattering and stimulated Raman amplification (SRS) are measured in the telecom band with CW pump lasers. Then the study turns to the mid-infrared region to suppress the nonlinear optical loss, so that pulsed pump sources can be considered to obtain a higher Raman gain. Then the Raman gain in these two wavelength regimes are compared and the role of the pump power and fibre length in the Raman amplification process are discussed. Finally, the extension for mid-infrared source generation via cascaded Raman processes is discussed.

4.2 Raman scattering in SCFs

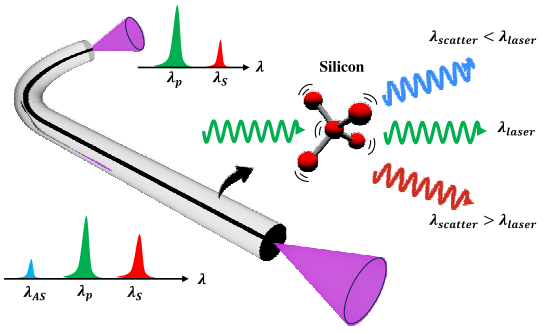

FIGURE 4.1: Schematic of Raman scattering in SCFs.

Figure 4.1 shows a schematic of the Raman scattering process in SCFs, where a delayed $\chi^{(3)}$ nonlinear response is caused by the crystal lattice vibrations. The vibrations are associated with optical phonons when the pump light propagates through the medium.

The Raman emission process can be either spontaneous or stimulated. In the spontaneous Raman scattering, only a pump is injected into the nonlinear medium and new waves are generated at the Stokes and anti-Stokes wavelengths. In the stimulated Raman scattering, a seed is injected together with pump at either the Stokes or anti-Stokes wavelengths. When two laser beams with different wavelengths propagate together through a Raman medium, the longer wavelength beam can experience optical amplification through SRS if the longer wavelength overlaps with the Stokes bandwidth. The energy conservation for Raman scattering processes can be expressed as:

$$\omega_p = \omega_S - \Omega, \tag{4.1}$$

$$\omega_{AS} = \omega_p + \Omega, \tag{4.2}$$

where Ω is the optical phonon frequency, which depends on the intrinsic frequency of the optical phonon in nonlinear materials. The optical phonon frequency for silicon is $\sim$15.6 THz, so that the Raman frequency shifting from the pump to the Stokes or anti-Stokes wave is $\sim$15.6 THz in SCFs. The Raman bandwidth can be calculated from the Raman response time, which is $\sim$3 ps in silicon, corresponding to a Raman emission bandwidth of $\sim$105 GHz. As the momentum conservation between the pump and seed photons are automatically satisfied with the inclusion of optical phonons, the SRS amplification is not restricted by phase-matching considerations. Therefore, Raman scattering can be used to amplify signals within the whole transmission window of nonlinear medium if suitable pump sources are accessible. This property makes it very important for regions where the operating wavelength of traditional amplifiers are limited.

4.3 Literature review

The early research on Raman systems made use of long lengths of low-loss silica fibre due to the low propagation losses [91]. Then the focus shifted to silicon waveguides due to their high damage threshold, strong Raman emission (10^3-10^4 times higher than silica), compact architectures (roughly $\sim$100 times smaller than SMF) and extended infrared transmission (1.1-8 μm) [92, 26, 93, 94]. Raman scattering in the telecom band was one of the first nonlinear processes demonstrated in a silicon waveguide [95], and was closely followed by examples of amplification [96, 92, 97] and lasing [98, 26, 93, 99]. However, to date, the achievable gain in silicon systems within the telecom band has been hindered by the relatively high linear and nonlinear transmission losses. To reduce the linear losses, waveguides with large, micrometre-sized dimensions have been employed, but these have required the use of impractically high coupled pump powers ($\sim$1 W CW laser) to achieve Raman gains up to 2.3 dB due to the reduced light

confinement [100]. Alternately, when using smaller, sub-micrometre waveguide dimensions, both the linear and nonlinear losses play a significant role, and thus, pulsed pump sources or complex carrier sweep-out schemes have been required to reduce the build-up of free carriers to obtain similar levels of gain [101]. Moreover, despite this initial success, and Raman amplification being demonstrated in bulk silicon at 3.4 μm[97], currently Raman amplification or wavelength shifting in silicon waveguides has been confined to wavelengths $<$2 μm, which is attributed to the relatively short device lengths and limited power handling of the on-chip components [98].

In this chapter, I investigate Raman scattering in the tapered SCFs in both the near- and mid-infrared to take advantages of features such as their low propagating losses, extended lengths and efficient coupling to fibre-based sources.

4.4 Telecom band Raman process

Due to realy availability of optical components in telecom band, the Raman system was demonstrated in this region first.

4.4.1 Fibre fabrication and profiles

Owing to the relatively small cross-section for Raman process, in order to enhance the Raman scattering, the fibres were tapered down to a core diameters of $<$1 μm to increase the optical intensity. At the time of this study, these were the smallest optical cores for this class of fibre. Table 4.1 summarises the profiles and optical properties of two SCFs used for the telecoms Raman scattering measurements. The insertion losses for these SCFs were measured using the CW laser diodes at input powers of 1 mW. The Fibre2 was fabricated during the Raman amplification measurement, therefore it is only used for SRS amplification experiment. The fibre lengths is less than 2 cm because I was not yet able to taper longer fibre length with low losses when the Raman experiment was being carried out.

TABLE 4.1: Geometrical parameters and insertion losses for two submicron tapered SCFs used for Raman scattering measurements.

Parameter	Symbol	Fibre1 (unit)	Fibre2 (unit)
Waist diameter	D_w	850 nm	750 nm
Waist length	L_w	10 mm	15 mm
Total length	L	13.5 mm	19.3 mm
Input diameter	D_{in}	4.7 μm	4.6 μm
Output diameter	D_{out}	4.4 μm	4.2 μm
Insertion loss	α	$\sim$10.2 dB	$\sim$8.9 dB

4.4.2 Experimental setup

Figure 4.2 shows the experimental setup to characterise the Raman response for the SCFs in the telecoms band. Two CW laser diodes operating at different wavelengths (1431 nm & 1500 nm) were used as pump sources to characterise the spontaneous Raman emission. The output power of these two sources are ∼110 mW. An external isolator was placed after the pump to avoid light reflection into the diodes. Two conventional TLFs were used to couple the pump light into and out of the SCFs. Compared with free-space lenses, TLFs have a flat frequency response over the wavelength range covering both the Stokes and anti-Stokes wavelengths. To ensure the pump light was primarily launched into fundamental mode of the SCF, the output mode profile was verified using a free space lens and a CCD before using a TLF at the output. A power metre (Thorlabs S148C) and an OSA (YOKOGAWA AQ6370D) were used to measure the optical power and record the output spectra, respectively. To investigate SRS amplification, a signal laser (TUNICS T100s) was injected into the SCF together with the pump using a wavelength division multiplexer (WDM). A polarisation controller (PC) was also used to align the linearly polarised pump and signal beams to optimise the stimulated Raman gain. A second WDM positioned at the output stage was used to filter out the noise caused by the pump diode.

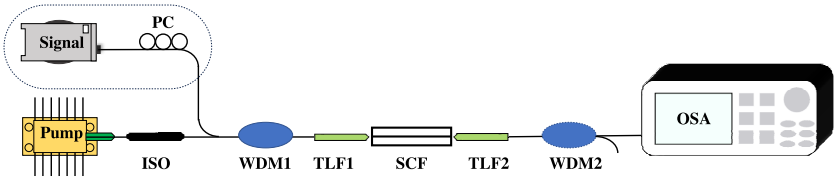

FIGURE 4.2: Schematic of the telecom band Raman system for the tapered SCFs. ISO: isolator. WDM: wavelength division multiplexer.

4.4.3 Spontaneous Raman scattering

Fibre1 in Table 4.1 was used in the initial experiments. The linear loss at 1550 nm was estimated to be 2.1 dB cm^{-1} by subtracting the coupling losses (7.3 dB) from the total insertion loss (10.2 dB). Figure 4.3 shows the recorded Stokes spectra at several values of coupled power for the two different pump wavelengths. The Stokes signals for forward-emitted Raman scattering were generated at 1546.3 nm and 1626.3 nm in Figure 4.3(a) and Figure 4.3(b), matching with the Raman shift of 15.6 THz for crystalline silicon in both instances. The lowest pump power for which the spontaneous Raman scattering can be clearly observed was 3 mW, and the bandwidths of the Stokes signals for the pump wavelength of 1431 nm and 1500 nm were 263.7 GHz and 221.2 GHz, respectively. These bandwidths are slightly larger than the theoretical bandwidth of 105 GHz for silicon, which can be attributed to the finite bandwidth of the pump sources

[95]. Figure 4.3 shows the simulation results (dash line) by solving the general NLSE (Equation (2.65)), which were performed by another group member, Shiyu Sun. Table 4.2 summarises the simulation parameters corresponding to Fibre1. By convolving the pump linewidths with the intrinsic Raman scattering linewidth (105 GHz), the simulations agree very well with the experiments (solid lines), both in terms of the powers and bandwidths. As the maximum pump power used here is still very low (<50 mW average/peak power), the nonlinear absorption was found to be negligible, so that the maximum Stokes powers can be increased further by using pump laser sources with higher maximum output powers [102].

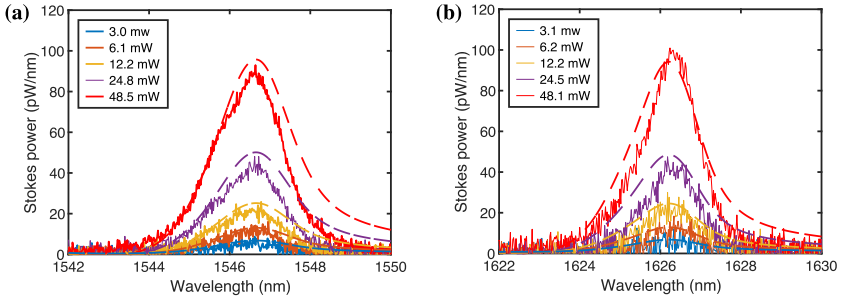

FIGURE 4.3: Spontaneous Raman emission spectra at various pump powers, as given in the legends, for pump wavelengths of (a) 1431nm and (b) 1500 nm.

To estimate the Raman gain coefficient, the relationship between the integrated Stokes power and pump power is considered as [103]:

$$P_S = \kappa L_{eff} P_p, \tag{4.3}$$

where κ is the spontaneous Raman coefficient in units of cm^{-1} and the effective length L_{eff} can be expressed as:

$$L_{eff} = (1 - e^{-\alpha L})/\alpha. \tag{4.4}$$

Figure 4.4 plots the Stokes power as a function of coupled power for the two different pump wavelengths. As expected, the spontaneous emission power depends linearly on the pump power. Figure 4.4 also shows the slope efficiencies (κL_{eff}) for the two pump wavelengths, which are almost the same due to the close pump wavelengths. By using the spontaneous Raman coefficient, the spontaneous Raman efficiency S in the

TABLE 4.2: Simulation parameters for Fibre1 in spontaneous Raman scattering.

Parameter	Symbol	Value (unit)	Value (unit)
Pump wavelength	λ	1431 nm	1500 nm
Linear loss	α_l	2 dB cm^{-1}	2 dB cm^{-1}
Keff effect coefficient	n_2	4.2×10^{-18} m^2 W^{-1}	5.0×10^{-18} m^2 W^{-1}
Carrier lifetime	τ	7.5 ns	7.5 ns
FCA parameter	σ	1.45×10^{-21} m^2	1.45×10^{-21} m^2
TPA coefficient	β_{TPA}	11.77×10^{-12} m W^{-1}	10.79×10^{-12} m W^{-1}
Effective mode area	A_{eff}	0.41×10^{-12} m^2	0.42×10^{-12} m^2

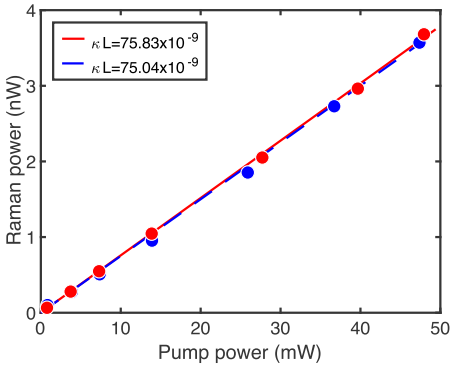

FIGURE 4.4: Spontaneous Raman output power as a function of coupled pump power for the two pump wavelengths of (a) 1431 nm and (b) 1500 nm.

SCFs can then be calculated as:

$$S = \kappa/\Delta\Omega, \tag{4.5}$$

where $\Delta\Omega$ is the effective solid angle for the fundamental mode, which is estimated to be 0.25 Sr^{-1} for a SCF with a waist core diameter of 850 nm by using the commercial software package ModeSolution. Hence, the values of S for the pump wavelengths of 1431 nm and 1500 nm are 3.03×10^{-7} cm^{-1} Sr^{-1} and 3×10^{-7} cm^{-1} Sr^{-1}, respectively. The spontaneous Raman coefficients obtained in these SCFs are similar to previously reported values obtained for nanophotonic silicon waveguides [103], and are at least two orders of magnitude larger than those of standard silica optical fibres [91]. To characterise the ability of using Raman scattering to amplify signals, the Raman gain coefficient g_s is defined as [104]:

$$g_s = \frac{8\pi c^2 \omega_p}{\hbar\omega_S^4 n^2(\omega_S)(N+1)\Delta\Omega}. \tag{4.6}$$

Here, ω_p and ω_S are the angular frequencies of the pump and Stokes, respectively. n is the refractive index at signal wavelength, N is the Bose occupation factor (0.1 at room temperature), $\hbar$ is Planck's constant divided by 2π and $\Delta\Omega$ is the FWHM bandwidth of the Raman response in silicon (105 GHz). Thus, the values of g_s obtained for the pump wavelengths of 1431 and 1500 nm are 29 and 34 cm GW^{-1}, respectively. The values of g_s are consistent with previously reported values obtained for single crystal waveguides, which fall within the range of 20–76 cm GW^{-1} [92, 95, 105].

In addition to the Stokes measurements, the anti-Stokes signal was also observed when pumping with coupled powers >3 mW. Figure 4.5 shows the anti-Stokes spectra obtained with the pump wavelengths of 1431 nm and 1550 nm, respectively. The wavelength shifting of 15.6 THz was also observed for anti-Stokes wave, which is the same as Stokes wave but in the opposite directions. Due to the low anti-Sotkes power relative to the noise floor, the anti-Stokes spectrum exhibits an asymmetric profile. In theory, the power ratio between the anti-Stokes (P_{AS}) and Stokes (P_S) can be calculated

by quantum statistics as [92]:

$$\frac{P_{AS}}{P_S} = e^{-h\omega_v/k_B T}, \tag{4.7}$$

where ω_v is the phonon frequency, T is the experimental temperature in units of K, and k_B is the Boltzmann constant. The calculated power ratio (0.08) matches well with the experimental value of 0.09, which can be obtained by integrating the power spectra shown in Figure 4.5.

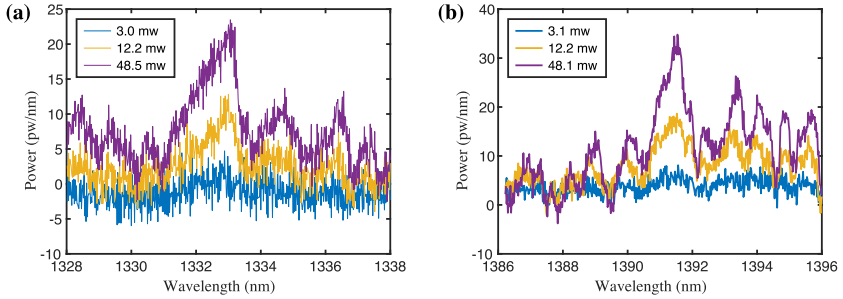

FIGURE 4.5: Anti-Stokes Raman emission for pump wavelength of (a) 1431 nm and (b) 1500 nm.

When characterising the spontaneous Raman emission in Fibre1, spectral measurements covering a wide wavelength range including different pump sources, Stokes and anti-Stokes waves were also recorded. Figure 4.6(a) shows the measured spectra when pumped with the 1431 nm laser, where the Stokes waves have a centre wavelength of 1546.6 nm and the anti-Stokes waves have a centre wavelength of 1332.8 nm. Figure 4.6(b) shows the measured spectra when pumped with the 1500 nm source. For this pump, the centre wavelength of the Stokes and anti-Stokes wave were shifted to 1626.4 nm and 1391.4 nm, respectively. When pumped with the same pump power level, the power of Stokes wave for these two pump wavelengths was similar, and the maximum measured Stokes power was -69.8 dBm and -70.4 dBm for the pump wavelengths of 1431 nm and 1500 nm, respectively. The similar Stokes powers indicate that the Raman emission efficiency of this telecom band system is stable when tuning the pump wavelengths.

To further test the tunability of this system, additional Raman emission spectra were measured by using a 1550 nm laser source. Figure 4.6(c) shows the record spectra, where the Stokes and anti-Stokes waves have a centre wavelength of 1685 nm and 1434.4 nm, respectively. As the Stokes wave was buried in the background noise of the telecom band OSA (AQ6370D), a low-noise mid-infrared OSA (AQ6375) was used to measure the spontaneous Raman emission when pumped at 1550 nm. As show in Figure 4.6(d), when pumped with a power of 48.2 mW, the Stokes wave has a power of -70.1 dBm , which is around the same power level as the Stokes wave when pumped at 1431 nm (-69.8 dBm) or 1500 nm (-70.4 dBm). The stable Raman emission efficiency when tuning the pump wavelength from 1431 nm to 1550 nm shows the benefit of using

this SCF-based Raman system for the wavelength generation and signal amplification in the telecom band.

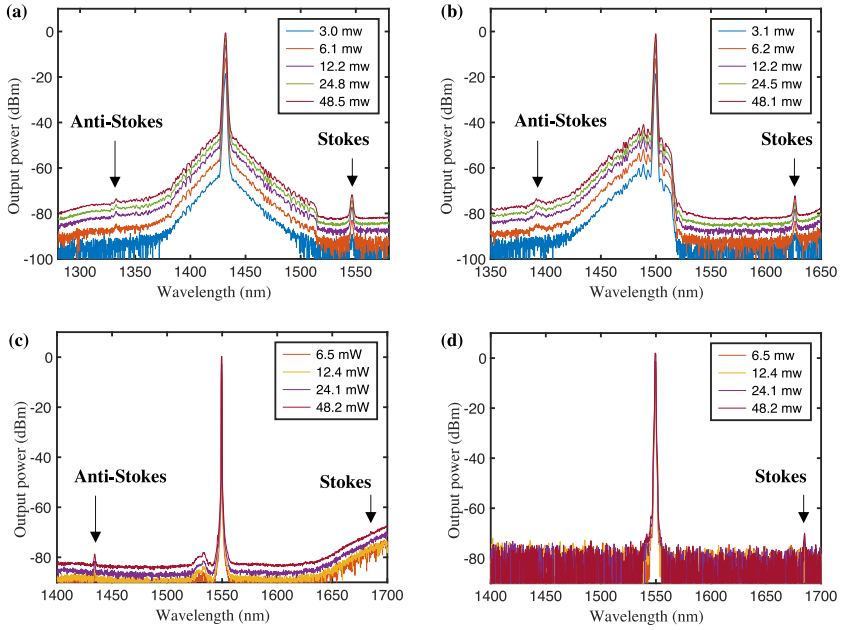

FIGURE 4.6: Spontaneous Raman spectra of tapered SCFs at pump wavelength of (a) 1431 nm, (b) 1500 nm and (c)&(d) 1550 nm. The spectra in (d) are the same as those in (c), but measured on a mid-infrared OSA.

4.4.4 Stimulated Raman amplification

The high Raman gain coefficient ($\sim$30 cm GW^{-1}) obtained by characterising the spontaneous Raman emission indicates that SCF is very suitable for stimulated Raman amplification in the telecom band. Due to the similar Raman gain coefficient for the two pump wavelengths, only the 1431 nm pump wavelength was investigated for the Raman amplification measurement. The setup is the same with the spontaneous measurement (shown in Figure 4.2), but a tunable signal laser (TUNICS T100S) was introduced as a seed signal. The signal wavelength was scanned from 1542 to 1550 nm with a fixed input power of 0.1 mW. The Raman gain was measured by comparing the Stokes

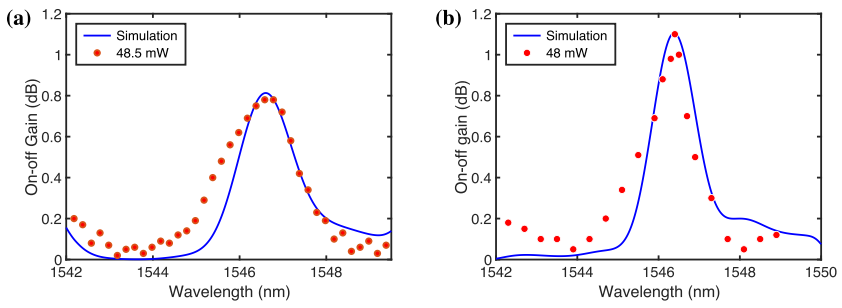

FIGURE 4.7: (a) Stimulated Raman gain for a 1431 nm pump for (a) Fibre1 (b) Fibre2.

TABLE 4.3: Simulation parameters for Fibre2 in stimulated Raman scattering.

Parameter	Symbol	Value (unit)
Pump wavelength	λ	1431 nm
Linear loss	α_l	1 dB cm^{-1}
Keff effect coefficient	n_2	4.2×10^{-18} m^2 W^{-1}
Carrier lifetime	τ	7.5 ns μm
FCA parameter	σ	1.45×10^{-21} m^2
TPA coefficient	β_{TPA}	11.77×10^{-12} m W^{-1}
Effective mode area	A_{eff}	0.3×10^{-12} m^2

power variation when the pump was on and off. Figure 4.7 shows the on–off gain curve with a pump power of ∼48 mW for Fibre1 and Fibre2. The peak gains were 0.8 dB in Figure 4.7(a) and 1.1 dB in Figure 4.7(b). The peak gain wavelengths for these two fibres were 1546.3 nm, which matches well with the spontaneous peak. The higher Raman gain for Fibre2 is mainly due to the lower linear loss (1 dB cm^{-1} vs 2 dB cm^{-1}) and longer waist length (1.5 cm vs 1 cm). Moreover, the measured maximum Raman gain (1.1 dB) obtained in Fibre2 is slightly larger than what has been reported (0.7 dB) for sub-micrometre-sized planar silicon waveguides in Ref. [105], which is attributed to the combination of low fibre transmission loss and longer waveguide lengths. Figure 4.7(a) and Figure 4.7(b) also plot the simulation results calculated by Shiyu Sun, which agree well with the measured experimental data. The simulation parameters for Fibre1 are the same as for the spontaneous simulation in Table 4.2 and the parameters for Fibre2 were summarised in Table 4.3.

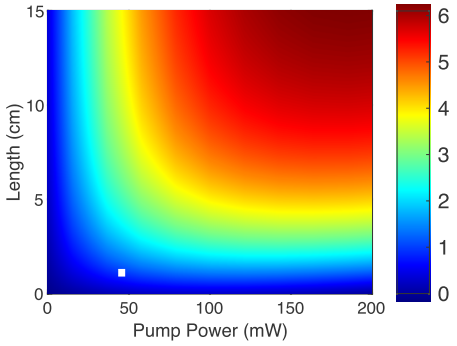

FIGURE 4.8: Simulation results of on–off gain as a function of coupled pump power and fibre length.

Althoug 1.1 dB on-off Raman gain is still not high enough for physical applications, it is only limited by the input pump power and fibre length. To better understand the performance of the telecom band Raman system, additional simulations were calculated for Fibre2. Figure 4.8 shows a colour map of the on-off gain as functions of the coupled pump power and fibre length, assuming that all other parameters (core size, transmission loss, etc.) remain the same as Fibre2. These results show that the maximum gain would increase slightly to 1.6 dB when the pump power is increased to ∼120 mW. However, due to the increasing nonlinear loss introduced by the TPA induced free

carriers, there is little benefit in increasing the pump power more than 120 mW. An alternative solution is increasing the fibre length to 10 cm, where the gain could reach as high as 6 dB.

4.5 Mid-infrared Raman process

Mid-infrared regime is of great interest for gas sensing [106], environmental monitoring [107], and medical diagnostics [108]. Within this regime, 2 μm wavelength has attracted considerable interest because it is the operating wavelength of thulium-doped fibre systems, which can produce flexible power scaling and high-quality beam profiles with minimal thermal distortion. As discussed in Chapter 2, the TPA coefficient (β_{TPA}) of silicon at 2 μm is only around half as strong as the value at 1.55 μm (0.3 cm GW^{-1} vs 0.7 cm GW^{-1}). Therefore, the high peak power pulsed laser can be used for SCF-based mid-infrared Raman systems to increase the Raman emission power. Another benefit of using pulsed laser is that the FCA can also be reduced by using laser sources with pulse durations much shorter than the lifetime of free-carriers [109]. Thus, this section focused on the 2 μm pulsed laser pumped Raman system.

4.5.1 Fibre design

TABLE 4.4: Parameters of the tapered SCF (Fibre3) used for mid-infrared Raman scattering measurement.

Parameter	Symbol	Value (unit)
Waist diameter	D_w	1.59 μm
Waist length	L_w	6 cm
Total length	L	6.5 cm
Input diameter	D_{in}	4.6 μm
Output diameter	D_{out}	4.4 μm
Propagation loss	α	0.2 dB cm^{-1}

As discussed in the telecom band Raman system, the Raman gain benefits a lot from longer fibre lengths. Therefore, the total fibre length for this work was designed to be 6.5 cm, including a waist length of 6 cm and two taper transitions with a length of 2.5 mm each. Although small core diameters can introduce high light intensities, it will also introduce higher transmission loss due to the increased absorption loss introduced by silica cladding at 2 μm. After testing the insertion loss of tapered SCFs with different core diameters, a waist diameter of 1.6 μm was selected to ensure low transmission loss for the longer wavelength of pump (2 μm) and Raman shifted signal (2.2 μm). Table 4.4 summarises the parameters of the tapered SCF used for 2 μm Raman amplification, which was named Fibre3. To characterise the propagation loss of the tapered SCF, the insertion loss of the device was measured with a 2 μm pulsed laser, using the lowest

power setting to minimise the effect of nonlinear absorption. The measured insertion loss for this SCF was 12.8 dB, including 10.7 dB coupling loss and 1.3 dB transmission loss, so that the estimated transmission loss is only 0.2 dB cm^{-1} for Fibre3, which is comparable to the lowest losses obtained in the SCF platform [48, 39].

4.5.2 Experimental setup

Figure 4.9 shows the experimental setup to investigate the 2 μm Raman measurement. A gain-switched laser diode ($\lambda = 1.99$ μm, Eblana Photonics) seeded thulium-doped fibre master oscillator power amplifier system was used as a pump laser source [110]. The pump had a 125 ps pulse duration with a repetition rate of 10 MHz. The maximum average output power is 70 mW, corresponding to a maximum peak power of ~56 W at the central wavelength of 1.99 μm. The signal used for Raman amplification was a CW mid-infrared laser (Cr^{+2}: ZnS/Se IPG Photonics) that can be tuned over a range of 2.0-2.4 μm, with a minimum wavelength resolution of 0.3 nm. A 90:10 fiberised beam combiner (BC) was used to combine the pump and signal before being injected into the tapered SCF. To couple the combined lasers into the SCF, a 40× objective lens (OL1, NA: 0.65) was used, and a 60× lens (OL2, NA: 0.85) was used to collect the output pump and Stokes wave. The beam profile was monitored by a camera to ensure the light was coupled into the fundamental mode. A mid-infrared patch cord (Thorlabs M42) was used to send the collected light to the detector. When used for spontaneous Raman scattering characterisation, the signal laser was turned off and the output light was sent to an mid-infrared OSA (AQ6375) to measure the Raman scattering spectra. For the characterisation of the mid-infrared SRS amplification, the CW signal was tuned across the measured spontaneous scattering bandwidth. An optical chopper was used to modulate the DC signal before coupling into the fiberised BC, and a lock-in amplifier (LIA) was used to detect the power variation of the output signal when the pump was on and off.

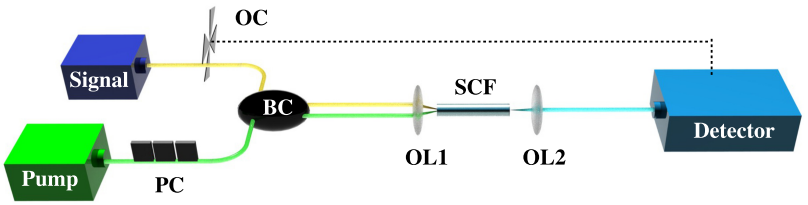

FIGURE 4.9: Experimental setup used for 2 μm Raman scattering measurements. OC: optical chopper, BC: beam combiner.

4.5.3 Spontaneous Raman scattering

Figure 4.10(a) shows the spontaneous Raman scattering spectra. The Stokes peak is positioned at ∼2.22 μm, matching with the expected Raman shift of 15.6 THz. Due to the narrow linewidth of the pump source (<0.05 nm), the linewidth of the Stokes wave (∼1.7 nm) is close to the intrinsic bandwidth (105 GHz) of the silicon Raman emission. Although the noise level of the OSA is higher in the mid-infrared, the appearance of the spontaneous Stokes wave for average powers was lower than that for telecom band (2 mW at 2 μm vs 3 mW at 1.55 μm) due to the lower transmission loss and longer fibre length. Figure 4.10(a) also plots the simulation results by solving Equation (2.47), which was done by Shiyu Sun. Table 4.5 summarises the parameters used for the simulations. The excellent agreement between the experiments and simulation data verifies the parameters used for the calculations.

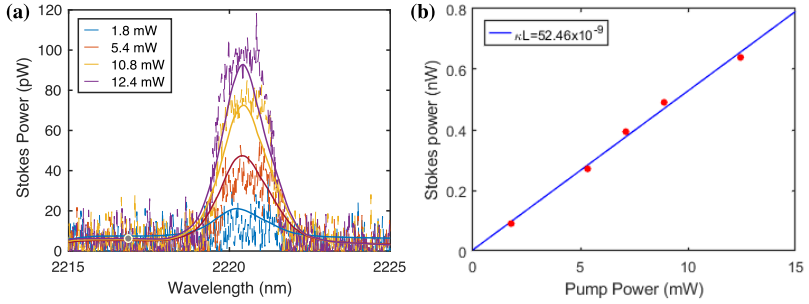

FIGURE 4.10: (a) Spontaneous Raman emission spectra at various time-averaged pump powers for a pump wavelength of 1.99 μm. (b) Stokes power as a function of coupled-in average pump power.

To compare the efficiency of the spontaneous Raman emission with the results obtained in the telecom band, the spontaneous Raman coefficient was also calculated using the relationship between the integrated Stokes power versus pump power. Figure 4.10(b) plots the generated Stokes power as a function of coupled-in average pump power. The spontaneous Raman coefficient at 2.2 μm can be determined as 8.7×10^{-9} cm^{-1} from the linear fit. Then the spontaneous Raman efficiency S can then be estimated to be $\sim1.05\times10^{-7}$ cm^{-1} Sr^{-1} by using Equation (4.5). Comparing this value with previous results for telecom band system, the lower S is in agreement with the λ^{-4} dependence. The value of the Raman gain coefficient (g_s) at 2 μm was also calculated via Equation (4.6), which is found to be 18 cm GW^{-1} at the pump wavelength of 1.99 μm. The value here is lower than the telecom band Raman in Ref.[95] but higher than the value obtained in Ref.[97], which was obtained in bulk silicon for the pump at 3.4 μm. Although g_s follows the expected trend of decreasing with a λ^{-1} dependency, the slightly lower g_s is expected to be compensated by the higher pump peak powers that can be used at 2 μm [88].

TABLE 4.5: Simulation parameters of Fibre3 for spontaneous Raman scattering.

Parameter (label)	Value (unit)	Parameter (label)	Value (unit)
Effective mode area (A_{eff})	1.17 μm^2	FCD (μ)	5.87
TPA coefficient (β_{TPA})	0.3 cm GW^{-1}	Phonon lifetime (τ_1)	7.5 ns
Free carrier loss (σ)	1.45×10^{-21} m^2	Input loss (α_{in})	7.5 dB
GVD (β_2)	0.003 ps^2 m^{-1}	Output loss (α_{out})	4 dB
Nonlinear index (n_2)	6×10^{-18} m^2 W^{-1}	Damping time (τ_2)	3.5 ps
TOD (β_4)	-7.23×10^{-7} ps^4 m^{-1}	Response function (f_R)	0.038

The backward spontaneous Raman emission in Fibre3 was also measured by introducing a fiberised beam combiner before the SCF. Due to the higher system losses in this configuration where the beam combiner (75: 25) is used to couple the pump (75%) into the SCF with a TLF and couple out the backward propagating Raman scattering signal with the other port (25%). The measured backward Raman power is lower than forward scattering by ∼4 dB. Although the backward Raman amplification is often favored in traditional systems as it can avoid residual pump power at the output, and it also lowers the noise properties, owing to the short length of the SCF used in our experiments (6.5 cm), the Raman gain and noise properties for our system are in fact similar for the forwards and backward pumped configurations. Therefore, only forward direction pumping is investigated for mid-infrared Raman amplification.

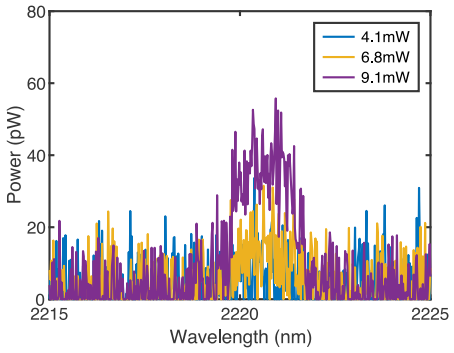

FIGURE 4.11: Backward spontaneous Raman emission spectrums at various time-averaged pump powers.

4.5.4 Stimulated Raman amplification

To demonstrate the capacity for efficient Raman amplification in this 2 μm wavelength region, the input CW signal power was fixed at 0.1 mW, which is consistant with the previous telecom band Raman amplification experiment. The 2 μm stimulated Raman gain could be easily observed for average pump powers as low as ∼3 mW. To measure the largest measurable gain, which is more useful for nonlinear applications, the highest pump power was used. The maximum coupled in pump power was fixed at 12.4 mW (corresponding to a peak power of 10 W), estimated by using the input coupling loss of 7.5 dB. Figure 4.12(a) shows the measured time-averaged on-off gain as

the signal wavelength is tuned across the Raman emission bandwidth. A maximum time-averaged gain of 3.7 dB was measured for the signal wavelength of 2.22 μm, with a measured average signal power of ~10 nW out of this system. Owing to the pulsed nature of the pump beam, the amplified signal will also occur as a train of short pulses [111]. By converting the time-averaged on-off gain using the duty cycle factor F [1/(10 MHz×125 ps)], the peak on-off gain is calculated to be ~30.4 dB, corresponding to a peak signal output of 0.3 mW. This gain is substantially larger than the 12 dB that was reported for amplification at 3.4 μm in bulk silicon, which is attributed to the higher pump intensity (900 MW cm^{-2} vs 217 MW cm^{-2}) and longer nonlinear interaction length (6.5 cm vs 2.5 cm) available via the fibre platform [97]. Compared with the Raman gain previously obtained in the telecom band system (1.1 dB), this gain is much larger due to the high pump power and long fibre length. The Raman gain obtained here is only slightly lower than the best results for conventional on-chip waveguides for a pump power more than five times larger, where 6.8 dB of measured gain (corresponding to 45.8 dB peak on-off gain) was obtained for a 6.6 ps pump pulse with a peak-coupled pump power of 55 W. Figure 4.12(b) then shows the tuning of the output signal through tuning the pump wavelength across a bandwidth of 4 nm, illustrating that the gain bandwidth could be increased by using a broadband source, or even several pump sources combined to yield a flat gain profile. The variation of output signal power during the wavelength tuning was mainly caused by the loss wavelength dependence of the system.

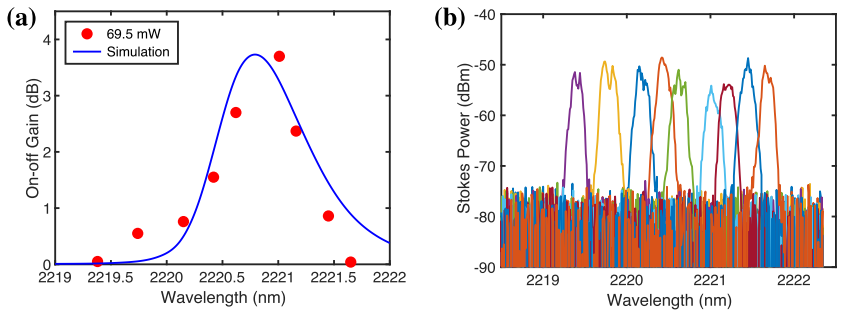

FIGURE 4.12: (a) Stimulated Raman gain for a 1.99 μm pulse pump with 12.4 mW of coupled power. (b) The measured output spectra when tuning the pump wavelength.

To further probe the Raman amplification performance within the current system, additional simulations were conducted to investigate the role of the pump power and the fibre length. Figure 4.13 plots the predicted time-averaged on-off gain, assuming that the remaining SCF and pulse parameters are the same as the experimental procedure herein. The maximum measured gain obtained in Figure 4.12(a) is also labelled on the colourmap. Due to the non-negligible TPA parameter at the 1.99 μm pump wavelength, these results show that there is little benefit in increasing the pump power much beyond the existing value due to the substantial FCA associated with the relatively long 125 ps pump pulse. However, increasing the SCF length to 20 cm while retaining the same pump power, does result in a substantial increase in the time-averaged on-off

gain up to ∼20 dB (corresponding to a peak on-off gain of 49 dB), which would result in an average signal powers as high as 1 μW (peak power of 0.8 mW). Thus, this analysis highlights the importance of optimising the system to minimise the role of nonlinear absorption processes to obtain high gains, and thus high signal output powers.

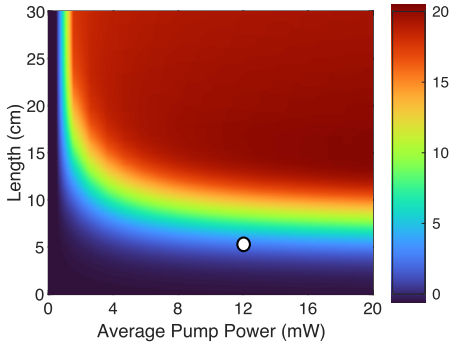

FIGURE 4.13: Simulation results of on-off average gain as a function of coupled pump power and waist length of SCF.

4.6 Cascaded Raman scattering

4.6.1 Optimisation of Raman system

As the high peak on-off Raman gain can be obtained with 2 μm pulsed laser pump, additional simulations were conducted to investigate the conditions for efficient cascaded Raman scattering. As discussed in chapter 2, the FWM could be strong when the pump wavelength colse to the ZDW ($\beta_2 = 0$) [112]. Figure 4.14 plots the calculated GVD (β_2) profiles in the SCFs with different core diameters. For the fiber core size (D = 1.6 μm) used in the 2 μm Raman amplification experiment, the pump wavelength is very close to the ZDW. To ensure that Raman scattering was the dominant nonlinear conversion process, the ZDW should be shifted by varying the core diameter.

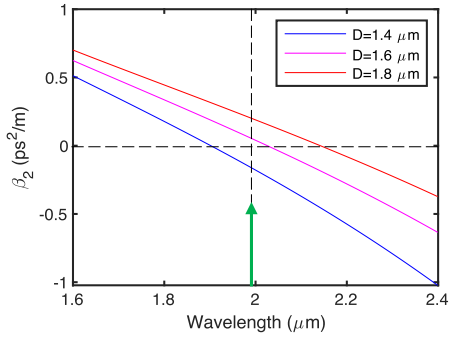

FIGURE 4.14: Calculated GVD (β_2) for the SCF with different core diameters shown in the legend.

By using the parameters from Table 4.5 and the calculated values of the dispersion for SCFs with different core diameter, Figure 4.15(a) shows the output peak power of Stokes waves as a function of fiber core diameter. The Stokes waves are generated via spontaneous cascaded Raman scattering, assuming the peak power of the pump is 10 W, and the pulse duration is 125 ps, as used in the 2 μm Raman experiments. The cascaded Raman scattering reaches a minimum for a core diameter of 1.58 μm. This is attributed to the strong competition with the FWM process, which overlaps with the Raman bandwidth [2]. However, when increasing the core diameter to 1.7 μm, which positions the pump further from the ZDW, even the 5th order Stokes wave (4.1 μm) can achieve maximum output power. Although increasing the core diameter further, allows for the observation of the 6th order Stokes wave (>5.5 μm), the converted powers for all the other waves are significantly reduced. Therefore, 1.7 μm was chosen for long wavelength generation through cascaded Raman processes in the additional simulations.

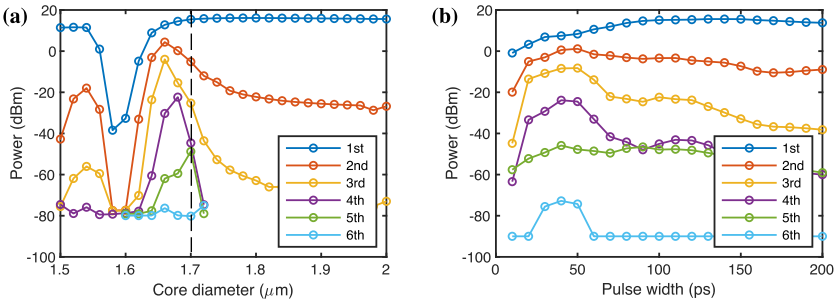

FIGURE 4.15: Cascaded Raman scattering output Stokes power as a function of (a) fiber core diameter and (b) pulse width.

Moreover, the role of nonlinear absorption, and specifically the build-up of free carriers associated with the long pulse duration was also investigated. When pumping at 2 μm with a fixed peak power of 10 W, Figure 4.15(b) shows the output Stokes peak powers from cascaded Raman scattering as a function of pump pulse width for a 1.7 μm core diameter fiber. As we can see, the high-order Stokes waves (2nd, 3rd, 4th, 5th) achieve a maximum output power when decreasing the pulse width to 40 ps. Therefore, a pulse width of 40 ps pulse width was selected for simulations of cascaded Raman scattering for the 2 μm pump.

4.6.2 Extended mid-infrared source generation

By using these new values of the waist diameter and pulse duration, Figure 4.16(a) shows the spontaneous Stokes power generated as a function of wavelength and fiber length assuming a coupled-in average pump power of 8 mW (peak-power of 20 W). Although the average power is slightly lower than the maximum value used in the

experiments, the peak power is twice as high owing to the shorter pulse duration. Figure 4.16(b) shows the output spontaneous Stokes powers as a function of fiber length. As can be seen in Figure 4.16(b), at a propagation distance of 2.5 cm, the first-order Stokes wave has intensified to have a similar power level with the pump, which enables it to act as a pump for the second-order Stokes wave at 2.5 μm . The second-order Stokes wave then grows to have a maximum power at the propagation distance of 4.5 cm and acts as a pump for the third-order Stokes wave. Moreover, as the fiber length increases further, Raman Stokes waves out to the 5th order can be generated ($\lambda \sim 4.1$ μm) with a high peak power level (>0.3 mW). The maximum output peak powers for the Stokes wave from 1st order to 5th order are 7.1 mW, 6.9 mW, 0.35 mW, 1.27 mW and 0.34 mW, corresponding to output average powers of 3.18 μW, 2.76 μW, 0.14 μW, 0.51 μW and 0.14 μW, respectively. As the simulation here includes all the nonlinear processes (FWM, TPA, FCA, SRS and IRS), the 3rd-order Stokes wave could have a lower power due to the IRS process which causes energy not to transfer in one direction [113].

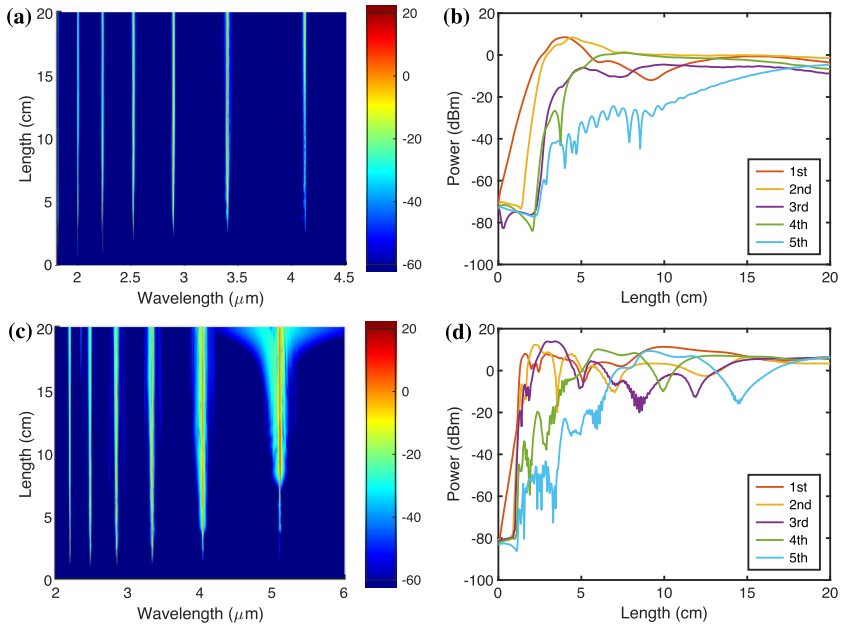

FIGURE 4.16: (a) Simulated spectral evolution of cascaded Raman scattering with 2 μm pulsed laser pump, (b) output peak powers of Stokes waves as a function of fiber length for (a). (c) Simulated spectral evolution with 2.2 μm pulsed laser pump, (d) output Stokes peak powers as a function of fiber length for (c).

To increase the Raman powers and extend the wavelength coverage further, it is also worth exploring the benefits of switching to a slightly longer pump wavelength, such as could be offered by a holmium-doped fiber system operating at 2.2 μm [114]. Interestingly, 2.2 μm represents a favorable wavelength for pumping nonlinear processes in silicon as it is at the edge of the TPA region, so that β_{TPA} is negligible. This wavelength also is shorter than where higher-order 3PA processes become significant. Thus, one can expect the nonlinear absorption to play a minimal role for such pump sources and

the original pump pulse duration of 125 ps can be used to increase the energy in the generated Stokes waves. Figure 4.16(c) plots the spontaneous Stokes power as a function of wavelength for a 2.2 μm pump, assuming the same fiber length and coupled input peak power (20 W) as in Figure 4.16(a), clearly showing the strongly cascaded conversion. The output peak powers of the generated Stokes waves as a function of fiber length are then plotted Figure 4.16(d). Due to the significant reduction in TPA and FCA for this wavelength, a substantial increase in the conversion efficiency is observed, with the 2nd order Stokes wave (now at a wavelength of $\sim$2.8 μm) appearing after only 2 cm of propagation. Moreover, as the 2nd order Stokes power increases, the process can continue to rapidly generate higher order Stokes waves (up to the 5th order at $\lambda \sim 5.1$ μm) for fiber lengths of only $\sim$5 cm. Moreover, the Raman wavelength conversions essentially all happen within the first 10 cm, so that there is little benefit to extending the SCF length for 2.2 μm system beyond this. Thanks to the negligible nonlinear absorption and increased pump pulse energy for the 2.2 μm system, the obtainable maximum peak powers of all Raman Stokes waves now exceed 8.67 mW, corresponding to an average power of 10.8 μW, which is two orders of magnitude higher than 2 μm system. Further, these powers could be increased by an order of magnitude with increasing input pump powers [115]. Thus, these results show the potential to extend the wavelength coverage of the SCF-based Raman system across the 2-5 μm wavelength region, and beyond [116].

4.7 Conclusion

In this chapter, spontaneous and stimulated Raman scattering has been investigated in tapered SCFs. The Raman gain coefficient of the fibres was estimated to be $g_s \sim$30 cm GW^{-1} in the telecom band and a peak on-off gain of 1.1 dB was obtained using a milliwatt level CW pump power at 1.43 μm. Moreover, when shifting the pump wavelength to 2 μm, a 30.4 dB peak on-off gain was achieved by extending the fibre length from 1.5 cm to 6 cm and pumping with a pulsed laser (125 ps) to increase the coupled peak power. Then the additional simulations show the possibility to increase the peak on-off gain up to $\sim$50 dB by extending the fibre length to 20 cm. Finally, modelling of the nonlinear propagation suggested that the performance of mid-infrared Raman system can be optimised by altering the SCF core diameter for pump wavelength beyond 2 μm and shown the possibility to extend the generated signals to wavelengths of $\sim$4 μm for a 2 μm pump source by using cascaded Raman processes, and even further to $\sim$5 μm when using a source of wavelength longer than 2.2 μm.

Chapter 5

Four-wave mixing wavelength conversion

5.1 Introduction

In this chapter, FWM in the tapered SCFs is studied. Firstly, the wavelength conversion based on FWM is investigated with simulations and experiments in the telecom band. Both the conversion efficiency and bandwidth are discussed, then the role of fibre dispersion and fibre length for FWM in the SCFs is also analysed. Secondly, the Raman scattering process is used to enhance the FWM conversion efficiency by setting the newly generated wave within the Raman amplification bandwidth. The enhancement introduced by the Raman process is analysed by both simulation and experiments.

5.2 Four-wave mixing

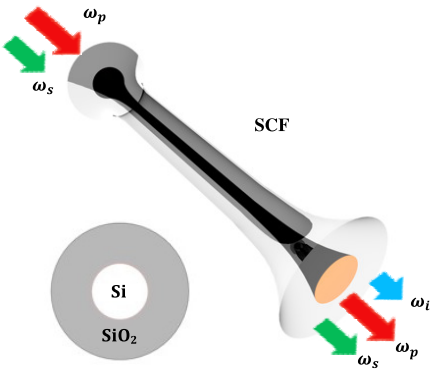

FIGURE 5.1: Schematic of degenerate FWM in tapered SCF platform.

Similar to the Raman scattering process, FWM also arises due to the third-order nonlinearity ($\chi^{(3)}$) in the SCFs and can be either a spontaneous or stimulated process. However, only stimulated FWM is studied in this thesis because the photon power generated by spontaneous FWM processes is too low and the access to high sensitive photon detectors was limited when this work was going on. Figure 5.1 shows a schematic of degenerate FWM in the tapered SCF platform. The stimulated FWM involves four photons, including two pump photons, one signal photon and one idler photon. The frequency of the two pump photons can be either same or different, corresponding to the degenerate and nondegenerate FWM, respectively. As it is more convenient to achieve phase matching condition, this thesis is focused on the degenerate FWM. To achieve high wavelength conversion efficiency, both energy and momentum need to be conserved. The conservation of energy is automatically satisfied in the degenerate FWM process due to the frequency relationship between pump, signal and idler photons as:

$$2\omega_p = \omega_s + \omega_i. \tag{5.1}$$

As discussed in chapter 2, the momentum conservation can be achieved when the phase mismatch is almost vanished ($\Delta k \approx 0$). To characterise the FWM efficiency, the conversion efficiency (CE) is defined by using the output power of the idler wave (P_i^{out}) and the input power of the signal wave (P_s^{in}) as [84]:

$$CE = \frac{P_i^{out}}{P_s^{in}}. \tag{5.2}$$

Assuming the pump is not depleted during the process, the CE of FWM can be calculated as [2]:

$$CE = [\frac{\gamma P_p}{g} \sinh(gL_{eff})]^2, \tag{5.3}$$

where the parametric gain coefficient g is given by [117]:

$$g = \sqrt{\gamma P_p \Delta k_L - (\Delta k_L)^2}, \tag{5.4}$$

where P_p is the pump power. It is clear that the maximum CE occurs when $\Delta k = 0$, which usually can be satisfied around the ZDW. The maximum CE is given as:

$$CE_{max} = \sinh^2(\gamma P_p L). \tag{5.5}$$

5.2.1 Dispersion and phase matching in SCFs

To study the FWM in the telecom band, Figure 5.2(a) shows the GVD (β_2) for the SCFs with different core diameters by using the calculated effective refractive index from Equation (2.12). As 1.55 μm is the most commonly used wavelength in the telecom band, three core diameters (0.8 μm, 0.9 μm and 1 μm) with ZDWs close to 1.55 μm were

used for the calculation. As shown in Figure 5.2(a), the ZDW is very sensitive to the core diameter variation and increases as the fibre core diameter increases. The GVD value can be positive or negative by setting the pump wavelength shorter or longer than the ZDW, corresponding to the normal dispersion region ($\beta_2 > 0$) or anomalous dispersion region ($\beta_2 < 0$). Moreover, as the fourth-order dispersion (FOD, β_4) is also very important for the phase matching, Figure 5.2(b) shows the calculated FOD for these core diameters, which all have negative values and so can be used to compensate for the positive nonlinear refractive index variation ($\Delta k_{NL} = 2\gamma P$) in the phase mismatch form ($\Delta k = \Delta k_L + \Delta k_{NL}$).

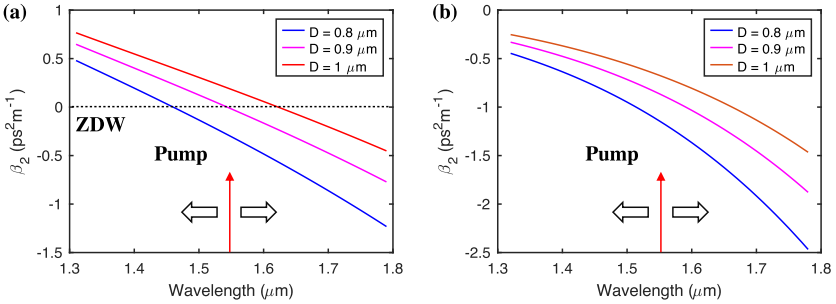

FIGURE 5.2: Calculated (a) GVD (β_2) and (b) FOD (β_4) for SCFs with different core diameters.

As the ZDW of 0.9 μm core diameter SCFs is most close to 1.55 μm, it was used for the additional simulations to calculate the CE of FWM. To investigate the CE under different fibre dispersion, the pump wavelength was slightly tuned around 1.55 μm to change the dispersion. Table 5.1 summarises the calculated values of GVD and FOD for the different pump wavelengths. To minimise the influence of nonlinear absorption, a low pump power of 50 mW was used for the modelling. Moreover, the fibre length is also involved in the modelling because it can influence the CE of FWM, particularly if the phase matching is not perfect. Figure 5.3 shows the calculated CE as a function of signal wavelength and fibre length. The maximum CE is similar (∼-30 dB) for all the pump wavelengths while the FWM bandwidth varies a lot as the fibre dispersion changes. As shown in Figure 5.3(a), the largest bandwidth of 650 nm (from 1.9 μm to 1.25 μm) was achieved when pumped at 1.53 μm, which is in the normal dispersion region. Figure 5.3(b) also shows the FWM pumped in the normal dispersion region. However, as the value of GVD for 1.54 μm pump is smaller than that of 1.53 μm pump,

TABLE 5.1: Fibre dispersion for a SCF with a core diameter of 0.9 μm when pumped at different wavelengths.

λ_p (μm)	GVD (ps^2 m^{-1})	FOD (10^{-5} ps^4 m^{-1})	A_{eff} (μm^2)	γ (W^{-1} m^{-1})
1.53	0.04	-0.8	0.387	57.91
1.54	0.01	-0.83	0.392	57.91
1.55	-0.02	-0.86	0.398	57.91
1.56	-0.04	-0.9	0.403	57.91

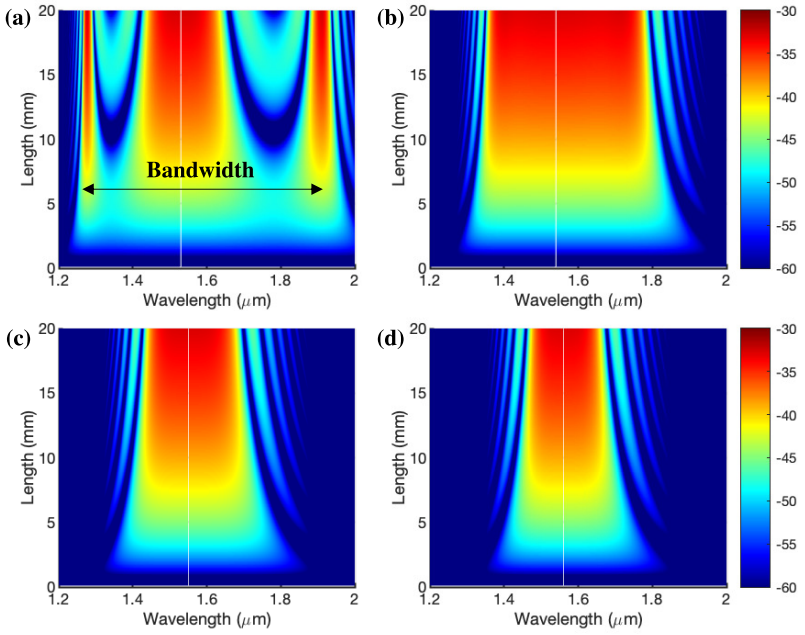

FIGURE 5.3: FWM efficiency as a function of SCF length and signal wavelength for a SCF with a core diameter of 0.9 μm when pumped at (a)1.53 μm, (b)1.54 μm, (c)1.55 μm and (d)1.56 μm.

the FWM bandwidth was slightly narrower, which is 550 nm (from 1.85 μm to 1.3 μm). Figure 5.3(c) shows the situations when pumped in the anomalous dispersion region. The FWM bandwidth was only 400 nm because both the β_2 and β_4 are negative and the phase mismatching increases very quickly when the signal wavelength is tuned away from the pump. Due to the more negative β_2 and β_4, Figure 5.3(d) shows the narrowest bandwidth (300 nm). Therefore, to achieve broden wavelength conversion bandwidth, the pump wavelength should be set to the normal dispersion region.

Moreover, the simulation in Figure 5.3 also shows the influence of fibre length. Longer fibre lengths tend to achieve higher CE due to the longer interaction lengths. However, the FWM bandwidth can be decreased when the fibre length increases due to the negative role of fibre length, which can be clear seen in the CE calculation Equation (5.3). Due to the trade-off between FWM bandwidth and CE, the fibre length should be designed according the requirement of nonlinear applications.

5.2.2 FWM characterisation in SCFs

To investigate FWM in the SCFs experimentally, two SCFs with similar lengths but different core diameters were selected for full characterisation. Table 5.2 summarises the fibre profiles and loss measurement results for the two tapered SCFs. Figure 5.4 shows the experimental setup used to characterise the FWM in SCFs. Two telecom band CW lasers were used as the pump and signal, respectively. A 50:50 fiberised BS was used

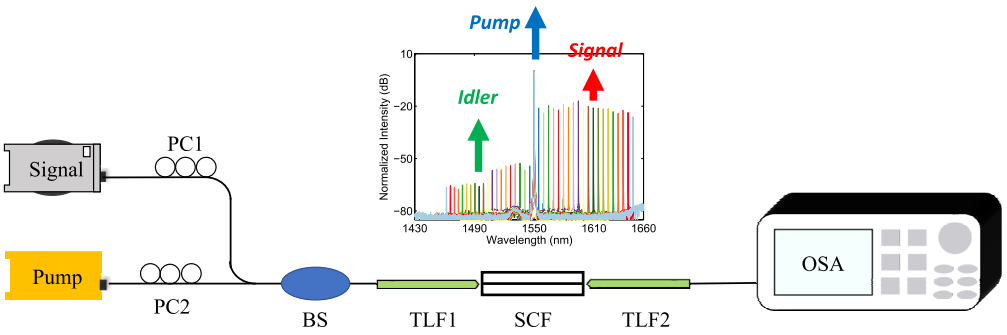

FIGURE 5.4: Schematic of the FWM characterisation setup. BS: beam splitter.

to combine the pump and signal lasers. TLFs were used to launch the light into the SCFs and collect the output light. Two PCs were used to align the polarisation of the two beams to achieve the maximum CE. A telecom band OSA was used to record the output FWM spectra. To testing the experiment setup, the inset in Figure 5.4 shows a recorded spectrum of FWM in Fibre4. The coupled-in pump power was fixed around 20 mW when the signal wavelength was tuned from 1555 to 1680 nm. The measured pump peak powers in the spectra were similar for all the measurements, which indicates that the whole system was very robust during the experiments. The CE can be calculated using the measured signal power and the corresponding idler powers.

TABLE 5.2: Fibre parameters for tapered SCFs used for FWM characterisation.

Label	D_w (nm)	ZDW (μm)	L_w (mm)	Insertion loss (dB)
Fibre4	780 nm	1.44	5 mm	7.6 dB
Fibre5	830 nm	1.48	5 mm	8.6 dB

Figure 5.5 shows the measured CE curves for Fibre4 and Fibre5 at three different pump wavelengths (1.54 μm, 1.55 μm and 1.56 μm), together with the calculated CE curves by using Equation (5.3). Thanks to the low transmission loss (<1 dB cm^{-1}) and good dispersion profile of tapered SCFs, broadband wavelength conversion of more than 280 nm has been demonstrated in the telecom band. The achievable maximum wavelength conversion was limited by the tuning range of laser sources but not the tapered SCFs. The simulation results match well with the experimental results, indicating that the estimated core diameter is very close to the real value. As the ZDW of Fibre5 is more close to the pump wavelengths, the main bandwidths of Fibre5 are slightly larger than Fibre4 when pumped at the same wavelength. Moreover, by comparing the CE curve when pumped with different wavelength for the same tapered SCF, it can be observed that the main bandwidth of FWM can be slightly larger when the pump wavelength is more close to the ZDW, which agrees well with the previous simulation. Table 5.3 summarises all the parameters used for the FWM simulation and the measured FWM bandwidth. Both Fibre4 and Fibre5 were pumped at anomalous dispersion region because the core diameters of these tapered SCFs are smaller than designed. As the dispersion variation introduced by changing the pump wavelength is very small, so that

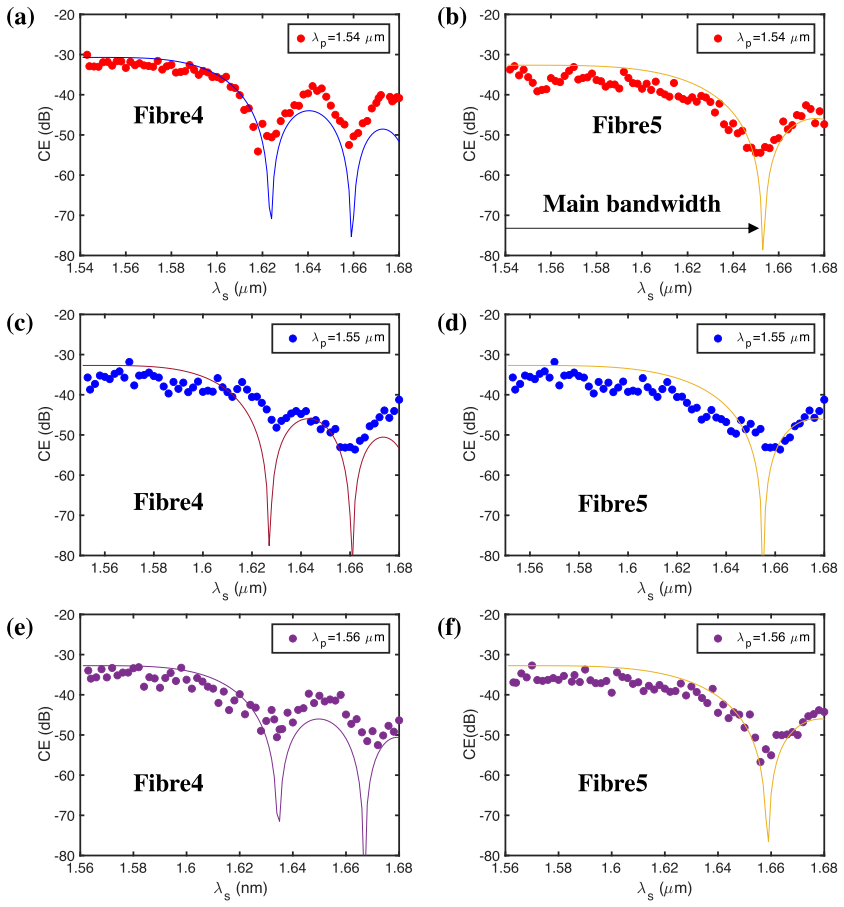

FIGURE 5.5: Measured CE curve of FWM for Fibre4 and Fibre5 at pump wavelength of (a)&(b) 1.54 μm, (c)&(d) 1.55 μm, (e)&(f) 1.56 μm.

the main bandwidth variation for different pump wavelengths is not very distinct. The maximum CEs achieved in the experiment is better than the previous simulation for tapered SCFs with a core diameter of 0.9 μm in the fibre length of 5 mm (-30 dB vs -37 dB) because the smaller fibre core diameter can increase the pump intensity to enhance nonlinear interaction. The minimum CEs in the experiment are not match perfect with the simulation value because the signal tuning resolution (2 nm) is not sufficient to align very accurately with the wavelength where the lowest FWM efficiency exist.

TABLE 5.3: Simulation parameters of fibres used for the FWM experiments.

Fibre name	λ_p (μm)	β_2 (ps^2/m)	β_4 (1×10^{-4} ps^4/m)	P (mW)	Main bandwidth (nm)
Fibre4	1.54	-0.3404	-0.1170	40	160
Fibre4	1.55	-0.3772	-0.1214	40	165
Fibre4	1.56	-0.4142	-0.1259	40	170
Fibre5	1.54	-0.1743	-0.2074	40	220
Fibre5	1.55	-0.2074	-0.1047	40	214
Fibre5	1.56	-0.2407	-0.1087	40	200

5.3 Raman enhanced FWM

5.3.1 Mechanism of Raman enhancement

As the wavelength conversion range of telecom band FWM is large enough to cover the Raman scattering bandwidth, it is necessary to study the interaction between these two nonlinear processes. In particular, because the FWM efficiency drops quickly when the signal is tuned far away from the pump wavelength, it can be useful to enhance the FWM efficiency with Raman scattering. In this work, the enhancement mechanism is achieved by setting the signal wavelength at the anti-Stokes wavelength so that the idler is at the Stokes wavelength. Thus stimulated SRS can be used to amplify the idler power. There are three dominant nonlinear processes, including FWM, SRS and IRS. Figure 5.6(a) shows the energy diagram of these three processes. FWM induces idler photons (λ_i) in the longer wavelength, and the SRS can amplify it to generate more idler photons because the idler wavelength is in the Raman gain bandwidth. Due to the strong signal power in the anti-Stokes wavelength, IRS can transfer the energy from signal to pump to compensate the pump photon depletion introduced by other two processes. As a result, more longer wavelength idler photons can be generated through the hybrid interaction.

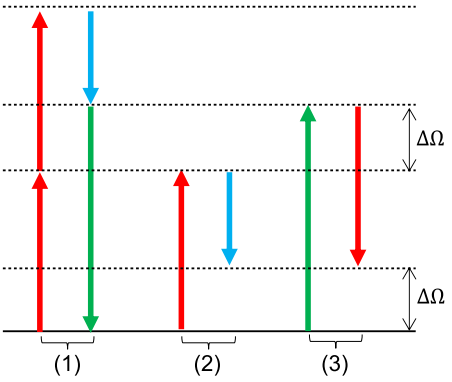

FIGURE 5.6: (a) Virtual energy level diagrams for (1) FWM, (2) SRS, and (3) IRS.

5.3.2 Experiment setup

Figure 5.7 shows the experimental setup used for the Raman enhanced FWM measurement. A tunable CW pump laser with a working wavelength around 1.55 μm was used as pump source for FWM. Due to the limited access to the tunable laser at the anti-Stokes wavelength of 1.43 μm when pumped around 1.55 μm, an alternative method was used. As shown in the inset, the signal wavelength was fixed at 1.43 μm and the pump wavelength was tuned to change the wavelength mismatch between the idler wavelength (λ_i) and peak Raman amplification wavelength (Λ_R). A WDM was used to

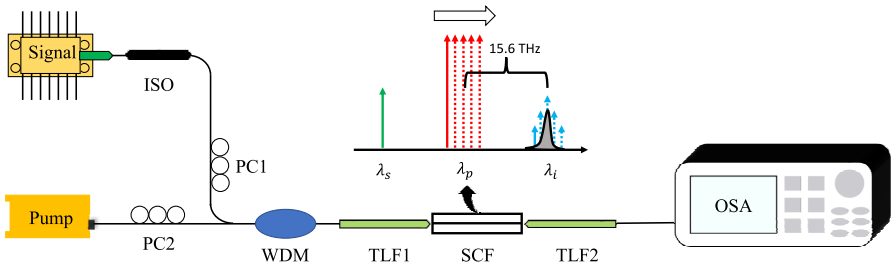

FIGURE 5.7: The experimental setup for Raman enhanced FWM measurement in the tapered SCFs.

combine the pump and signal beam and then coupled into and out the SCF using TLFs. Two PCs were used to align the polarization of the pump and signal to optimise the conversion efficiency. An OSA was used to record the output signals. The maximum enhancement will take place when the pump is tuned to align the idler wavelength with the peak Raman gain wavelength.

5.3.3 Fibre design

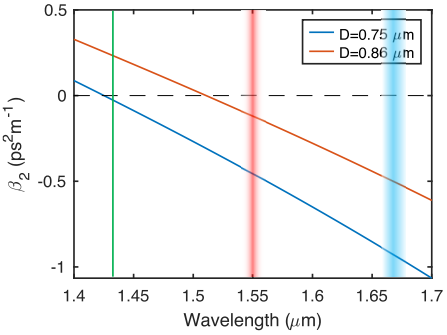

FIGURE 5.8: GVD (β_2) as a function of wavelength for SCFs with two different core diameters, as labelled. Vertical lines indicate the positions of the pump (middle), signal (left), and idler (right).

As discussed in Section 5.2.1, the fibre dispersion profile and length are very important for the efficiency of FWM. Therefore, tapered SCFs with different core diameters and lengths were fabricated for the Raman enhanced FWM investigation. Table 5.4 summarises the parameters of these fibres and Figure 5.8 shows the GVD (β_2) curves for the core diameters used. The position of the signal wavelength (1431 nm, green), tunable pump (∼1545 nm, red) and generated idler (∼1680 nm, blue) are labelled with vertical lines. The ZDW for the core diameter of 860 nm is much closer to the pump wavelength than the 750 nm core size to ensure a very different phase matching condition for comparison. To enhance the FWM wavelength conversion process, the fibre waist lengths were increased to more than 10 mm, which is two times longer than the fibres used in the FWM characterisation experiment. The insertion loss measurements for these three fibres show the transmission losses are less than 1 dB cm^{-1} in the telecom band.

TABLE 5.4: Geometrical parameters and insertion loss for the fibres used for Raman enhanced FWM measurement.

Fibre	D_w (nm)	L_w (mm)	Total length (mm)	Insertion loss (dB)
Fibre6	860 nm	10 mm	14 mm	8.4 dB
Fibre7	860 nm	15 mm	18.7 mm	9.8 dB
Fibre8	750 nm	10 mm	13.8 mm	7.8 dB

5.3.4 Characterisation of Raman enhanced FWM

Figure 5.9(a) shows the measured CE curves for the Raman enhanced FWM for different core diameters. The input pump powers were fixed at 28 mW and the signal power remained fixed at 2 mW. The curve for the SCF with a waist diameter (D_w) of 860 nm shows a clear peak when the offset ($\lambda_i - \Lambda_R$) is zero. A maximum CE up to ∼-44 dB is achieved with the Raman enhancement. However, the curve for the SCF with a waist diameter (D_w) of 750 nm does not have such a clear peak when tuning the offset. By comparing the results obtained for two different core diameters, it is clear that the maximum conversion efficiency drops as the FWM moves further away from phase matching. The results were compared with simulations (solid curve), which were conducted by Shiyu Sun. The simulation results are in good agreement with the experiments. To better understand the observed enhancement, the CE curves without the Raman process included were also calculated and shown as dash curves in Figure 5.9(a). A significant enhancement of ∼15 dB was achieved by comparing the experimental results with simulations for the 860 nm core diameter SCF, while the Raman enhancement for the 750 nm diameter SCF was only ∼9 dB due to the poor phase matching condition.

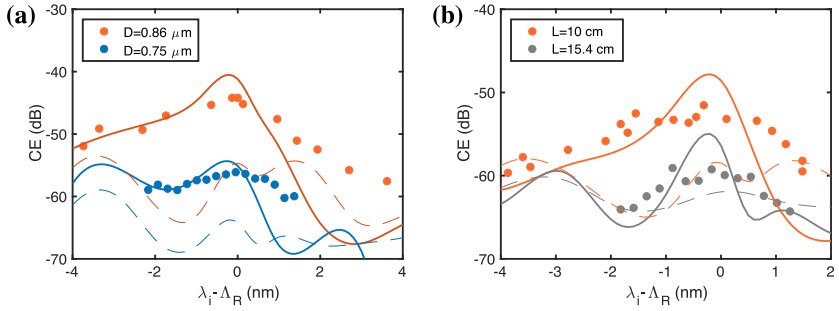

FIGURE 5.9: (a) CE curves as λ_i is tuned across Λ_R for SCFs with different core diameters and same length (L_w = 10 mm). (b) CE curves for SCFs with different lengths but same core diameter (D_w = 860 nm). Dashed curve is the CE without Raman process involved.

Moreover, to study the role of fibre length in the Raman enhancement, Figure 5.9(b) shows the CE curves for SCFs with a core waist diameter of 860 nm but different waist lengths (10 mm vs 15.4 mm). The pump power was reduced slightly to 14 mW to make the measurement process more stable to access more accurate results. The Raman enhancements obtained for the 10 mm and 15.4 mm long SCFs were 7 dB and 4

dB, respectively. To understand the role of fibre length in Raman enhanced FWM, additional simulations were done by Shiyu Sun. Figure 5.10 shows the CE as a function of fibre length. It is clear that there is an oscillation for the Raman enhanced FWM CE curve, so that the enhancement for 15.4 mm fibre is lower than the 10 mm fibre. The oscillation in Figure 5.10 is due to the imperfect phase matching ($\Delta k \neq 0$) for SCFs with a core diameter of 860 nm and the energy transfer between the pump photons and generated photon pairs. Importantly, the Raman enhancement only serves to amplify the conversion rather than alter this trend so that the best phase matching condition and SCF length should be chosen to achieve the maximum enhancement.

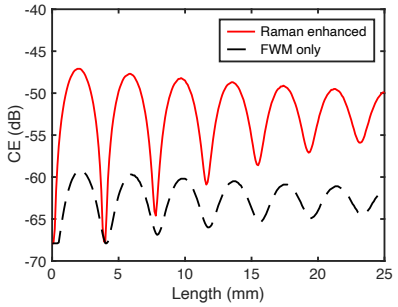

FIGURE 5.10: Simulated CE curves as a function of tapered waist length conducted both with (solid) and without Raman (dashed).

Compared with planar silicon waveguides, the maximum Raman-enhanced CE achieved in tapered SCF is much higher than that achieved in a rib waveguide (-44 dB vs -50 dB) despite the use of lower pump powers (28 mW vs 700 mW) [118]. The CE is only lower than the best results (exceeding 0 dB for a pump power of 20 mW) for their planar counterparts with ring-resonator geometries [119]. However, the simulation results in Ref. [120] show that the CE can be increased to 2.3 dB by increasing the pump peak power to 340 mW for a tapered SCF with a waist diameter of 860 nm over a length of 10 cm without the need for complex p-i-n diode [121] or ring resonator structures [119], highlighting the versatile of SCF platform.

5.4 Conclusion

In this chapter, FWM in the SCFs has been investigated in the telecom band. Firstly, the role of fibre dispersion and length in the FWM process was discussed using simulations, and experiments were used to study the FWM efficiency and bandwidth. A large FWM bandwidth (>280 nm) and a high CE (>-30 dB) was achieved experimentally with a fibre length of only 5 mm. Moreover, Raman scattering has been used to enhance the FWM CE by positioning the conversion wavelengths within the Raman amplification bandwidth. The role of phase matching in Raman enhanced FWM was

discussed. A Raman enhancement of more than 15 dB can be observed in the experiments, dependent on the phase matching condition.

Chapter 6

FWM for undetected-photon imaging

6.1 Introduction

In this chapter, undetected-photon (UP) imaging via FWM in SCFs is discussed. Firstly, the concept of UP imaging is introduced and two UP beam generation methods for imaging are compared. Secondly, the FWM-based classical UP imaging setup is presented and compared with previous setups, and the SCFs used for photon beams generation are characterised. Thirdly, amplitude imaging and phase imaging are realised by measuring the combined power variation and the interference fringes. Finally, the methods to expand the FWM bandwidth using SCFs for ultra-broadband UP imaging are discussed with simulations.

6.2 Undetected-photon imaging

6.2.1 Development of undetected-photon imaging

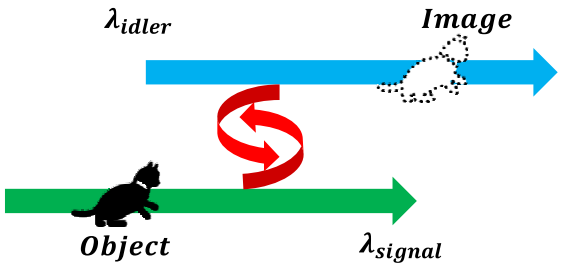

FIGURE 6.1: Operational principle of undetected-photon imaging.

A schematic of UP imaging is shown in Figure 6.1. A pair of UP beams is used for the imaging process, in which one photon beam (λ_{signal}) interacts with the object whilst the other beam (λ_{idler}) is detected. A key feature of this approach is that the wavelength used for illumination can be significantly different from that used for detection so that detectors can be used for imaging objects that are beyond the working wavelength range [122, 123, 124, 125]. Lemos *et al.* achieves the initial demonstration with a quantum imaging system in 2014 [126], where a 532 nm laser was used as pump to generate signal beam at 1550 nm and idler beam at 810 nm via spontaneous parametric-down conversion (PDC). The amplitude and phase images of an etched silicon plate were demonstrated by detecting light at 810 nm, which is out of the transmission window of silicon. However, due to the low photon generation rate of the quantum sources, highly sensitive single-photon detectors are needed for the quantum system. Following the initial demonstrations, Shapiro *et al.* argued that the use of non-classical light was not necessary to achieve the same result [127]. With that insight, classical analogues of UP imaging were explored by using correlated beams. The benefit of classical sources is that higher photon beam powers and more conventional components can be used for detecting, opening a route to the development of faster and more practical imaging schemes [128, 129].

6.2.2 Photon beams generation method

The most popular photon beams generation method for UP imaging uses second-order ($\chi^{(2)}$) nonlinear interactions, either spontaneous (quantum) or stimulated (classical) PDC [130]. Figure 6.2(a) shows the photon generation machinism of the PDC process, where a high-energy pump photon is converted to a pair of photon beams, which includes the two photons used for probing and detecting. Due to the energy conservation, both the UPs and detected photons (DP) have longer wavelengths than the pump photons. The benefit of this method is the high conversion efficiency and low losses of the nonlinear crystals available for such processing. An alternative photon beams generation method is using the third-order ($\chi^{(3)}$) nonlinear interaction of FWM in nonlinear waveguide platforms. Figure 6.2(b) shows the photon beam generation machinism of FWM. Two pump photons are converted to a photon-pair, which includes a red-shift UP and a blue-shift DP. The wavelength difference range of the UP and DP is only limited by the transparency window of the nonlinear waveguide.

Due to the absence of $\chi^{(2)}$ processes for the SCF platform, FWM is used to generate the photon beams for UP imaging. Although FWM relies on a higher-order nonlinear process, which is not as strong as the $\chi^{(2)}$ processes, phase matching can be achieved conveniently by engineering the waveguide dispersion, which makes it flexible to choose the operating wavelengths for photon beams generation. Moreover, the SCF waveguide systems can substantially simplify the implementation and allow for integration

with other fibre components to produce more compact all-fibre photon beam sources, which is important for the development of more robust UP imaging systems [131].

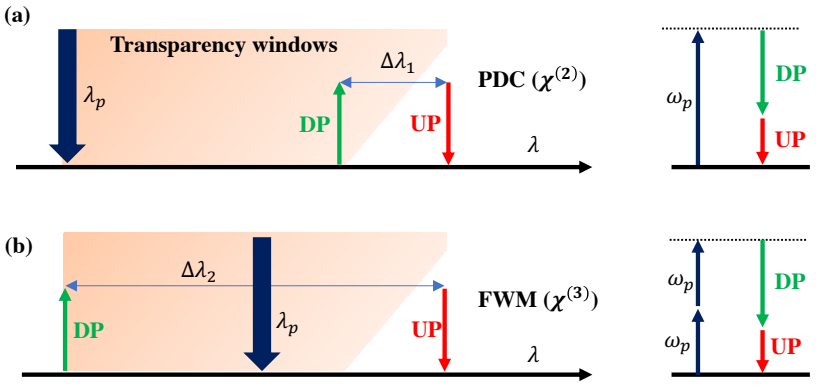

FIGURE 6.2: Operational principle and energy level diagrams of (a) $\chi^{(2)}$ and (b) $\chi^{(3)}$ processes for undetected-photon beams generation. UP: undetected photons; DP: detected photons; PDC: parametric down-conversion.

6.3 System design

6.3.1 Imaging system design

To design a suitable system for SCF-based UP imaging, two previous systems are compared, including the quantum imaging system of Lemos *et al.* [126] and the classical imaging system of Cardoso *et al.* [128]. As shown in Figure 6.3(a), the quantum imaging setup uses the spontaneous PDC in two identical $\chi^{(2)}$ nonlinear crystals of periodically poled potassium titanyl phosphate (PPKTP) to generate entangled photon beams. The benefit of this design is that the object and reference arms within the setup can have the same light path lengths to achieve high spatial entanglement for the detecting photons, and therefore generate high-quality images. Another benefit of this setup design is that the pump powers for the two crystals can be adjusted flexibly by changing the power split ratio for the pump, which can be used to balance the power of the two arms to increase the visibility of interference fringes.

Figure 6.3(b) shows the classical UP imaging system of Cardoso *et al.* [128], in which the pump and probe laser are used to produce classical beams for detection by passing through the same $\chi^{(2)}$ nonlinear crystal of barium borate (BBO) twice. The benefit of this setup is that only one nonlinear medium is needed, so that the whole system is more simple. However, due to the intrinsic difference in the light path lengths for the undetected and detected waves ($\Delta L > 0.6$ m), a long coherence length is needed for high-quality amplitude and phase images. Narrow linewidth pump and probe lasers were used in Ref. [128] for the stimulated PDC process to generate light with a long coherence length.

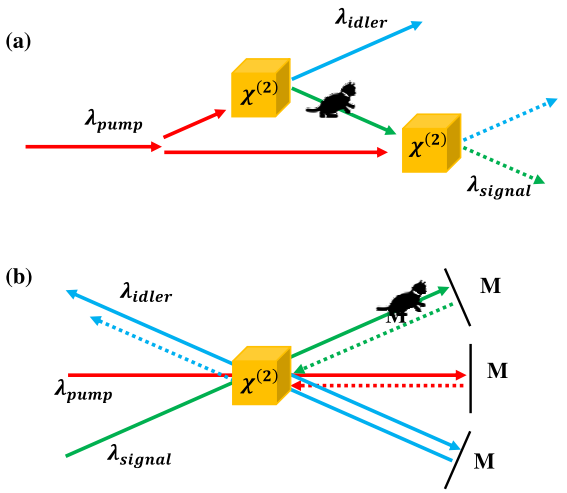

FIGURE 6.3: Schematic of UP imaging system for the (a) quantum system in Ref. [126], (b) classical system in Ref. [128].

Figure 6.4 shows the experimental setup design for SCF-based UP imaging, which combines features of the quantum setup of Lemos *et al.* [126] with the classical approach of Cardoso *et al.* [128]. Stimulated FWM in the tapered SCFs was used to generate photon beams for UP imaging. The pump and signal lasers are split equally before launching into two identical SCFs, more similar to the approach used in the quantum implementation [126], where the light paths were balanced. Moreover, unlike the complex free space setup needed for Figure 6.3, fiberised optical components can be used due to the fibre geometry of the SCFs and the ability to position the UP and DP at wavelengths where traditional couplers can be bought. The object is inserted into the probe laser of the object arm before being coupled into the path of the fibre. By assuming the object has a transmission coefficient T and introduces a phase delay of γ, the signal path for the object and reference arms in Figure 6.4 is similar to that in Figure 6.3(a), and can be expressed as [126]:

$$E_{ob} = \sqrt{T}|A_s|e^{i\gamma}, \tag{6.1}$$

$$E_{ref} = |A_s|. \tag{6.2}$$

Therefore, the amplitude and phase information of the object can be converted from the signal waves to the idlers by using the intrinsic amplitude correlation ($|A_i| \propto |A_p|^2|A_s|$) and phase correlation ($\phi_i = -\phi_s$). By combining the generated idlers from the two

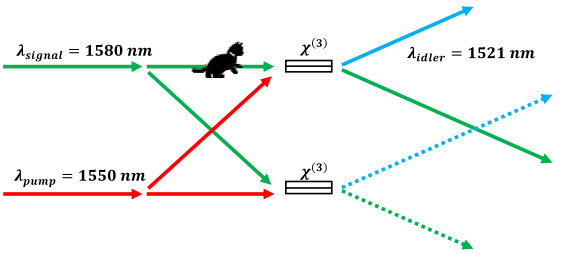

FIGURE 6.4: Schematic of FWM-based UP imaging system in SCFs.

arms, the power for detection can be expressed as [126]:

$$P = \frac{1}{2}[1 \pm T\cos\gamma]. \tag{6.3}$$

As we can see, the information of amplitude and phase are mixed in Equation (6.3). To achieve amplitude imaging specifically, the amplitude information T should be separated from the phase information γ. Therefore, a phase compensation of γ should be introduced to the reference arm to eliminate the phase item ($\cos\gamma$) in Equation (6.3), so that T can be determined by measuring the total power ($P = 1/2[1 \pm T]$). For phase imaging, the idlers are overlapped in free space to generate interference fringes, which have a visibility of T, so that the phase can be estimated by measuring the interferometric fringes, as discussed in [132].

6.3.2 Fibre design and characterisation

TABLE 6.1: Geometrical parameters and insertion losses for two tapered SCFs.

Fibre name	D_w (nm)	L_w (cm)	L_0 (cm)	Insertion loss (dB)
Fibre9	∼915	1.5	1.9	8.7
Fibre10	∼915	1.5	1.8	8.2

Due to the low optical transmission loss and high coupling efficiency of the SCFs in the telecom band, a pump source with a wavelength of 1.55 μm was selected to generate photon beams via stimulated FWM. The target core diameter of the SCFs was 915 nm, so that the ZDW is close to 1.55 μm to obtain high nonlinear *CE*s. Figure 6.5(a) shows the calculated GVD (β_2) and FOD (β_4) for the SCFs with this core diameter. Figure 6.5(b) shows the FWM efficiency as a function of signal wavelengths and fibre lengths by solving Equation (5.4) with the calculated GVD of 0.016 $\mathrm{ps^2\ m^{-1}}$ and FOD of -0.83$\times10^{-5}$ $\mathrm{ps^4\ m^{-1}}$. The strong FWM can happen with a large bandwidth from 1.4 μm to 1.8 μm. However, to ensure standard components with good performance metrics and minimal loss can be used in the UP imaging system, the signal is set at 1580 nm and the wavelength conversion bandwidth is ∼60 nm (from 1580 nm to 1521 nm). The tapered waist length of 1.5 cm was selected to obtain sufficient nonlinear conversion (∼-30 dB) without introducing too much loss. Table 6.1 summarises the parameters of the two tapered SCFs used for imaging. By using the 7.3 dB coupling loss in the telecom band, the estimated transmission loss for both fibres was around 0.8 dB $\mathrm{cm^{-1}}$. Figure 6.5(c) and Figure 6.5(d) show the FWM characterization results for these two identical tapered SCFs used for UP imaging. As the ZDW was designed to be very close to the pump wavelength, these fibres exhibit a large FWM bandwidth. The decreasing of the *CE* curves for these two fibres as the signal wavelength increases mainly caused by the wavelength dependence of the fibre coupling loss. The high *CE*s at the

signal wavelength of 1.58 μm ensured high generated beam powers for the UP imaging measurements.

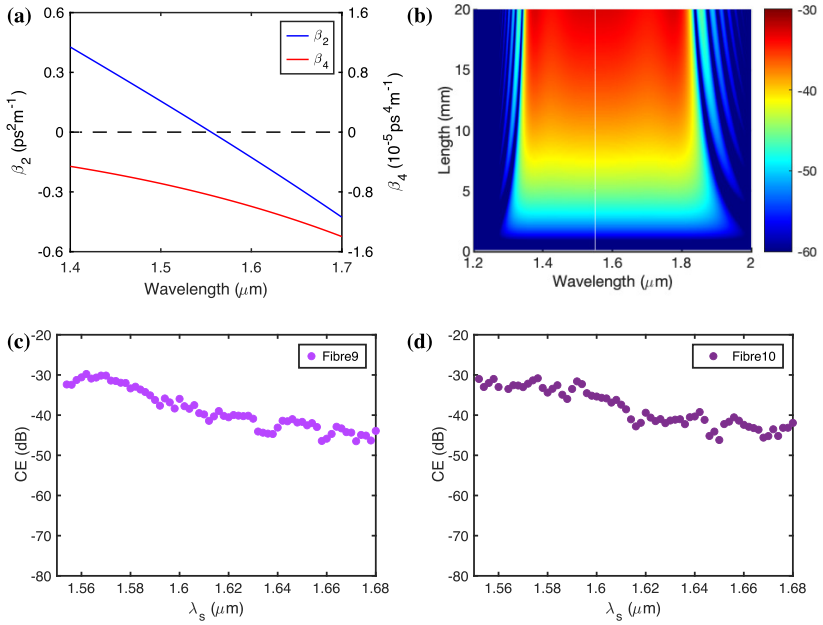

FIGURE 6.5: (a) Calculated GVD and FOD parameters and (b) simulated FWM efficiency as a function of signal wavelength and fibre length. FWM characterisation results of (c) Fibre9 and (d) Fibre10.

6.4 Imaging results

6.4.1 Amplitude imaging

Figure 6.6 shows the schematic of the amplitude imaging setup. CW sources at 1.55 μm and 1.58 μm were used as the pump and signal lasers, respectively. The coupled in pump power was fixed at 48 mW and the signal power was ~20 mW for each SCF. The nonlinear absorption processes can be ignored due to the low pump and signal power. A free-space section was included in the setup to achieve the interaction between the

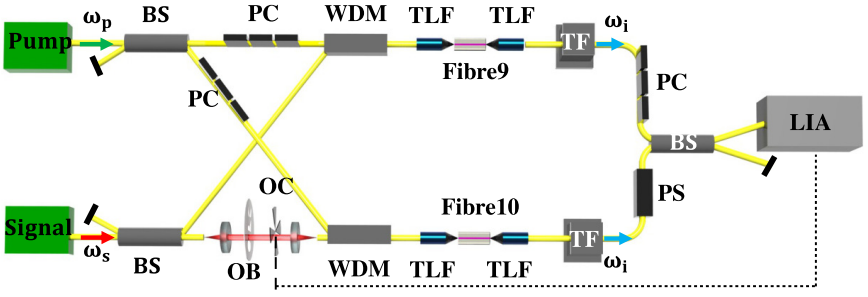

FIGURE 6.6: Experimental setup for amplitude imaging using undetected photons. OB, object; OC, optical chopper; TF, tunable filter and PS, phase shifter.

signal light and the object. The probe signal light is coupled out of and back into the fibre system using fibre collimators. The total coupling loss of this section is 1.05 dB, which introduced a small power difference between the signal and idler beams in the two arms. A two-axis stage was used to fix the object so that it could be scanned across the beam along the x and y-directions perpendicular to the propagation direction of the beams. Two PCs were used to align the relative polarisation between the pump and signal beams. Low-loss WDMs were used to combine the aligned pump and signal beams before launching into the SCFs using TLFs. To ensure the light is launched into fundamental mode of the SCFs, the outputs were coupled out using lenses and the mode profiles were checked with a camera before using the tapered lens fibres for the output side. Two filters were used to filter out the pump and signal beams from the output light. Then the two idlers were sent to the detector. A phase shifter was also placed in the object arm to compensate for the phase difference between the two arms for amplitude detection. A LIA was used and connected with a 50% duty cycle optical chopper (OC) to measure the power variation of the combined idlers precisely. To simply record the sum of the idler powers, the OC was inserted into the free-space section to modulate the DC signal for detection.

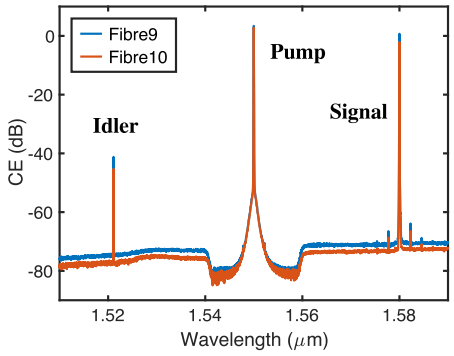

FIGURE 6.7: FWM spectra generated by the two SCFs during amplitude imaging.

Figure 6.7 shows the FWM spectra generated by two SCFs in the amplitude imaging measurement. Due to the loss difference between the two arms, the idler generated by Fibre10 was around 4.05 dB lower than that of Fibre9. The loss difference was introduced by the chopper (3 dB) and the fibre collimators (1.05 dB). The resolution of this imaging system depends on the beam profile of the signal beam (D=1.38 mm). Although the resolution is not very high due to the use of collimators, it can be optimised by replacing the collimators with a lens system, which can have a smaller focused beam size, as discussed in Chapter 2. As an example, the calculated beam size of a lens with a 5 mm focus length and input beam diameter is less than 2 μm by using Equation (2.3). With a careful redesign of the free-space section to avoid introducing setup instability, a small beam spot size is achievable in this setup to improve the resolution.

The amplitude object was fabricated using aluminum foil because the foil completely blocks the 1.58 μm signal beam ($T = 0$), whilst the lettering is fully transparent ($T = 1$).

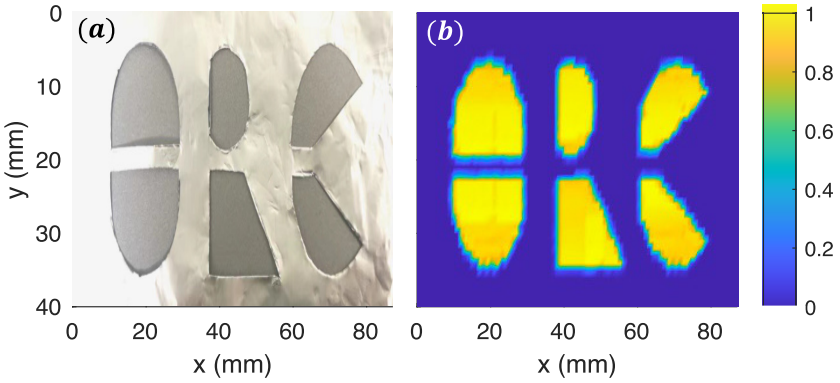

FIGURE 6.8: (a) Object with an ORC pattern for amplitude imaging. (b) Relative amplitude image obtained with a scanning step of 1 mm.

Figure 6.8(a) shows the shape of the amplitude object, where an ORC pattern was cut into the foil. A scanning step size of 1 mm was used for amplitude imaging in both the x and y directions, which is slightly smaller than the resolution of 1.4 mm. Figure 6.8(b) shows the amplitude imaging results, and the colour scale shows the normalised amplitude levels. The intensity image matches excellently with the object pattern due to the stability of this fiberized system. Moreover, the long coherence length of the idler beams also contribute to the system stability. The coherent length of FWM depends on the convolution of pump and signal bandwidth, which can be expressed as:

$$L_{coh} = c\tau_{coh} = \frac{c}{\pi\Delta\nu}, \tag{6.4}$$

where $\Delta\nu$ is the FWHM linewidth of the two idlers. By using the linewidths of the pump and signal lasers (10 kHz), the linewidth of the idlers were estimated to be ~20 kHz, so that this system exhibits a coherence length of more than 4 km. The long coherence length of the idler beams ensure the high imaging quality of this UP system.

6.4.2 Phase imaging

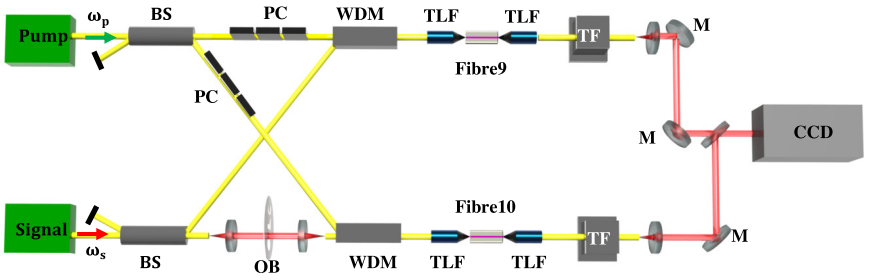

FIGURE 6.9: Experimental setup for phase imaging using undetected photons.

Figure 6.9 shows the setup used for phase imaging. The setup for idlers generation in the two SCFs is retained, but the chopper was removed and the photodetector was

replaced by a CCD camera. The two idlers are overlapped in free space to generate the interference pattern in the camera. Due to the removal of the OC, the losses for the two arms were more balanced, so that the powers of the two idler beam was more equal to generate high visibility interference fringes. As discussed by Joenathan *et al.* [132], the phase changes can be measured by the interference Moiré fringes.

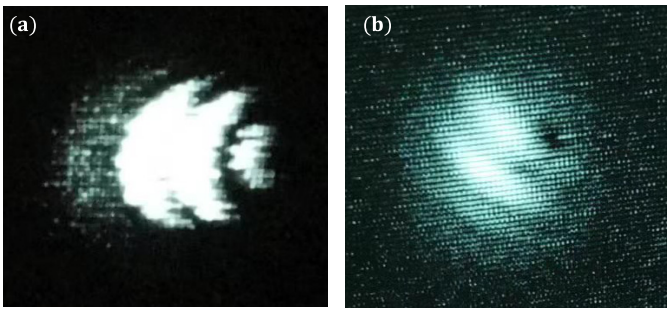

FIGURE 6.10: Interference fringes (a) without and (b) with the insertion of the pellicle film.

Figure 6.10(a) shows the interfence fringes generated by the two idlers. Although the idler beam powers of the two arms were not very high (∼10 nW), the interfence pattern was still very clear. To introduce a phase difference for the two arms, a 2 μm thick pellicle film was selected as the material for the phase object. The benefit of using this material is that it has a high transmission of 92% for the 1580 nm signal, which can ensure the signal power will not be attenuated too much, so that the generated idler in the object arm is large enough to generate high visibility interference fringes with the idler from the reference arm. Moreover, the pellicle material has a refractive index of ∼1.4, thus a phase difference of $\sim\pi$ can be introduced with the film, which ensures that the fringe variation can be clearly observed. Figure 6.10(b) shows the interference fringes by inserting the pellicle film into the object arm. Although the visibility is reduced due to the loss of the pellicle film, the fringes can be still observed due to the high transmission of the film.

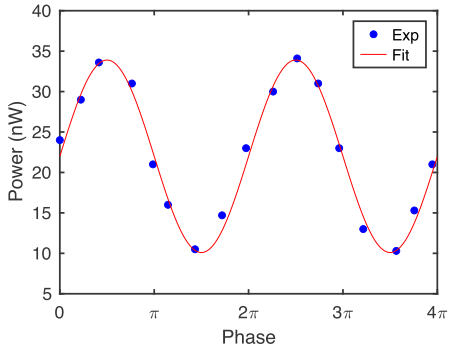

FIGURE 6.11: Phase correlation measurement for the detected idlers, including a sinusoidal fit to the experimental data.

According to the power difference between the two generated idlers, which is caused by the loss of the phase shifter (∼2 dB). The estimated fringe visibility can be calculated as:

$$v = \frac{I_{max} - I_{min}}{I_{max} + I_{min}}. \tag{6.5}$$

The estimated fringe visibility is 60%. To obtain the experimental visibility of the interfence pattern directly, a phase shifter was used to replace the free-space section to mimic a simple phase modifier. The phase of the probe signal laser could be adjusted between 0 and 4π before launching into Fibre10. Figure 6.11 shows the combined power variation for the two FWM generated idler beams. The good agreement between the experimental data and a sinusoidal fit (solid curve) provides evidence of the phase correlation between the two generated idlers, which can be calculated to 53% visibility. The low experimental visibility (53%) in Figure 6.11 is mostly caused by this power imbalance of the system, such as different insertion loss or FWM efficiency between Fiber9 and Fiber10. Although the visibility of 53% is not excellent, the visibility could be improved by adjusting the pump or signal power for each SCF with customised BS ratios.

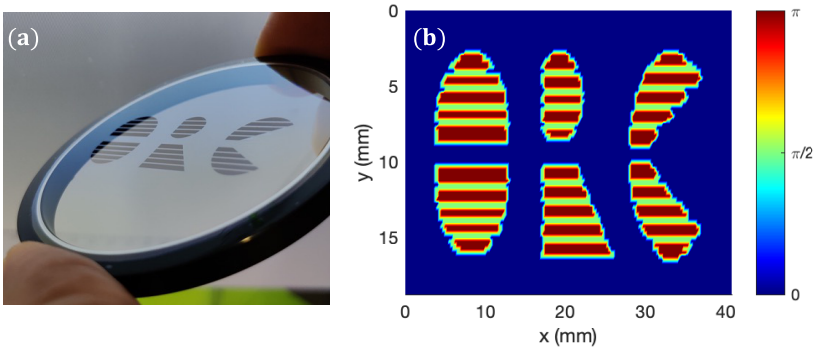

FIGURE 6.12: (a) Transparent object for phase imaging cut out from a pellicle film; (b) Relative phase image obtained with a scanning step of 1 mm.

The phase objects was fabricated by cutting the phase pattern into the film via a high-power laser cutting process to get a high-quality phase object. Figure 6.12(a) shows the laser-cut phase object, which has a clean ORC pattern. The small bridges were used to stop the film from curving after cutting out a big piece from the centre. Figure 6.12(b) shows the measured phase image, and the colour scale shows phase shift levels. The ORC pattern can be clearly observed in the phase image, and the Moiré fringes are very stable when the signal beam falls inside or outside the letters. The resolution of the phase imaging is also ∼1.4 mm, which is also limited by the beam sise of the signal to probe the object. Comparing the phase and intensity images, the slightly crisper edges of the phase image to the better quality of the phase object, which was produced via laser cutting rather than hand cutting, and to the better balance between the two idler powers due to the removal of the chopper. Moreover, unlike the earlier work of

PDC-based UP imaging, where the phase correlation relies on both the phases of the pump and the signal beams [128], the phase correlation in our system only depends on the signal seed due to the intrinsic phase locking of degenerate FWM.

It is worth noting that this is the first time a third-order ($\chi^{(3)}$) nonlinear waveguide system was used for UP imaging. Compared with previous quantum systems that used second-order ($\chi^{(2)}$) nonlinear interactions, the power for detecting is much higher ($\sim$10 nW vs 1×10^6 counts/s), allowing for traditional detectors but not single-photon detectors to be used [126]. Although classical $\chi^{(2)}$ UP imaging systems can have higher power for detection than our system, it is an all-fiberized system with improving stability and portability [128, 133].

6.5 Ultrabroad band FWM

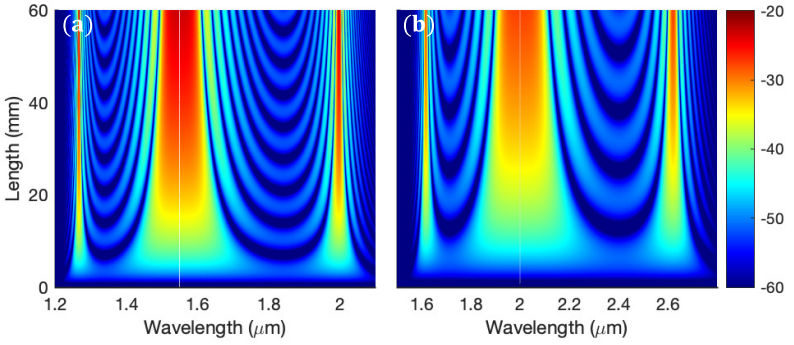

FIGURE 6.13: (a) FWM efficiency as a function of signal wavelength and fibre length (a) for SCFs with a core diameter of 0.93 μm when pumped at 1.55 μm and (b) for SCFs with a core diameter of 1.6 μm when pumped at 2 μm.

Although both good amplitude and phase imaging were demonstrated using the photon beams generated by stimulated FWM in SCFs, the wavelength conversion bandwidth was only 60 nm in the telecom band, which is far less than the transmission window of silicon material (1.1-8 μm). To investigate the possibility of ultra-broadband UP imaging based on FWM in SCF platforms, simulations are used to design SCFs with suitable fibre dispersion to achieve broadband FWM when pumping with two important wavelengths: 1.55 μm (emission window of Er^{3+}, Yb^{3+} hosted with silicate) and 2 μm (emission window of Tm^{3+}, Ho^{3+} hosted with silicate) [134]. As discussed in Chapter 5, broadband FWM is achievable when the fibre has a small positive GVD and a negative FOD at the pump wavelength, so that the perfect phase matching ($\Delta k = 0$) can be satisfied when the signal was very far away from the pump.

As examples, SCFs with core diameters of 0.93 μm and 1.6 μm are used for 1.55 μm and 2 μm pumping, respectively. Table 6.2 summarises the parameters used for the simulations. Figure 6.13(a) shows the CE as a function of signal wavelength and fibre

length when pumped at 1.55 μm. The 2 μm wavelength can be converted to ~1.2 μm with a CE of -23 dB when the fibre length is more than 2 cm. Figure 6.13(b) shows the CE colormap when pumped at 2 μm. Due to the longer pump wavelength, a 2.6 μm wavelength light can be converted to ~1.6 μm with a efficiency of -23 dB with a 2 cm fibre length. As the effective mode area at 2 μm is larger, higher input pump power (50 mW vs 20 mW) is used for the simulation.

To study the maximum wavelength conversion range of FWM in SCFs, Figure 6.14(a) and Figure 6.14(b) plot the phase matching wavelengths as a function of fibre core diameter. When pumped at 1.55 μm, SCFs with core diameter of ~0.97 μm can convert the signal wavelength from 2.5 μm to 1.2 μm. As shown in Figure 6.14(a), longer mid-infrared signal wavelength can be converted to near-infrared regime when the core diameter increases. Due to the limitation of silicon transmission window (1.1-8 μm), the longest wavelength that can be converted is ~2.6 μm when using a 1.55 μm pump source. Figure 6.14(b) shows the phase matching wavelengths when pumped at 2 μm. Due to the longer pump wavelength, the signal wavelength can be converted from 8 μm to 1.1 μm with high efficiency by using a SCF with a core diameter of 2.05 μm, covering almost the whole transmission window of silicon.

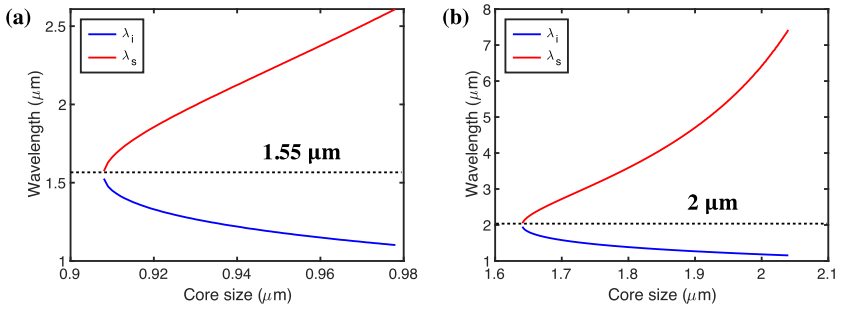

FIGURE 6.14: Maximum phase matching signal/idler wavelengths as a function of fibre core diameter when pumped at the wavelength of (a) 1.55 μm and (b) 2 μm.

6.6 Conclusion

In this chapter, UP imaging via FWM was discussed. Firstly, the concept and development of UP imaging systems were introduced, and two methods to generate photon beams for UP imaging are compared. Secondly, the UP imaging system based on the

TABLE 6.2: Fibre parameters for ultrabroad band FWM simulation.

D_w (μm)	β_2 (ps^2 m^{-1})	β_4 (10^{-5} ps^2 m^{-1})	λ_p (μm)	A_{eff} (μm^2)	P_p (mW)
0.93	0.05	-0.80	1.55	0.35	20
1.6	0.04	-0.96	2	1.13	50

SCF platform was described and the SCFs used to generate photon beams were characterized. The FWM efficiency of ∼-30 dB in a wavelength conversion bandwidth of 60 nm was achieved by using two low-loss SCFs (<0.8 dB cm^{-1}). Thirdly, high-quality phase and amplitude UP images were demonstrated with a resolution of ∼1.4 mm. The power for measurement is more than 10 nW due to the use of classical sources, which is much larger than previous quantum setups. Clear phase interference fringes were obtained with measured visibility of ∼53%. Finally, the possibility of ultrabroad band UP imaging using FWM in SCFs was discussed with simulations. The results show that efficient wavelength conversion can cover the wavelength range from 1.1 μm to 8 μm by using suitable fibre core diameters when pumped at 2 μm.

Chapter 7

Conclusions and future work

7.1 Conclusions

In summary, this thesis investigated tapered SCFs as a novel nonlinear platform for wavelength conversion and amplification in the telecom band and mid-infrared regimes.

As-drawn SCFs with a core diameter of 10 μm were successfully tapered down to a core size range of 700 nm - 3 μm with a loss of less than 1 dB cm^{-1} at both 1.55 μm and 2 μm wavelengths, with lengths yet 6.5 cm. Impressive nonlinear properties were obtained, including a TPA coefficient of $\sim$ 0.7 cm^{-1} GW and a Kerr index of $\sim$ 5×10^{-14} cm^2 GW^{-1} at 1.54 μm . The low loss and high nonlinearity of the tapered SCF, highlight the advantages of using this platform for applications in near- and mid-infrared regimes, and a range of nonlinear processes were demonstrated.

A Raman gain coefficient of 30 cm GW^{-1} at 1.55 μm and 18 cm GW^{-1} at 2 μm were measured. Thanks to the tight light confinement of the SCF platform, high intensities can be achieved, so that a modest gain (1.1 dB) was obtained with a low CW pump power of only 48 mW in the telecom band. Moreover, an excellent peak on-off gain (30.4 dB) was achieved at 2.22 μm with a picosecond pulsed laser at 2 μm, thanks to the high peak power and low nonlinear absorption. It is worth noting that this work represented the first observation of Raman gain in the SCF platform.

A FWM conversion bandwidth of more than 300 nm was achieved in the telecom band, with a maximum conversion efficiency of -30 dB. Further investigation showed that hybrid FWM with Raman scattering can produce an enhancement of more than 15 dB for the FWM conversion efficiency. These results highlight the potential of using a tapered SCF platform for highly efficient wavelength conversion in the telecom band.

SCF-based undetected-photon imaging system was demonstrated, with both high quality amplitude and phase imaging being achieved with the photon beams generated by

stimulated FWM in SCFs. The resolution was determined to be 1.4 mm, with a detection power of more than 10 nW and interference visibility of 53%. These results helped highlight the impressive robustness and stability of the SCFs as a nonlinear platform for imaging systems.

7.2 Future work

Although remarkable success has been achieved in this thesis, there are still many research opportunities for the tapered SCF platform within the nonlinear fibre optics field. For example:

1. All-fibre integrated Raman amplifier. The SCF can be integrated with SMF via low-loss nano-spike structures to make the system more robust and suitable to handle high pump powers. Moreover, due to the low loss of the tapered SCFs, a longer fibre length can be used to increase the Raman gain further. Therefore, it would be interesting to demonstrates high-quality all-fibre Raman amplifier and even lasers.

2. Mid-infrared wave generation by cascaded Raman scattering. The mid-infrared Raman experiment proved the remarkable Raman gain ($\sim$30.4 dB) at 2.22 μm with a pulsed pump laser at 2 μm. The 2.22 μm is the wavelength where TPA vanishes. Therefore, it can be the source to generate higher-order Raman scattering across the range of 2-5 μm when the Stokes power is high enough.

3. Broadband undetected-photon imaging. The conversion wavelength of FWM can be ultrabroad by redesigning the profile of the SCFs to manipulate the phase-matching condition. Converting the wavelength from the mid-infrared to telecom band for detection is very interesting for imaging and spectroscopy.

Appendix A

List of Publications

Journals

First author publications

1. **M. Huang**, S. Sun, D. Wu, H. Ren, L. Shen, T. W. Hawkins, J. Ballato, U. J. Gibson, and A. C. Peacock. Continuous-wave Raman amplification in silicon core fibers pumped in the telecom band. *APL Photonics* 6, no. 9 (2021).

2. **M. Huang**, D. Wu, H. Ren, L. Shen, T. W. Hawkins, J. Ballato, U. J. Gibson, M. Beresna, R. Slavík, J. E. Sipe, M. Liscidini, A. C. Peacock. Classical imaging with undetected photons using four-wave mixing in silicon core fibers. *Photonics Research* 11, no. 2 (2023): 137-142.

3. **M. Huang**, S. Sun, T. S. Saini, Q. Fu, L. Xu, D. Wu, H. Ren, L. Shen, T. W. Hawkins, J. Ballato, A. C. Peacock. Raman Amplification at 2.2 μm in Silicon Core Fibers with Prospects for Extended Mid-infrared Source Generation. *Light: Science & Applications* 12, no. 1 (2023): 209.

Co-author publications

1. L. Shen, H. Ren, **M. Huang**, D. Wu, and A. C. Peacock. A review of nonlinear applications in silicon optical fibers from telecom wavelengths into the mid-infrared spectral region. *Optics Communications* 463 (2020): 125437.

2. D. Wu, L. Shen, H. Ren, **M. Huang**, C. Lacava, J. Campling, S. Sun, T. W. Hawkins, U. J. Gibson, P. Petropoulos, J. Ballato, A. C. Peacock. Four-wave mixing-based wavelength conversion and parametric amplification in submicron silicon core fibers. *IEEE Journal of Selected Topics in Quantum Electronics* 27, no. 2 (2020): 1-11.

3. S. Sun, **M. Huang**, D. Wu, L. Shen, H. Ren, T. W. Hawkins, J. Ballato, U. J. Gibson, G. Z. Mashanovich, and A. C. Peacock. Raman enhanced four-wave mixing in silicon core fibers. *Optics Letters* 47, no. 7 (2022): 1626-1629.

4. L. Shen, **M. Huang**, S. Sun, D. Wu, Z. Yan, H. Ren, and A. C. Peacock. Toward in-fiber nonlinear silicon photonics. *APL Photonics* 8, no. 5 (2023).

Conferences

1. **M. Huang**, H. Ren, L. Shen, D. Wu, S. Sun, T. W. Hawkins, J. Ballato, U. J. Gibson, and A. C. Peacock. Stimulated Raman Scattering in a Tapered Submicron Silicon Core Fiber. In *CLEO: Science and Innovations*, pp. STh5A-3. Optica Publishing Group, 2021.

2. **M. Huang**, D. Wu, H. Ren, L. Shen, T. W. Hawkins, J. Ballato, U. J. Gibson, J. E. Sipe, R. Slavík, M. Liscidini and A. C. Peacock. Phase and Amplitude Imaging with Undetected Photons via Four-wave Mixing in Silicon Core Fibers. In *CLEO: Science and Innovations*, pp. SM3O-8. Optica Publishing Group, 2022.

3. **M. Huang**, S. Sun, T. S. Saini, Q. Fu, L. Xu, D. Wu, H. Ren, L. Shen, T. W. Hawkins, J. Ballato and A. C. Peacock. Mid-infrared Spontaneous and Stimulated Raman Scattering in a Silicon Core Fiber. In *2023 Conference on Lasers and Electro-Optics Europe & European Quantum Electronics Conference (CLEO/Europe-EQEC)*, pp. 1-1. IEEE, 2023.

4. S. Sun, **M. Huang**, D. Wu, L. Shen, T. W. Hawkins, J. Ballato, U. J. Gibson, G. Z. Mashanovich, and A. C. Peacock. Role of Phase-matching on Raman-enhanced FWM in Silicon Core Fibers. In *CLEO: QELS_Fundamental Science*, pp. FTh2A-7. Optica Publishing Group, 2022.

5. D. Wu, T. S. Saini, S. Sun, L. Shen, **M. Huang**, T. W. Hawkins, J. Ballato, and A. C. Peacock. Broadband MIR wavelength conversion in a tapered silicon core fiber. In *2023 Conference on Lasers and Electro-Optics Europe & European Quantum Electronics Conference (CLEO/Europe-EQEC)*, pp. 1-1. IEEE, 2023.

References

[1] R. W. Boyd, A. L. Gaeta, and E. Giese. *Nonlinear optics*. Mara Conner, 2020.

[2] G. P. Agrawal. *Nonlinear fiber optics*. Elsevier, 2013.

[3] P. D. Maker, R. W. Terhune, and C. M. Savage. Intensity-dependent changes in the refractive index of liquids. *Physical Review Letters*, 12(18):507, 1964.

[4] P. A. Franken et al. Generation of optical harmonics. *Physical Review Letters*, 7(4):118, 1961.

[5] G. Eckhardt et al. Stimulated Raman scattering from organic liquids. *Physical Review Letters*, 9(11):455, 1962.

[6] R. Y. Chiao and B. P. Stoicheff. Stimulated Brillouin scattering and coherent generation of intense hypersonic waves. *Physical Review Letters*, 12(21):592, 1964.

[7] R. L. Carman, R. Y. Chiao, and P. L. Kelley. Observation of degenerate stimulated four-photon interaction and four-wave parametric amplification. *Physical Review Letters*, 17(26):1281, 1966.

[8] J. Fournier and E. Snitzer. The nonlinear refractive index of glass. *IEEE Journal of Quantum Electronics*, 10(5):473–475, 1974.

[9] F. P. Kapron, D. B. Keck, and R. D. Maurer. Radiation losses in glass optical waveguides. *Applied Physics Letters*, 17(10):423–425, 1970.

[10] R. H. Stolen. The early years of fiber nonlinear optics. *Journal of Lightwave Technology*, 26(9):1021–1031, 2008.

[11] A. Hasegawa and F. Tappert. Transmission of stationary nonlinear optical pulses in dispersive dielectric fibers. i. anomalous dispersion. *Applied Physics Letters*, 23(3):142–144, 1973.

[12] L. F. Mollenauer, R. H. Stolen, and J. P. Gordon. Experimental observation of picosecond pulse narrowing and solitons in optical fibers. *Physical Review Letters*, 45(13):1095, 1980.

[13] L. F. Mollenauer and R. H. Stolen. The soliton laser. *Optics Letters*, 9(1):13–15, 1984.

[14] J. C. Knight et al. All-silica single-mode optical fiber with photonic crystal cladding. *Optics Letters*, 21(19):1547–1549, 1996.

[15] J. K. Ranka, R. S. Windeler, and A. J. Stentz. Visible continuum generation in air-silica microstructure optical fibers with anomalous dispersion at 800 nm. *Optics Letters*, 25(1):25–27, 2000.

[16] R. F. Cregan et al. Single-mode photonic band gap guidance of light in air. *Science*, 285(5433):1537–1539, 1999.

[17] P. J. A. Sazio et al. Microstructured optical fibers as high-pressure microfluidic reactors. *Science*, 311(5767):1583–1586, 2006.

[18] L. Shen et al. Toward in-fiber nonlinear silicon photonics. *APL Photonics*, 8(5), 2023.

[19] J. Takahashi et al. Oxidation-induced improvement in the sidewall morphology and cross-sectional profile of silicon wire waveguides. *Journal of Vacuum Science & Technology B: Microelectronics and Nanometer Structures Processing, Measurement, and Phenomena*, 22(5):2522–2525, 2004.

[20] S. Zheng et al. Silicon-based four-mode division multiplexing for chip-scale optical data transmission in the 2 μm waveband. *Photonics Research*, 7(9):1030–1035, 2019.

[21] W. Bogaerts et al. Silicon microring resonators. *Laser & Photonics Reviews*, 6(1):47–73, 2012.

[22] G. T. Reed and C. E. Jason. Silicon optical modulators. *Materials Today*, 8(1):40–50, 2005.

[23] L. Shen et al. High-performance silicon 2$\times$ 2 thermo-optic switch for the 2-μm wavelength band. *IEEE Photonics Journal*, 11(4):1–6, 2019.

[24] B. Jalali and S. Fathpour. Silicon photonics. *Journal of Lightwave Technology*, 24(12):4600–4615, 2006.

[25] X. Liu et al. Mid-infrared optical parametric amplifier using silicon nanophotonic waveguides. *Nature Photonics*, 4(8):557–560, 2010.

[26] O. Boyraz and B. Jalali. Demonstration of a silicon raman laser. *Optics Express*, 12(21):5269–5273, 2004.

[27] B. Kuyken et al. Mid-infrared to telecom-band supercontinuum generation in highly nonlinear silicon-on-insulator wire waveguides. *Optics Express*, 19(21):20172–20181, 2011.

[28] A. G. Griffith et al. Silicon-chip mid-infrared frequency comb generation. *Nature Communications*, 6(1):6299, 2015.

[29] M. Pu et al. Ultra-low-loss inverted taper coupler for silicon-on-insulator ridge waveguide. *Optics Communications*, 283(19):3678–3682, 2010.

[30] D. Vermeulen et al. High-efficiency fiber-to-chip grating couplers realized using an advanced cmos-compatible silicon-on-insulator platform. *Optics Express*, 18(17):18278–18283, 2010.

[31] B. Kuyken et al. An octave-spanning mid-infrared frequency comb generated in a silicon nanophotonic wire waveguide. *Nature Communications*, 6(1):6310, 2015.

[32] N. Singh et al. Octave-spanning coherent supercontinuum generation in silicon on insulator from 1.06 μm to beyond 2.4 μm. *Light: Science & Applications*, 7(1):17131–17131, 2018.

[33] J. S. Penadés et al. Suspended silicon waveguides for long-wave infrared wavelengths. *Optics Letters*, 43(4):795–798, 2018.

[34] F. Li et al. Low propagation loss silicon-on-sapphire waveguides for the mid-infrared. *Optics Express*, 19(16):15212–15220, 2011.

[35] M. Sinobad et al. Mid-infrared octave spanning supercontinuum generation to 8.5 μm in silicon-germanium waveguides. *Optica*, 5(4):360–366, 2018.

[36] J. Chen, Y. Sun, and L. A. Wang. Reducing splicing loss between a silicon-cored optical fiber and a silica optical fiber. *IEEE Photonics Technology Letters*, 28(16):1774–1777, 2016.

[37] H. Ren et al. Tapered silicon core fibers with nano-spikes for optical coupling via spliced silica fibers. *Optics Express*, 25(20):24157–24163, 2017.

[38] R. Sohanpal et al. All-fibre heterogeneously-integrated frequency comb generation using silicon core fibre. *Nature Communications*, 13(1):3992, 2022.

[39] H. Ren et al. Low-loss silicon core fibre platform for mid-infrared nonlinear photonics. *Light: Science & Applications*, 8(1):105, 2019.

[40] C. E. Finlayson et al. Electrical and raman characterization of silicon and germanium-filled microstructured optical fibers. *Applied Physics Letters*, 90(13), 2007.

[41] A. Rubino and E. Terzini. Amorphous silicon-based guided-wave passive and active devices for silicon integrated optoelectronics. *IEEE Journal of Selected Topics in Quantum Electronics*, 4(6):997–1002, 1998.

[42] L. Lagonigro et al. Low loss silicon fibers for photonics applications. *Applied Physics Letters*, 96(4), 2010.

[43] N. Healy et al. Polycrystalline silicon optical fibers with atomically smooth surfaces. *Optics Letters*, 36(13):2480–2482, 2011.

[44] J. Ballato et al. Silicon optical fiber. *Optics Express*, 16(23):18675–18683, 2008.

[45] T. Minami et al. In-situ observation of bubble formation at silicon melt–silica glass interface. *Journal of Crystal Growth*, 318(1):196–199, 2011.

[46] S. M. Schnurre and R. F. Schmid. Reactions at the liquid silicon/silica glass interface. *Journal of Crystal Growth*, 250(3-4):370–381, 2003.

[47] E. F. Nordstrand et al. Alkaline oxide interface modifiers for silicon fiber production. *Optical Materials Express*, 3(5):651–657, 2013.

[48] M. Kudinova et al. Two-step manufacturing of hundreds of meter-long silicon micrometer-size core optical fibers with less than 0.2 dB/cm background losses. *APL Photonics*, 6(2), 2021.

[49] B. Scott et al. Fabrication of silicon optical fiber. *Optical Engineering*, 48(10):100501–100501, 2009.

[50] C. Hou et al. Crystalline silicon core fibres from aluminium core preforms. *Nature Communications*, 6(1):6248, 2015.

[51] N. Healy et al. Tapered silicon optical fibers. *Optics Express*, 18(8):7596–7601, 2010.

[52] S. Chaudhuri et al. Crystalline silicon optical fibers with low optical loss. *ACS Photonics*, 3(3):378–384, 2016.

[53] N. Healy et al. CO_2 laser-induced directional recrystallization to produce single crystal silicon-core optical fibers with low loss. *Advanced Optical Materials*, 4(7):1004–1008, 2016.

[54] F. H. Suhailin et al. Tapered polysilicon core fibers for nonlinear photonics. *Optics Letters*, 41(7):1360–1363, 2016.

[55] Y. Franz et al. Material properties of tapered crystalline silicon core fibers. *Optical Materials Express*, 7(6):2055–2061, 2017.

[56] P. Mehta et al. Nonlinear transmission properties of hydrogenated amorphous silicon core optical fibers. *Optics Express*, 18(16):16826–16831, 2010.

[57] P. Mehta et al. Ultrafast wavelength conversion via cross-phase modulation in hydrogenated amorphous silicon optical fibers. *Optics Express*, 20(24):26110–26116, 2012.

[58] L. Shen et al. Nonlinear transmission properties of hydrogenated amorphous silicon core fibers towards the mid-infrared regime. *Optics Express*, 21(11):13075–13083, 2013.

[59] L. Shen et al. Four-wave mixing and octave-spanning supercontinuum generation in a small core hydrogenated amorphous silicon fiber pumped in the mid-infrared. *Optics Letters*, 39(19):5721–5724, 2014.

[60] M. Huang et al. Fiber integrated wavelength converter based on a silicon core fiber with a nano-spike coupler. *IEEE Photonics Technology Letters*, 31(19):1561–1564, 2019.

[61] H. Ren et al. Nonlinear optical properties of polycrystalline silicon core fibers from telecom wavelengths into the mid-infrared spectral region. *Optical Materials Express*, 9(3):1271–1279, 2019.

[62] F. A. Martinsen et al. Silicon-core glass fibres as microwire radial-junction solar cells. *Scientific Reports*, 4(1):6283, 2014.

[63] D. Homa et al. Silicon fiber with pn junction. *Applied Physics Letters*, 105(12), 2014.

[64] N. Healy et al. Extreme electronic bandgap modification in laser-crystallized silicon optical fibres. *Nature Materials*, 13(12):1122–1127, 2014.

[65] Y. P. Huang and L. A. Wang. In-line silicon schottky photodetectors on silicon cored fibers working in 1550 nm wavelength regimes. *Applied Physics Letters*, 106(19), 2015.

[66] S. Zhang et al. Temperature characteristics of silicon core optical fiber fabry–perot interferometer. *Optics Letters*, 40(7):1362–1365, 2015.

[67] F. H. Suhailin et al. Kerr nonlinear switching in a hybrid silica-silicon microspherical resonator. *Optics Express*, 23(13):17263–17268, 2015.

[68] Online website. Optical calculators for focus spot size, Date published: 2020. Available: https://wavelength-oe.com/optical-calculators/focus-spot-size/.

[69] J. Bures. *Guided optics: Optical fibers and all-fiber components*. John Wiley & Sons, 2009.

[70] A. W. Snyder and J. D. Love. *Optical waveguide theory*. Chapman and hall London, 1983.

[71] K. Han et al. Strip-slot direct mode coupler. *Optics Express*, 24(6):6532–6541, 2016.

[72] D. B. Leviton and B. J. Frey. Temperature-dependent absolute refractive index measurements of synthetic fused silica. In *Optomechanical Technologies for Astronomy*, volume 6273, pages 800–810. SPIE, 2006.

[73] Online website. Uncoated silicon window, Date published: 1999. Available: https://www.thorlabs.com/NewGroupPage9.cfm?ObjectGroup_ID=3979.

[74] Online website. Uncoated silica window, Date published: 1999. Available: https://www.thorlabs.com/newgrouppage9.cfm?objectgroup_id=3983.

[75] C. Krüger et al. Birefringence measurements on crystalline silicon. *Classical and Quantum Gravity*, 33(1):015012, 2015.

[76] B. J. Frey, D. B. Leviton, and T. J. Madison. Temperature-dependent refractive index of silicon and germanium. In *Optomechanical Technologies for Astronomy*, volume 6273, pages 790–799. SPIE, 2006.

[77] R. Kitamura, L. Pilon, and M. Jonasz. Optical constants of silica glass from extreme ultraviolet to far infrared at near room temperature. *Applied Optics*, 46(33):8118–8133, 2007.

[78] Q. Lin et al. Dispersion of silicon nonlinearities in the near infrared region. *Applied Physics Letters*, 91(2), 2007.

[79] D. K. Schroder, R. N. Thomas, and J. C. Swartz. Free carrier absorption in silicon. *IEEE Journal of Solid-state Circuits*, 13(1):180–187, 1978.

[80] Ö. Boyraz et al. All optical switching and continuum generation in silicon waveguides. *Optics Express*, 12(17):4094–4102, 2004.

[81] E. A. Kittlaus, H. Shin, and P. T. Rakich. Large brillouin amplification in silicon. *Nature Photonics*, 10(7):463–467, 2016.

[82] N. T. Otterstrom et al. A silicon brillouin laser. *Science*, 360(6393):1113–1116, 2018.

[83] H. Shin et al. Tailorable stimulated brillouin scattering in nanoscale silicon waveguides. *Nature Communications*, 4(1):1–10, 2013.

[84] D. Wu et al. Four-wave mixing-based wavelength conversion and parametric amplification in submicron silicon core fibers. *IEEE Journal of Selected Topics in Quantum Electronics*, 27(2):1–11, 2020.

[85] J. Ballato and A. C. Peacock. Perspective: Molten core optical fiber fabrication-a route to new materials and applications. *APL Photonics*, 3(12), 2018.

[86] Y. Fu et al. Efficient adiabatic silicon-on-insulator waveguide taper. *Photonics Research*, 2(3):A41–A44, 2014.

[87] A. Bera et al. Ultra-low loss waveguide platform in silicon photonics. In *Silicon Photonics XVII*, volume 12006, pages 6–11. SPIE, 2022.

[88] A. D. Bristow, N. Rotenberg, and H. M. Driel. Two-photon absorption and kerr coefficients of silicon for 850–2200nm. *Applied Physics Letters*, 90(19), 2007.

[89] H. K. Tsang and Y. Liu. Nonlinear optical properties of silicon waveguides. *Semiconductor Science and Technology*, 23(6):064007, 2008.

[90] T. Kato et al. Measurement of the nonlinear refractive index in optical fiber by the cross-phase-modulation method with depolarized pump light. *Optics Letters*, 20(9):988–990, 1995.

[91] Y. Aoki. Properties of fiber raman amplifiers and their applicability to digital optical communication systems. *Journal of Lightwave Technology*, 6(7):1225–1239, 1988.

[92] Y. Han and B. Jalali. Observation of stimulated Raman amplification in silicon waveguides. *Optics Express*, 11(15):1731–1739, 2003.

[93] H. Rong et al. An all-silicon Raman laser. *Nature*, 433(7023):292–294, 2005.

[94] Y. Takahashi et al. A micrometre-scale Raman silicon laser with a microwatt threshold. *Nature*, 498(7455):470–474, 2013.

[95] R. Claps et al. Observation of Raman emission in silicon waveguides at 1.54 μm. *Optics Express*, 10(22):1305–1313, 2002.

[96] D. R. Solli, P. Koonath, and B. Jalali. Broadband Raman amplification in silicon. *Applied Physics Letters*, 93(19), 2008.

[97] V. Raghunathan et al. Demonstration of a mid-infrared silicon Raman amplifier. *Optics Express*, 15(22):14355–14362, 2007.

[98] H. Rong et al. A cascaded silicon Raman laser. *Nature Photonics*, 2(3):170–174, 2008.

[99] H. Rong et al. A continuous-wave Raman silicon laser. *Nature*, 433(7027):725–728, 2005.

[100] H. Rong et al. Raman gain and nonlinear optical absorption measurements in a low-loss silicon waveguide. *Applied Physics Letters*, 85(12):2196–2198, 2004.

[101] Q. Xu, V. R. Almeida, and M. Lipson. Demonstration of high Raman gain in a submicrometer-size silicon-on-insulator waveguide. *Optics Letters*, 30(1):35–37, 2005.

[102] D. Wu et al. Net optical parametric gain in a submicron silicon core fiber pumped in the telecom band. *APL Photonics*, 4(8), 2019.

[103] J. I. Dadap et al. Spontaneous Raman scattering in ultrasmall silicon waveguides. *Optics Letters*, 29(23):2755–2757, 2004.

[104] J. M. Ralston and R. K. Chang. Spontaneous-Raman-scattering efficiency and stimulated scattering in silicon. *Physical Review B*, 2(6):1858, 1970.

[105] R. L. Espinola et al. Raman amplification in ultrasmall silicon-on-insulator wire waveguides. *Optics Express*, 12(16):3713–3718, 2004.

[106] U. Willer et al. Near-and mid-infrared laser monitoring of industrial processes, environment and security applications. *Optics and Lasers in Engineering*, 44(7):699–710, 2006.

[107] Z. Du et al. Mid-infrared tunable laser-based broadband fingerprint absorption spectroscopy for trace gas sensing: a review. *Applied Sciences*, 9(2):338, 2019.

[108] R. Ghorbani and F. M. Schmidt. Real-time breath gas analysis of CO and CO_2 using an EC-QCL. *Applied Physics B*, 123:1–11, 2017.

[109] T. K. Liang and H. K. Tsang. Efficient Raman amplification in silicon-on-insulator waveguides. *Applied Physics Letters*, 85(16):3343–3345, 2004.

[110] Q. Fu et al. Controllable duration and repetition-rate picosecond pulses from a high-average-power OP-GaAs OPO. *Optics Express*, 28(22):32540–32548, 2020.

[111] J. Zhou et al. Ultrafast Raman fiber laser: a review and prospect. *PhotoniX*, 3(1):1–23, 2022.

[112] Q. Lin et al. Ultrabroadband parametric generation and wavelength conversion in silicon waveguides. *Optics Express*, 14(11):4786–4799, 2006.

[113] T. Cheng et al. The second-order Raman stokes stronger than the first-order Raman stokes due to inverse Raman scattering in a single mode tellurite fiber. *IEEE Journal of Quantum Electronics*, 53(4):1–4, 2017.

[114] L. G. Holmen et al. Tunable holmium-doped fiber laser with multiwatt operation from 2025 nm to 2200 nm. *Optics Letters*, 44(17):4131–4134, 2019.

[115] S. Hollitt et al. A linearly polarised, pulsed ho-doped fiber laser. *Optics Express*, 20(15):16285–16290, 2012.

[116] F. Wang et al. Mid-infrared cascaded stimulated Raman scattering and flat supercontinuum generation in an As-S optical fiber pump at 2 μm. *Applied Optics*, 60(22):6351–6356, 2021.

[117] M. A. Foster et al. Broad-band continuous-wave parametric wavelength conversion in silicon nanowaveguides. *Optics Express*, 15(20):12949–12958, 2007.

[118] R. Claps et al. Anti-stokes raman conversion in silicon waveguides. *Optics Express*, 11(22):2862–2872, 2003.

[119] N. Vermeulen, J. E. Sipe, and H. Thienpont. Quasi-phase-matched cavity-enhanced raman converter based on a silicon nanowire ring. *IEEE Photonics Technology Letters*, 22(24):1796–1798, 2010.

[120] S. Sun et al. Raman enhanced four-wave mixing in silicon core fibers. *Optics Letters*, 47(7):1626–1629, 2022.

[121] A. Gajda et al. Highly efficient cw parametric conversion at 1550 nm in soi waveguides by reverse biased pin junction. *Optics Express*, 20(12):13100–13107, 2012.

[122] V. Boyer et al. Entangled images from four-wave mixing. *Science*, 321(5888):544–547, 2008.

[123] J. S. Dam, L. P. Tidemand, and C. Pedersen. Room-temperature mid-infrared single-photon spectral imaging. *Nature Photonics*, 6(11):788–793, 2012.

[124] D. Ding et al. Experimental up-conversion of images. *Physical Review A*, 86:033803, 2012.

[125] K. Huang et al. Wide-field mid-infrared single-photon upconversion imaging. *Nature Communications*, 13(1):1077, 2022.

[126] G. B. Lemos et al. Quantum imaging with undetected photons. *Nature*, 512(7515):409–412, 2014.

[127] J. H. Shapiro, D. Venkatraman, and F. N. C. Wong. Classical imaging with undetected photons. *Scientific Reports*, 5(1):10329, 2015.

[128] A. C. Cardoso et al. Classical imaging with undetected light. *Physical Review A*, 97(3):033827, 2018.

[129] A. Búzás et al. Biological microscopy with undetected photons. *IEEE Access*, 8:107539–107548, 2020.

[130] G. B. Lemos et al. Quantum imaging and metrology with undetected photons: tutorial. *Journal of the Optical Society of America B: Optical Physics*, 39(8):2200–2228, 2022.

[131] S. Slussarenko and G. J. Pryde. Photonic quantum information processing: a concise review. *Applied Physics Reviews*, 6(4), 2019.

[132] C. Joenathan and B. M. Khorana. Phase measurement by differentiating interferometric fringes. *Journal of Modern Optics*, 39(10):2075–2087, 1992.

[133] G. M. Basset et al. Video-rate imaging with undetected photons. *Laser & Photonics Reviews*, 15(6):2000327, 2021.

[134] S. D. Jackson. Towards high-power mid-infrared emission from a fibre laser. *Nature Photonics*, 6(7):423–431, 2012.